VAAL UNIVERSITY OF TECHNOLOGY

Inspiring thought. Shaping talent.

The Fabrication of ClNCNTs/Fe_3O_4 Nanoparticles for the Removal of Pb^{2+} Ions in Aqueous Solution

by

Morongwa Sowela Mary-Jane Sebake

Student no: 214091007

A dissertation submitted to the Faculty of Applied and Computer Sciences

Department of Biotechnology and Chemistry in fulfilment for the degree of

Master of Applied Science in Chemistry.

Supervisor: **Dr Winny K Maboya**

Co-Supervisor: **Dr Manoko S Maubane-Nkadimeng (WITS University)**

DECLARATIONS

I declare that this dissertation is my personal work under the supervision of Dr WK Maboya and the co-supervision of Dr MS Maubane-Nkadimeng. It is hereby submitted for a degree of Master of Applied Science in Chemistry to the Department of Biotechnology and Chemistry, Vaal University of Technology. It has not been submitted before for any degree or examination in any other University.

Morongwa Sowela Mary-Jane Sebake

On this 13th day of December 2021

ABSTRACT

Removal of wastewater pollutants is urgent as they are continuously defiling the limited freshwater resources, affecting the ecosystem, aquatic and terrestrial life. Carbon nanotubes-based adsorbent materials are effective for removal of wastewater pollutants owing to their large specific surface area. Surface modification of carbon nanotubes (CNTs) can mediate specific pollutant adsorption and increase CNTs colloidal stability and chemical reactivity. Heavy metal pollution of wastewater is one of the major threats, as this metals can be toxic to humans when present at certain concentrations in drinking water. This study report the synthesis of chlorine functionalized and nitrogen doped carbon nanotubes (ClNCNTs) loaded with iron oxide nanoparticles and their use as adsorbents for Pb^{2+} ions in aqueous solutions. Carbon nanomaterials that are functionalized with chlorine and doped with nitrogen were successfully synthesized. This was done through pyrolysis of a mixture of dichlorobenzene and acetonitrile (in a 1:1 volume ratio) over 10% Fe-Co/$CaCO_3$ bi-metallic catalyst via chemical vapour deposition (CVD) method. Addition of chlorine and nitrogen to the CNTs was to enable defect and disorder creation on the surface of the nanotubes which is envisaged to create nucleation sites on the their surface for better adhesion of the iron oxide nanoparticles.
Different loadings of magnetite (Fe_3O_4) nanoparticles on the surface of the ClNCNTs was achieved using a co-precipitation method. The synthesized materials were charaterized by Raman spectroscopy, Transmission electron microscopy (TEM), Powder X-ray diffraction (PXRD) spectroscopy, Thermal gravimetric analysis (TGA), Brunauer Emmett and Teller (BET) and X-ray photoelectron spectroscopy (XPS). Highly defected CNTs, some with hollow and others with bamboo-compartments due to nitrogen inclusion were obtained.

The effect of metal salt concentration in wt.% (10, 20, 30 and 53 wt.%) was investigated. The increase in wt.% loading has resulted in an increase in surface area, and a decrease in thermal stability as a result of defected Fe_3O_4/ClNCNTs. In addition, agglomeration was observed at 30 and 53 wt.% loading, due to large amount of iron present. The identity of the Fe_3O_4 nanoparticles was confirmed by PXRD and XPS with two iron peaks deconvoluted at 725.6 eV and 721 eV respectively. The percentage loading of the Fe_3O_4 nanoparticles at the surface of the ClNCNTs was affirmed by TGA analysis, where the residual mass obtained from TGA were closely related to the mass percentages added. Different nitrogen environments namely, the quatenary, pyridinic, pyrollic and nitrogen oxides were also observed, whilst chlorine could not be deconvoluted because it was present in very limited amount probably it was masked by the iron oxide nanoparticle. Thus, a 20 wt.% Fe_3O_4/ClNCNTs was chosen as an optimum, due

to uniform distribution of spherical nanopaticles observed along the radial length of ClNCNTs that had an average size of 10 ± 4.5 nm. The synthesized ClNCNTs and a nanocomposite made from a 20 wt.% Fe_3O_4/ClNCNTs were applied in the removal of Pb^{2+} ions from aqueous solution. The results obtained showed that a nanocomposite made from a 20 wt.% Fe_3O_4/ClNCNTs had a better adsorption capacity of 17.0 mg/g as compared with 14.8 mg/g for ClNCNTs.

DEDICATIONS

This work goes to the following individuals:

- My parents Mr MS Sebake and Mrs PM Sebake;
- My nieces Kamogelo and Phalafala; and nephews Tshegofatso, Sello, Kganya and Kgotso - Rakgadi loves you so much;
- My siblings Sello, Madidimalo and Ngoako;
- My sisters in love Edith and Nkutlelebohloko;
- My late special friend, sister and grandparents - Rest in Peace;
- And lastly to my salkom.

ACKNOWLEDGEMENTS

I would like to thank God almighty for giving me the life and strength to preserve when things were difficult. The journey was not easy, but it was worth it, as I can see the results.

Gratitude to my supervisor Dr WK Maboya, for taking a chance with a "working" student; not forgetting my co-supervisor Dr MS Maubane-Nkadimeng, for their guidance, motivation, and patient in taking this journey with me. The work was also done in collaboration with Prof NJ Coville. They have provided the necessary resources needed to execute the research.

A special thanks to my fellow researchers who always went an extra mile, namely Lebogang Mosiane, Kamogelo Modisane, Alice Magubane, Thuli Buthelezi, Boitumelo Thlaole, Bonnie Mtolo, Bokome Shaku, Themba Ntuli and the rest of the CATMAT group. Mr HK Mmako and the nanotechnology group. Appreciating the assistance from Prof. N Moloto and Zakhele Ndala with Raman analysis.

Also grateful to Dr Farai Dzike, Dr Thomas Mongwe, Dr Thapelo Mofokeng, Dr Pumza Mente "teacher Pumza" and Mohlala "sisters" namely Keorapetse and Dr Lesego for the insight knowledge they imparted regarding research and for keeping me motivated in difficult times.

I am thankful to the microscopy and microanalysis unit (MMU) headed by Prof. Alexander Ziegler and the staff, i.e., Dr MS Maubane-Nkadimeng, Dr E Linganiso, Dr Z Tetana and Jacques for the training of instruments such as XRD, TEM and SEM.

My gratitude goes to my work supervisor Mrs ML Mathebula and friend Ndivhuwo Phadziri for supporting me through the period of my studies.

Lastly to my family especially mom and dad for their support and motivation, for always preaching the word of God.

PRESENTATIONS

(i) **MSM Sebake**, MS Maubane-Nkadimeng and WK Maboya, "*Synthesis of heteroatoms (chlorine and nitrogen) containing carbon nanotubes loaded with iron oxide nanoparticles and their use as adsorbents for* Pb^{2+} *ions* **(Poster Presentation)**", Nanotechnology Young Researchers Symposium (NYRS) Virtual – University of the Witwatersrand, October 2021.

Table of Contents

DECLARATIONS i

ABSTRACT ii

DEDICATIONS iv

ACKNOWLEDGEMENTS v

PRESENTATIONS vi

LIST OF TABLES xiii

ABBREVIATIONS AND ACRONYMS xiv

CHAPTER 1 1

Synopsis 1

1. Introduction 1

1.1. Background 1

1.2. Purpose of the Study 3

1.2.1. Aim of the study 3

1.2.2. Objectives of the study 3

1.3. Justification 4

Chapter 2 8

Literature review 8

2. Brief introduction 8

2.1. Water scarcity and pollution 8

2.2. Heavy Metals 10

2.2.1. General overview of Lead (Pb) 11

2.2.1.1. Sources and uses of lead 11

2.3. Brief discussion on carbon and metal oxide nanomaterials 13

2.4. CNTs as adsorbents 14

2.5. Iron oxide nanoparticles 22

2.6. Application of nanomaterials in wastewater treatment 25

2.7. Water Treatment 27

2.7.1. Adsorption 27

2.8. Modelling of adsorption data 31

2.8.1. Kinetics studies 31

2.8.2. Adsorption isotherms 32

References 34

CHAPTER 3 43

Technical instruments used to characterize nanomaterials 43

3. Brief introduction 43

3.1. Powder X-ray diffraction spectroscopy 43

3.2. Electron microscopy 45

3.2.1. Scanning electron microscopy 45

3.2.2. Transmission electron microscopy 46

3.3. Thermal gravimetric analysis 48

3.4. X-ray photoelectron spectroscopy 50

3.5. Raman spectroscopy 51

3.6. Brunauer-Emmett-Teller 53

3.7. Atomic Absorption Spectroscopy 54

CHAPTER 4 58

4. Introduction 58

4.1. Study background 58

4.2. Experimental Procedures 60

4.2.1. Materials 60

4.2.2. Preparation of the bi-metallic catalyst 60

4.2.3. Synthesis and purification of ClNCNTs 61

4.2.4. Synthesis of ClNCNTs/Fe_3O_4 nanoparticles 62

4.2.5. Characterization techniques and data analysis 63

4.3. Results and discussions 64

4.3.1. Structural Analysis 64

4.3.2. Elemental and crystallographic analysis 66

4.3.3. Raman spectroscopy analysis 69

4.3.4. XPS analysis of ClNCNTs and 20 wt.% Fe_3O_4/ClNCNTs 72

4.4.4. Surface area and porosity analysis 75

4.4.5. Thermal gravimetric analysis 77

4.5. Conclusion 77

CHAPTER 5 83

Use of ClNCNTs and 20 wt.% Fe_3O_4/ClNCNTs-Based Nanocomposites as Nano-Adsorbents for Pb^{2+} Ions in Aqueous Solutions. 83

5. Introduction 83

5.1. Background 83

5.2. Experimental Procedures 84

5.2.2.2.1 Adsorption kinetics 86

5.2.2.2.1.1 Pseudo-first order model 86

5.2.2.2.1.2 Pseudo-second order model 87

5.2.2.2.1.3 Intraparticle diffusion 87

5.2.2.2.2 Adsorption isotherms 87

5.2.2.2.2.1. Langmuir isotherm model 88

5.2.2.2.2.2. Freundlich isotherm model 88

5.3. Results and Discussions 89

5.3.1. Adsorption studies 89

5.3.2. Kinetic studies 94

5.3.3. Isotherm studies 95

5.4. Conclusions 96

CHAPTER 6 101

6.1. Conclusions 101

6.2. Recommendations and future work 102

LIST OF FIGURES

Chapter 2

Figure 2.1: Future Projection Water Scarcity, adapted without modification from (Lingamdinne *et al.,* 2019). 9
Figure 2.2: Sources of water pollution. 10
Figure 2.3: Example of Pb; (a) chemical information and (b) sample. 11
Figure 2.4: Sources and uses of Pb, adapted without modification from (ILA, 2012). 12
Figure 2.5: Health implications of Pb, adapted without modification from (Panchangam, 2015). 13
Figure 2.6: Different types of nanomaterials used in water treatment, adapted with modification from (Cerro-Lopez and Méndez-Rojas, 2019). 14
Figure 2.7: Different model structure of SWCNTs. 15
Figure 2.8: Different types of CNTs: (a) SWCNTs and (b) MWCNTs, adapted without modification from (Santhosh *et al*., 2016). 15
Figure 2.9: Structural model of MWCNTs (a) Russian doll and (b) Parchment. 16
Figure 2.10: Set up of the CVD reactor. 16
Figure 2.11: Set up of arc discharge, adapted without modification from (Mehra and Jain, 2014). 17
Figure 2.12: Set up of laser ablation method, adapted without modification from (Lu *et al*., 2019). 18
Figure 2.13: Structure of Fe_3O_4 unit cell, adapted without modification from (Blaney, 2007). 23
Figure 2.14: Characteristics of physical adsorption process. 29
Figure 2.15: Characteristics of chemical adsorption process. 30

Chapter 3

Figure 3.1: Bruker D2 Phaser PXRD. 44
Figure 3.2: FEI Nova Nanolab 600 SEM. 46
Figure 3.3: A FEI Tecnai T12 TEM. 47
Figure 3.4: Perkin Elmer TGA STA 4000 series. 49
Figure 3.5: A PHI 5000 Versaprobe XPS. 51

Figure 3.6: Bruker Senterra Raman Spectroscopy. 52
Figure 3.7: A Micromeritics RS232 Brunnauer -Emmett-Teller (BET) surface area and porosity analyser. 54
Figure 3.8: An Agilent Technologies 200 series AAS. 55

Chapter 4

Figure 4.1: The schematic presentation of a CVD used to synthesize ClNCNTs. 61
Figure 4.2: The schematic presentation of a reflux system used to synthesize Fe_3O_4/ClNCNTs via a co-precipitation method. 62
Figure 4.3: TEM images of ClNCNTs un-loaded (a) and loaded with Fe_3O_4 using metal salts of different weight percentages (b)10 wt.%, (c) 20 wt.%, (d) 30 wt.%, and (e) 53 wt.% . 65
Figure 4.4: Histogram representing the average particles diameter of Fe_3O_4 nanoparticles loaded on ClNCNTs produced using a 20 wt.% metal loading. 66
Figure 4.5: EDX of ClNCNTs loaded with Fe_3O_4 generated from a 20 wt.% metal salt solution. 67
Figure 4.6: PXRD patterns of ClNCNTs un-loaded and loaded with with different metal salt loading of 10, 20, 30 and 53 wt.%. 68
Figure 4.7: Raman spectra of ClNCNTs un-loaded and loaded with different metal salt loading of 10, 20, 30, and 53 wt.% respetively. 70
Figure 4.8: XPS survey scan of (a) ClNCNTs un-loaded and (b) loaded with 20 wt.% Fe_3O_4. 72
Figure 4.9: XPS survey scan of the deconvoluted spectra of ClNCNTs; (a) C1s, (b) O1s, (c) N1s, and (d) Cl2p. 74
Figure 4.10:XPS survey scan of the deconvoluted spectra of Fe_3O_4/ClNCNTs; (a) C1s, (b) O1s, (c) N1s, and (d) Fe 2p. 74
Figure 4.11: Plots of adsorption and desorption nitrogen isortherms for ClNCNTs and Fe_3O_4/ClNCNTs. 76
Figure 4.12:(a) TGA and (b) the corresponding derivative (DTGA) curves of the un-loaded and loaded ClNCNTs. 77

Chapter 5

Figure 5.1: Schematic representation of adsorption batch studies. 86

Figure 5.2: Effect of initial pH on Pb^{2+} ions removal using ClNCNTs and 20 wt.% Fe_3O_4/CINCNTs (initial concentration: 100 mg/L, adsorbent mass: 0.05g, contact time = 16 h, shaking speed: 200 rpm and temperature: 298 K). 90

Figure 5.3: Effect of dosage mass of un-loaded ClNCNTs and 20 wt.% Fe_3O_4/CINCNTs loaded ClNCNTs (0.01 to 0.05 g) on Pb^{2+} ions removal (initial concentration: 100 mg/L, contact time = 16 h, shaking speed: 200 rpm, pH: 5, and temperature: 298 K). 91

Figure 5.4: Effect of initial Pb^{2+} ions concentration on the adsorption capacity over ClNCNTs and 20 wt.% Fe_3O_4/CINCNTs (adsorbent mass: 0.05 g, time: 16 h, shaking speed: 200 rpm, pH: 5 and temperature: 298 K). 92

Figure 5.5: Effect of contact time on Pb^{2+} ions uptake onto ClNCNTs and 20 wt.% Fe_3O_4/ClNCNTs, respectively with different solution concentrations of 5 to 100 mg/L (pH: 5, adsorbent mass: 0.05 g, shaking speed: 200 rpm and temperature: 298 K 93

LIST OF TABLES

Chapter 2

Table 2.1: South African Water Quality Guidelines Pb. 11

Table 2. 2: Summary of the adsorption studies of lead using nanomaterials as adsorbents. 26

Table 2.3: The conventional water treatment technologies, adapted without modification from Volesky, (2001). 27

Chapter 4

Table 4.1: Reaction parameters of the loading of Fe_3O_4 onto ClNCNTs. 63

Table 4.2: EDX analysis of ClNCNTs un-loaded and loaded with Fe_3O_4 nanoparticles with different amounts of metal salt solution. 67

Table 4.3: Full width at maximum data from PXRD diffraction patterns of Fe_3O_4/ClNCNTs produced with different metal loading of Fe_3O_4: 10, 20, 30 and 53 wt.% metal solution loadings. 68

Table 4.4: Raman main vibrational modes of ClNCNTs unloaded and loaded with different metal salt loading of 10, 20, 30 and 53 wt.%. 71

Table 4.5: Summary of Raman data of the ClNCNTs un-loaded and loaded with Fe_3O_4 nanoparticles. 72

Table 4.6: Summary of BET data of the ClNCNTs un-loaded and loaded with Fe_3O_4 nanoparticles. 76

Chapter 5

Table 5.1: The experimental data of kinetics adsorption model of ClNCNTs. 94

Table 5.2: The experimental data of kinetics adsorption model of 20 wt.% Fe_3O_4/CINCNTs. 95

Table 5.3: The experimental data of Langmuir isotherms adsorption model of ClNCNTs and 20 wt.% Fe_3O_4/CINCNTs. 96

Table 5.4: Langmuir equilibrium parameter or separation factor values of ClNCNTs and 20 wt.% Fe_3O_4/CINCNTs attained for different initial concentrations. 96

ABBREVIATIONS AND ACRONYMS

a.u.	Arbitrary units
BET	Brunnauer-Emmet-Teller
B	Boron
C	Carbon
C	Constant (BET) constant adjusted parameter
CCD	Charged-couples device
C_e	Concentration of metal ion at equilibrium
C_i	Initial Concentration of metal ion
CNM(s)	Carbon nanomaterial(s)
ClNCNT(s)	Chlorinated nitrogen-doped carbon nanotube(s)
CCl_4	Carbon tetrachloride
Cl	Chlorine
CNT(s)	Carbon nanotube(s)
Co	Cobalt
$CoFe_2O_4$	Cobalt ferrite
Cr	Chromium
Cu	Copper
CVD	Chemical vapour deposition
C_2H_2	Acetylene
D	Disorder-induced band
dc	Crystalline Size
DCB	Dichlorobenzene
DEA	Department of Environmental Affairs

DEF	Department of Environmental and Forestry
DEFF	Department of Environment, Forestry and Fisheries
DWF	Department of Water Affairs
DWS	Department of Water and Sanitation
EDX	Energy dispersive X-ray
EM	Electron Microscopy
ERWAT	Ekurhuleni Water Care Company
eV	Electron volts
FWHM	Full width half maximum
FTIR	Fourier transform infrared
Fe	Iron
Fe_3O_4	Magnetite
γ-Fe_2O_3	Maghemite
Fe_3O_4	Iron Oxide
α-Fe_2O_3	Hematite
g	gram
G	Graphitic band
GBD	Global burden of disease
g/cm^3	gram per cubic metre
h	hour
HCl	Hydrochloric acid
Hg	Mercury

HNO_3	Nitric acid
H_2SO_4	Sulphuric acid
I_D/I_G	Intensity ratio of D to G bands
IHME	Institute for Health Metrics and Evaluation
ILA	International Lead Association
IPD	Intraparticle diffusion
IWMM	International Water Management Institute
k_1	Pseudo-first-order constant
k_2	Pseudo-second-order constant
k_f	Freundlich isotherm constant
kJ/mol	Kilo joules per moles
m	mass of adsorbent
M	Molar
mg/g	milligram per gram
mg $L^{-1.}$	milligram per litre
Min	minutes
mL	Millilitre
mL/min	Millilitre per minutes
MWCNTs	Multi-walled carbon nanotubes
n	Freundlich exponent
NaOH	Sodium hydroxide

N-CNTs	Nitrogen doped carbon nanotubes
N-CNT: Cl	Nitrogen doped carbon nanotubes chlorine
N-CNT: O	Nitrogen doped carbon nanotubes oxygen
NEMA	National Environmental Management Act
NEMWA	National Environmental Management Waste Act
Ni	Nickel
NiO	Nickel oxide
nm	Nanometres
NPs	Nanoparticles
N_2	Nitrogen
P	Pressure (equilibrium)
Pb	Lead
PFO	Pseudo-first-order constant
PSO	Pseudo-second-order constant
P_o	Permeation pressure
PXRD	Powdered X-ray diffraction
pH_{PZC}	Point zero charge
q_e	quantity of metal ion adsorbed
q_m	quantity of the maximum metal ion uptake
q_t	quantity of metal ion uptake at time
RSA	Republic of South Africas

s	seconds
SANDF	South African National Defence Force
SEM	Scanning electron microscopy
SWCNTs	Single-walled carbon nanotubes
TCE	Trichloroethylene
TEM	Transmission electron microscopy
TGA	Thermogravimetric analysis
TTCE	Tetrachloroethane
V	Volume of solution
V_m	Volume of the monolayer absorbed
XPS	X-ray photoelectron spectroscopy
UN	United Nations
USA	United States of America
WHO	World Health Organization
wt.%	weight percentage
Zn	Zinc
As	Arsenic
°C	degrees celsius
%	Percentage
θ	Theta
$W.m^{-1}.K^{-1}$	Watts per meter per kelvin
Ω^{-1} cm^{-1}	per ohms per centimiter
Ω^{-1}	per ohms

DISSERTATION OUTLINE

The report is divided into six chapters.

Chapter 1: Synopsis

It presents the introduction, motivation, justification and the aims and objectives of the study.

Chapter 2: Literature Review

It presents a literature review of nanomaterials (i.e., carbon nanotubes (CNTs)) and iron oxide nanoparticles. The synthesis methods, structural architecture, modifications, and applications of these nanomaterials are discussed. A brief review of application of CNTs, metal oxides and CNTs/metal oxides composites as adsorbents in water treatment is herein presented. Moreover, a discussion on adsorption technique as a wastewater treatment method is also presented.

Chapter 3: Characterization techniques

It presents the discussion of different analytical techniques that were utilised in the characterization of the nanomaterials.

Chapter 4: Synthesis of nanomaterials

It presents the experimental details (i.e., chemical vapour deposition (CVD) method) and data analysis of the characterized chlorine functionalised, and nitrogen doped CNTs (ClNCNTs). A description of the weight percentage loading of magnetite nanoparticles (Fe_3O_4) onto the ClNCNTs is also discussed in detail.

Chapter 5: Application of nanomaterials

The chapter focuses on the experimental details and data analysis of ClNCNTs and Fe_3O_4/ClNCNTs used as nano-adsorbents in the removal of lead (i.e., Pb^{2+} ions) from aqueous solution. It includes the adsorption batch studies, kinetics and isotherms models.

Chapter 6: Conclusions and recommendations

It presents general conclusions based on the work done, which is the overall results of the study and the recommendations for future works and followed by references.

CHAPTER 1

Synopsis

1. Introduction

This chapter presents the background, the aim and objectives together with the justification of the study.

1.1. Background

Water is an essential part of human life and other living organisms is water. Water scarcity is becoming a huge problem all over the world due to contamination, rapid growth of population, lack of rain and increased industrialization (Singh and Song, 2001; Yang *et al*., 2019). Water quality is deteriorating due to presence of common pollutants from chemical industries. Pollutants in water include heavy metals such as arsenic (As), cadmium (Cd), chromium (Cr), copper (Cu), lead (Pb), mercury (Hg), nickel (Ni), and zinc (Zn) (Akpor and Muchie, 2010). Water pollution is a universal problem, which threatens the lives of all the living species, the biodiversity. The accepted levels of heavy metals in wastewater is set by the regulators such as the World Health Organization (WHO) (WHO, 2014), and in South Africa by the Department of Water and Forestry (DWF) (DWF, 1996), now known as the Department of Water and Sanitation (DWS) (National departments_South African Government-name change of departments, 2019). The disposal is regulated by the Department of Environmental Affairs (DEA, 2015 and 2019); (Department of Environmental Affairs 1998); (RSA Government, 1998), now known as Department of Environment, Forestry and Fisheries (DEFF) (National departments South African Government-name change of departments, 2019) in the country. As a result of its toxic effect on living organisms, heavy metals such as lead must be eliminated from wastewater.

Various technologies such as reverse osmosis, precipitation, ion exchange and filtration have been utilized in the treatment of wastewater for the removal of heavy metals. However, some of the technologies are effective even though there are some drawbacks in using these methods. The drawbacks includes cost, utilization of high energy and their result in the formation of secondary pollutants, whilst others are ineffective in the removal of inorganic materials (Das *et al*., 2014). An adsorption method is widely used for removal of lead because it is; (i) highly

economical, (ii) selective towards metals, (iii) regenerative, (iv) does not generate toxic sludge, (v) metals can be easily recovered, and (vi) it is effective (Tripathi and Rawat Ranjan, 2015).

Various nanoadsorbents such as nanomaterials have been used as adsorbents for a variety of contaminants in wastewater. The carbon-based nanomaterials such as carbon nanotubes (CNTs) and graphene have generated great interest in the wastewater treatment as sorbent materials for heavy metals due to their stability, limited reactivity, large surface area and are strong antioxidants (Chawla *et al*., 2015). Due to their exceptional physical, mechanical and chemical properties, CNTs have been studied intensively since their discovery. The electronic properties of CNTs were first reported in 1991 (Iijima, 1991). CNTs can be classified as single-walled carbon nanotubes (SWCNTs) and multi-walled carbon nanotubes (MWCNTs). SWCNTs have a diameter of about 1 nm and are made up of a single rolled graphene tube while MWCNTs are made up of a graphene sheet rolled into concentric tubes. Moreover, both types of CNTs differ in length as well as diameters. CNTs are materials that possess interesting adsorption behaviour pertaining to several noxious pollutants in aqueous solutions. Sadegh *et al*., (2016) indicated that CNTs as adsorbents are valuable materials to be used for the removal of pollutants, resulting from their special individual characteristics and structure, high surface area, mechanical and thermal stability.

The properties of CNTs can be improved by modifying them either through doping and/or funtionalization with various heteroatoms (e.g. nitrogen). This type of modification enhances their electronic and physical properties. The first report on the doping effect was reported in 1994 (Ayala *et al*., 2010). In this research, doping involved replacement of the carbon atom on the CNT wall with nitrogen. When MWCNTs are doped with nitrogen, their crystallinity, electrical properties, and reactivity are enhanced allowing them be used in a variety of applications (Tripathi and Rawat Ranjan, 2015). In addition, it was reported that substitution and surface functionalization had an influence on the carbon lattice. This effect may result in the increase of the reactivity sites on the curvature and breaks in the carbon lattice due to the adatom such as nitrogen (Kuzmany *et al*., 2004). Previous reports revealed that the inclusion of chlorine had the following effects, (i) it enhanced the growth of CNTs without damaging their crystalline structure (Ghemes *et al*., 2013; Nieto-Márquez *et al*., 2007), (ii) it resulted in surface restructuring (Nieto-Márquez *et al*., 2007), and (iii) it acted as a purification agent (Yuan *et al*., 2008). Furthermore, CNTs can also be functionalized by acid oxidation, which enhances their solubility, chemical reactivity and other physiochemical properties (Gupta *et*

al., 2019). This also allows for easier attachment of metal oxides such as nanoparticles (NPs) to their outerwalls.

The loading of metal oxide nanoparticles onto CNTs were firstly reported by Planeix in 1994 (Planeix *et al*., 1994). However, Fe_3O_4 nanoparticles tend to agglomerate due to Van der Waal forces. Thus, modification of the method will be beneficial for loading Fe_3O_4 onto CNTs. Moreover, Fe_3O_4 possess properties such as having high surface area and being paramagnetic which can provide more adsorption sites resulting in higher adsorption capacity of CNTs when loaded with this metal oxide nanoparticles.

Furthermore, the aforementioned properties of Fe_3O_4 will also render the Fe_3O_4/CNTs adsorbent magnetic, such that it can be easily removed after adsorption using a magnet which will allow for its re-use. In addition, the loading of Fe_3O_4 onto CNTs can result in enhancement of their electrical, mechanical and optical properties (Mallakpour and Khadem, 2016). It also amplifies the chemical adsorption abilities, while their recyclability, selectivity, and stability becomes higher (Sharma *et al*., 2017). These properties are beneficial for various applications such as in absorption, lithium ion batteries, photodetectors, sensors, and supercapacitors (Mallakpour and Khadem, 2016). The loading of Fe_3O_4 nanoparticles onto CNTs can be achieved via methods such as sol-gel, hydrothemal and co-precipitaion. Among this methods, co-precipitation is preferred because it is economical, simple and fast. Therefore, it is anticipated that the combination of adsorption properties of ClNCNTs and Fe_3O_4 might result in an effective nanoadsorbent that is recoverable and reusable. This nanoadsorbent could be used in the removal of pollutant Pb in water, due to it being toxic and detrimental to human beings.

1.2. Purpose of the Study

1.2.1. Aim of the study

The aim of the study was to modify the surface of chlorinated nitrogen-doped carbon nanotubes with Fe_3O_4 nanoparticles and use them as adsorbents for Pb^{2+} ions in aqueous solutions.

1.2.2. Objectives of the study

1. To synthesise ClNCNTs using a catalytic vapour deposition (CVD) method, by pyrolysis of a mixture of acetonitrile and dichlorobenzene over a Fe-Co/$CaCO_3$ catalyst.

2. To modify the surface of ClNCNTs with Fe_3O_4 nanoparticles by varying the nanoparticle percentage loading.
3. To determine the adsorption capacity of Pb^{2+} ions over Fe_3O_4 loaded and un-loaded ClNCNTs as adsorbents by optimizing the following parameters i.e., effect of adsorption time, adsorbent mass, pH and analyte concentration.
4. To investigate the kinetics of the adsorption process using the pseudo-first and pseudo-second order models, and the intraparticle diffusion model.
5. To investigate the mechanism of the adsorption process using the Langmuir and Freundlich adsorption models.

1.3. Justification

Shortage of water is a challenge faced globally. This phenomena has severe consequences in developing countries such as South Africa and other african countries. In South Africa, it is reported that about 5.7 million of the human population have a deprivation of basic water services ('Nanotechnology and water'). This problem is prone to escalate, due to drought caused by climate change, natality rate, urbanization and inadequate wastewater treatment from industries. For an example, lead (Pb) is a toxic heavy metal that is regarded as one of the water pollutants and has severe health implications. Hence, there is a need to remove it from wastewater for better water quality. Moreover, it was reported globally that a mortality rate of 1.1 million was due to lead exposure, while in South Africa about 2.0 % is attributed to unsafe water resources (Institute for Health Metrics and Evaluation (IHME). GBD (Global Burden of Disease) Compare, 2017). Hence, there is an acute need to improve the quality of drinking water. Clean water is a human basic right, as stipulated in the country's constitution (Constitution of the Republic of South Africa Act 108 of 1996, 1996); this can be achieved by employing the nanotechnology application.

Conventional techniques such as reverse osmosis, electrodialysis, and ion exchange are neither effective nor economical which make them require high energy input (Tripathi and Rawat Ranjan, 2015). Therefore, it is postulated that use of nanosized materials as adsorbents can aid in elimination of some of the challanges experienced with conventional methods. Hence, the attachment of Fe_3O_4 nanoparticles onto ClNCNTs is aimed to render them magnetic, which will make them easily recoverable after use. Attachment of chlorine and doping of the CNTs with nitrogen is aimed at creating defects on the surface of the CNTs thus increasing their

adsorption capabilities and attachment sites for Fe_3O_4 nanoparticles. This will allow for their use as an effective and efficient adsorbent, as it will possibly offer an opportunity to heighten the water purification industries. To our knowledge, the use of ClNCNTs loaded and un-loaded with Fe_3O_4 as adsorbents for Pb^{2+} ions in aqueous solutions is not documented.

References

Akpor, O.B. and Muchie, M., 2010. Remediation of heavy metals in drinking water and wastewater treatment systems: Processes and applications. *International Journal of the Physical Sciences*, 5 (12), 1807–1817.

Ayala, P., Arenal, R., Rümmeli, M., Rubio, A., and Pichler, T., 2010. The doping of carbon nanotubes with nitrogen and their potential applications. *Carbon*, 48 (3), 575–586.

Chawla, J., Kumar, R., and Kaur, I., 2015. Carbon nanotubes and graphenes as adsorbents for adsorption of lead ions from water: A review. *Journal of Water Supply: Research and Technology - AQUA*, 64 (6), 641–659.

Constitution of the Republic of South Africa Act 108 of 1996, 1996.

Das, R., Ali, M.E., Hamid, S.B.A., Ramakrishna, S., and Chowdhury, Z.Z., 2014. Carbon nanotube membranes for water purification: A bright future in water desalination. *Desalination*, 336 (1), 97–109.

DEA, 2015. Welcome desktop study on lead and cadmium in south africa venue : CSIR. Pretoria.

DEA, 2019. Overview of the department _ Department of Environmental Affairs [online]. Available from: http://www.environment.gov.za/aboutus/department [Accessed 27 May 2019].

https://www.defenceweb.co.za/featured/ekurhuleni-water-care-company-helping-sandf-fix-vaal-water-crisis/ [Accessed 22 Oct 2019].

Department of Environmental Affairs, 1998. *National Environmental Management Act 107 of 1998. Environmental Management.*

DWF, 1996. *South African Water Quality Guidelines Volume 1 Domestic Use Department of Water Affairs and Forestry Second edition*.

Ghemes, C., Ghemes, A., Okada, M., Mimura, H., Nakano, T., and Inoue, Y., 2013. Study of growth enhancement of multiwalled carbon nanotubes by chlorine-assisted chemical vapor deposition. *Japanese Journal of Applied Physics*.

Gupta, N., Gupta, S.M., and Sharma, S.K., 2019. Carbon nanotubes: synthesis, properties and engineering applications. *Carbon Letters*, 29 (5), 419–447.

Iijima, S., 1991. Helical microtubules of graphhitic carbon. *Nature*, 354, 56–58.

Kuzmany, H., Kukovecz, A., Simon, F., Holzweber, M., Kramberger, C., and Pichler, T., 2004. Functionalization of carbon nanotubes. *Synthetic Metals*, 141 (1–2), 113–122.

merging-issues/lead-and-cadmium [Accessed 27 Feb 2020].

Mallakpour, S. and Khadem, E., 2016. Carbon nanotube–metal oxide nanocomposites: Fabrication, properties and applications. *Chemical Engineering Journal*, 302, 344–367.

National departments _ South African Government-name change of departments [online], 2019. Available from: https://www.gov.za/about-government/government-system/national-departments [Accessed 13 Feb 2020].

Nieto-Márquez, A., Valverde, J.L., and Keane, M.A., 2007. Catalytic growth of structured carbon from chloro-hydrocarbons. *Applied Catalysis A: General*, 332 (2), 237–246.

Planeix, J.M., Coustel, N., Coq, B., Bretons, V., Kumbhar, P.S., Dutartre, R., Geneste, P., Bernier, P., and Ajayan, P.M., 1994. Application of carbon nanotubes as supports in heterogeneous catalysis. *Journal of American Chemical Society*, 116 (17), 7935–7936.

RSA Government, 1998. *National Water Act 36 of 1998. Government Gazette*.

Sadegh, H., Shahryari Ghoshekandi, R., Masjedi, A., Mahmoodi, Z., and Kazemi, M., 2016. A review on Carbon nanotubes adsorbents for the removal of pollutants from aqueous solutions. *International Journal of Nano Dimension*, 7 (2), 109–120.

Sharma, A., Gudala, S., Ambati, S.R., Penta, S., Mahapatra, S.P., Vedula, R.R., Pola, S., and Acharya, B., 2017. Synthesis of heterocyclic compounds catalyzed by metal/metal oxide-multiwall carbon nanotube nanocomposites. *Journal of the Chinese Chemical Society*, 64 (6), 589–606.

Singh, C. and Song, W., 2001. Carbon nanotube structure, synthesis, and applications. In: K. Donaldson, C. Poland, R. Duffin, and J. Bonner, eds. T*he Toxicology of Carbon Nanotubes*. Cambridge: Cambridge University Press, 1–37.

Tripathi, A. and Rawat Ranjan, M., 2015. Heavy metal removal from wastewater using low cost adsorbents. *Journal of Bioremediation & Biodegradation*, 06 (06).

Wang, L., Li, J., Jiang, Q., and Zhao, L., 2012. Water-soluble Fe_3O_4 nanoparticles with high solubility for removal of heavy-metal ions from waste water. *Dalton Transactions*, 41 (15), 4544.

WHO, 2014. Drinking Water and Sanitation Progress on. *Unicef*.

Yang, J., Hou, B., Wang, J., Tian, B., Bi, J., Wang, N., Li, X., and Huang, X., 2019. Nanomaterials for the removal of heavy metals from wastewater. *Nanomaterials,* 9 (3), 424.

Chapter 2

Literature review

2. Brief introduction

In this chapter a detailed review of the literature relating to wastewater contaminants and their removal, in particular heavy metals is discussed. The synthesis, properties, modification, and applications of the metal oxide modified carbon nanomaterials as adsorbents will also be reviewed.

2.1. Water scarcity and pollution

As a result of rapid growth in urbanization and industrialization, freshwater supplies are becoming scarce. Amongst others, industries that discharge contaminated wastewater to the water bodies without first treating them elevate the problem. It was estimated that about 20% of the world's wastewater was properly treated in 2015 (Zhang *et al*., 2016). The water scarcity study by International Water Management Institute (IWMI) (World Water Vision: Its Origin and Purpose, 2000) anticipated that by 2025 about 1.8 billion of the human population will be living in regions or countries with total water scarcity. Lately, most countries in the Middle East and North Africa are categorized as having total water scarcity. However, Pakistan, South Africa and huge parts of India as well as China, will be included by 2025. The aforementioned report is corroborated by WHO (2014), as it was estimated that there will be a water shortage affecting 50% of the world's population by 2025 and the projection of this water scarcity is presented in Figure 2.1.

Both projections are coming to existence in South Africa. Metropolitan areas such as Nelson Mandela Bay, Gauteng, eThekwini and other smaller municipalities are water-stressed and this eventually affect everyone in South Africa. Hence, the metropolitan areas and municipalities occasionally have water restrictions (Eberhard, 2018). The areas that had limited water problems before the projections are at their worst and their water problems are not lesser than that of the popularised Cape Town. However, the Cape Town drought that intensified in 2017/2018 and then subsided later in 2019, not forgetting the countdown to "day zero"; received higher attention, as the city is well known worldwide as a tourist destination and South Africa's economic hub (Ziervogel *et al*., 2019).

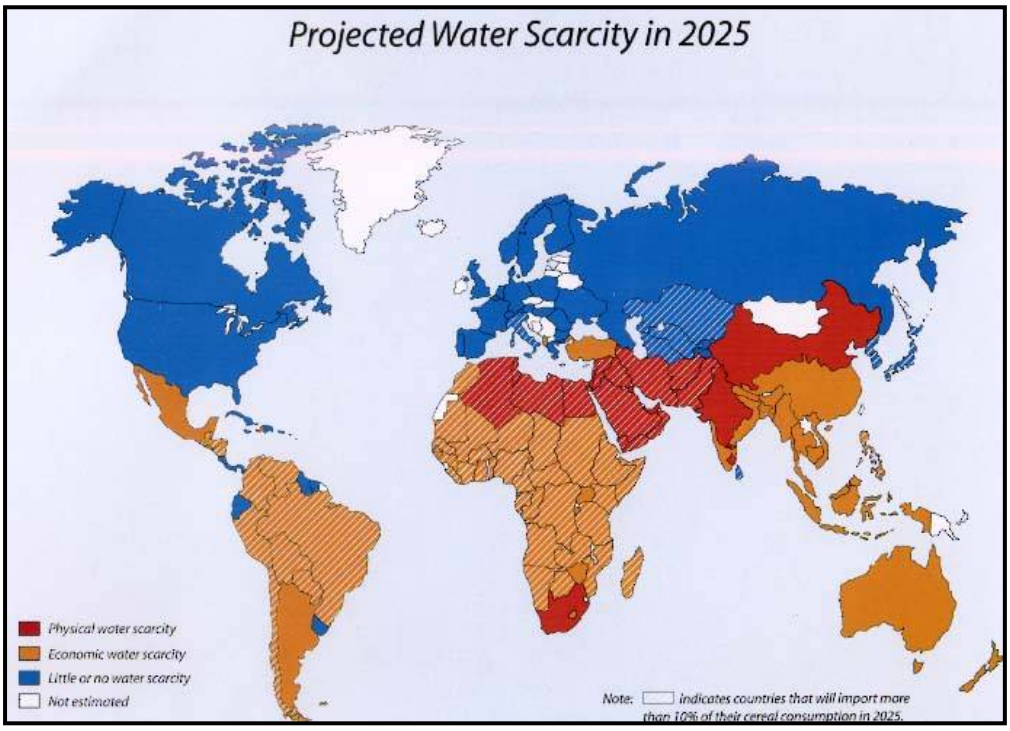

Figure 2.1: Future Projection Water Scarcity, adapted without modification from (Lingamdinne *et al*., 2019).

Other factors that contribute to water scarcity are lack of adequate wastewater treatment facilities and water pollution by various pollutants such as dyes, heavy metals, oils, pesticides as well as radioactive substances. Water pollution is the introduction of foreign elements, or compounds into water sources at a concentration that is not acceptable. Water pollution has an enormous impact on the living organisms, ecosystems and/or biodiversity (Fernández-Luqueño *et al*., 2013). The pollutants that are released into the water sources, can be either intentional or unintentional. The water pollution problem that arose in South Africa recently at the Vaal River (Emfuleni Municipality in the Vaal), was due to the bust of the water system pipes whereby the Ekurhuleni Water Care Company (Erwat) and South African National Defence Force (SANDF) were enlisted to assist the Emfhuleni municipality to combat this problem (defenceWeb, 2019). This incident had severe consequences, wherein it amplified the water scarcity problem as the country is experiencing drought. Besides this incident, there are a series of activities which can also contribute to water pollution listing different pollutants as per their activities.

The common sources of water pollution adapted from (Singh and Gupta, 2017) without modification are shown in Figure 2.2. The common sources of pollutants from industries in wastewater are heavy metals.

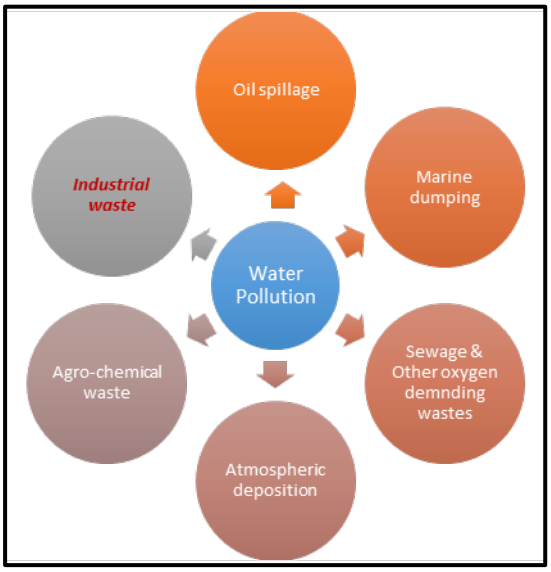

Figure 2.2: Sources of water pollution.

2.2. Heavy Metals

Metals with high densities are identified as heavy metals (Igwe, 2007). They are non-recyclable and can accumulate in living organisms triggering several health problems. The two main contributors to heavy metals release are mining and weathering of volcanic eruptions. The number one source of water pollution is heavy metal contamination (Bailey *et al*., 1999). Heavy metals include metals such as As, Cd, Cr, Cu, Ni, Zn, Hg and Pb. Some of the heavy metals such as Zn, Fe, and Cu are needed by the human body as a source of nutrients and for metabolism. However, their concentration must be limited since in higher concentrations they can be highly toxic leading to compromised quality of water. Moreover, at low concentrations heavy metals can accumulate and be persistent in the soil until they enter the food chain through the intake by plants. One of the common heavy metal in wastewater is lead (Pb). Thus, the focus of this research project is on the removal of Pb^{2+} ions from wastewater using an adsorption technique.

2.2.1. General overview of Lead (Pb)

Lead (Pb) exists in lesser quantities in the earth's crust and occurs naturally as a bluish-grey metal (Tchounwou *et al*., 2010) as depicted in Figure 2.3(b). Figure 2.3(a) shows the chemical information of Pb. It can be classified as metallic, organic and inorganic.

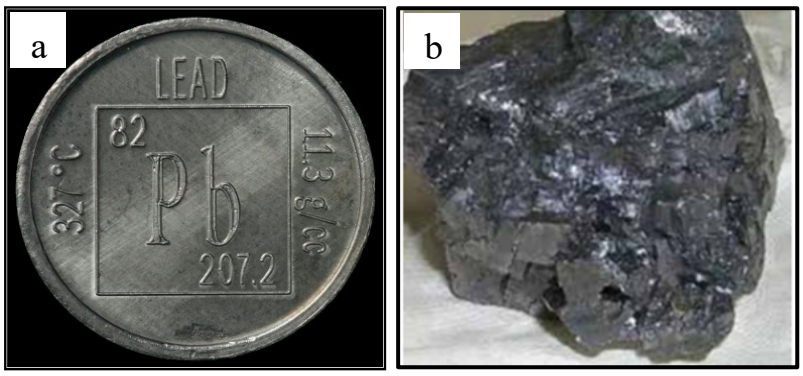

Figure 2.3: Example of Pb; (a) chemical information and (b) sample.

According to the Department of Water and Forestry (DWF) (DWF,1996), the South African Quality guidelines limit the amount of lead in different water uses, without health implications as tabulated in Table 2.1 below.

Table 2.1: South African Water Quality Guidelines Pb.

Type	**Limit (mg/L)**
Aquatic	0.0002
Domestic	0.1
Agriculture	
Livestork	0.5
Irrigation	0.2
Aquacalcure	0.01

2.2.1.1. Sources and uses of lead

Countries that were leading in 2009 for producing lead worldwide in their ranking order are China, Australia, United State of America (USA), Peru, Mexico, Canada, India, Bolivia, Poland, Russia, Sweden, Ireland and South Africa (Lead Producer Countries and their Percentage in World Production, 2009). However, in 2017 and 2018 there was a decline in the production of lead in countries such as China, Australia, Kazakhstan, Peru, South Africa and

USA; which accounts for 49 % of the global output (Global lead output set to bounce back in 2019). Lead is generally found in rocks that are in the earth's crust. Characteristics such as a low boiling point, soft, malleable, poor conductor of electricity, fire resistance and resistance to corrosion, make it versatile (Boldyrev, 2018). Thus, it is ideal to be used in a variety of commercial products such as ammunition, cable sheathing, devices to safeguard X-rays, cosmetics and lead-acid batteries as depicted by Figure 2.4. Industries, agricultural and domestics sites also utilizes lead in their daily activities. Lead is found in the environment as a result of these human activities (Tiwari *et al*., 2013), which causes lead to be present in soils, plants and water (Farid, 2016). The large source of lead was found in the use of lead pipe in the plumbing system of old homes (Sankhla *et al*., 2016).

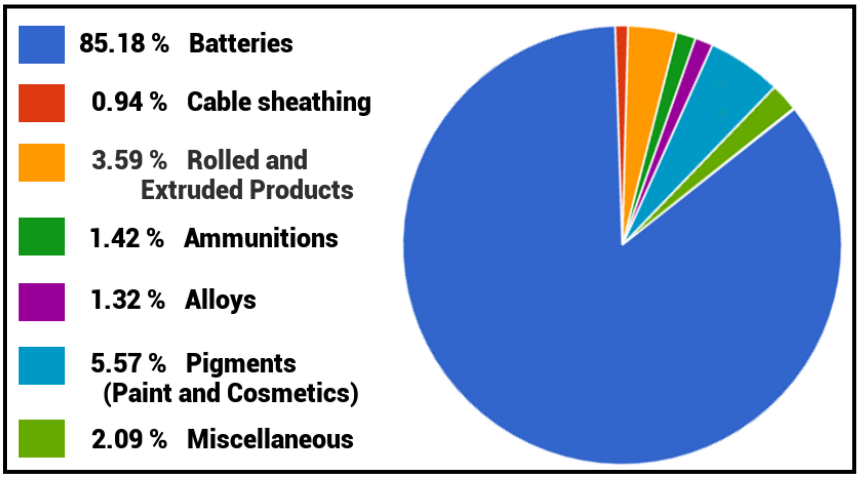

Figure 2.4: Sources and uses of Pb, adapted without modification from (ILA, 2012).

2.2.1.2. Health implications of Pb

Pb is harmful to the human body even at trace amounts as compared to its metal counterparts such as iron and zinc since these metals are vital to the human body at certain levels. Water that is polluted by Pb needs to be properly treated, prior to being discharged to the water receiver. If ingested or inhaled by human beings accidentally or intentionally, Pb will affect most organs in the body. It is commonly used commercially which leads to its widespread and exposure to the human beings (WHO, 2015). The effect of Pb toxicity in adults and children is different, as depicted in Figure 2.5. In children, the effect is extremely severe, as it is retained for longer periods especially for those that are below the age of 5. In addition, its effect also varies on the different human body parts. The exposure can be through drinking water, food, and dust (soil and air). Thus, Pb poisoning can be acute or chronic and it is associated with a variety of symptoms.

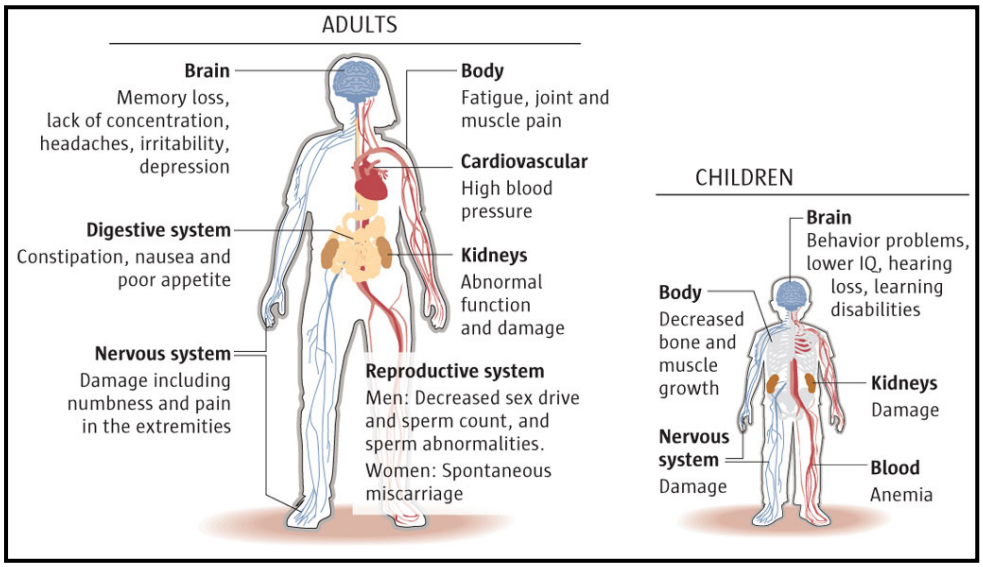

Figure 2.5: Health implications of Pb, adapted without modification from (Panchangam, 2015).

2.3. Brief discussion on carbon and metal oxide nanomaterials

Nanomaterials possess properties such as huge capacity and high selectivity, which makes them ideal sorbent materials for reducing the amount of organic/inorganic pollutants in wastewater (Chawla *et al*., 2015). Nanoadsorbents are the preferred nanomaterials to be used in adsorption, as they are efficient and effective in the elimination of organic and inorganic pollutants from water. Nanomaterials such as dendrimers, quantum dots, metal-oxide nanoparticles, CNTs are among others used in the treatment of water. The morphology of various types of nanomaterials are presented in Figure 2.6.

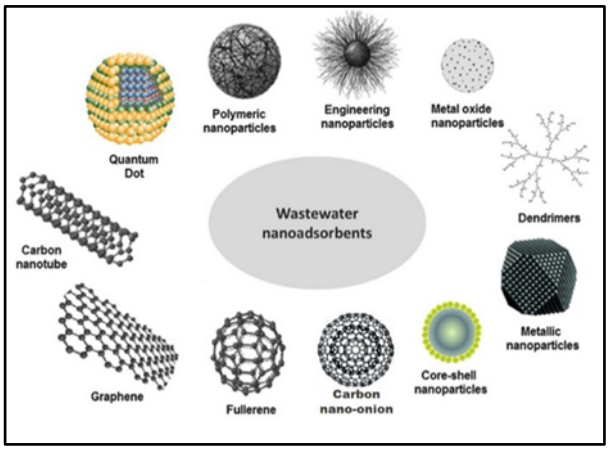

Figure 2.6: Different types of nanomaterials used in water treatment, adapted with modification (carbon nano-onion) from (Cerro-Lopez and Méndez-Rojas, 2019).

2.4. CNTs as adsorbents

Properties such as high adsorption capacity, good regeneration capability, and thermal stability are associated with CNTs, which make them ideal candidates for adsorption. Recently, the properties of CNTs such as high aspect ratios, large surface areas, nano-sized stability and rich surface chemical functionalities have made them useful in many applications (Wu *et al*., 2011). Thus, MWCNTs and SWCNTs have attracted great interest as supporting materials, due to their excellent properties such as high surface area and chemical stability. As a result of their exceptional physio-chemical properties, MWCNTs have been utilized in numerous diverse industrial applications (Mihalchik *et al*., 2015). Sadegh *et al*., (2016) stated that CNTs have unique structural characteristics which make them useful adsorbents for the elimination of pollutants. The advantages of using CNTs as adsorbents are their; (i) large specific surface area, (ii) abundant capacity to absorb an extensive variety of toxins, (iii) selectivity towards aromatics, and (iv) fast kinetics (Lu *et al*., 2016).

2.4.1. Structure of CNTs

CNTs are the allotropes of carbon within the fullerenes family, wherein fullerenes were discovered in 1985 (Kroto *et al*., 1985). This are nanomaterials that are sp^2 hybridized, with sheets of graphene layers that are rolled up forming a cylinder, denoted by the pair of indices (i.e. n, m, as shown in Figure 2.7) (Gupta *et al*., 2019). Based on the vector of their chirality in which SWCNTs (i.e. integers (n, m)) is folded, it will result in the geometries such as armchair (i.e. n=m (n, n), zigzag (n, 0) or chiral (n>m>0), refer to Figure 2.7**)** (Dervishi *et al*., 2009; Prasek *et al*., 2011; Eatemadi *et al*., 2014).

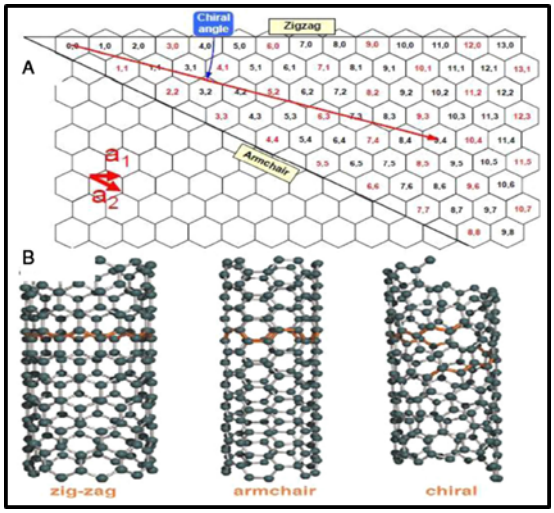

Figure 2.7: Different model structure of SWCNTs adapted without modification from (Eatemadi *et al*., 2014).

There are two types of CNTs that can be isolated namely the single-walled carbon nanotubes (SWCNTs) which contain a single layer of graphene and the multi-walled carbon nanotubes (MWCNTs) which contains multiple concentric layers of graphene. Multi-walled CNTs were the first to be discovered in 1991 by Ijima (Iijima, 1991), whilst SWCNTs were discovered later in1993 by Ijima and Ichihashi (Iijima and Ichihashi, 1993), (Figure 2.8).

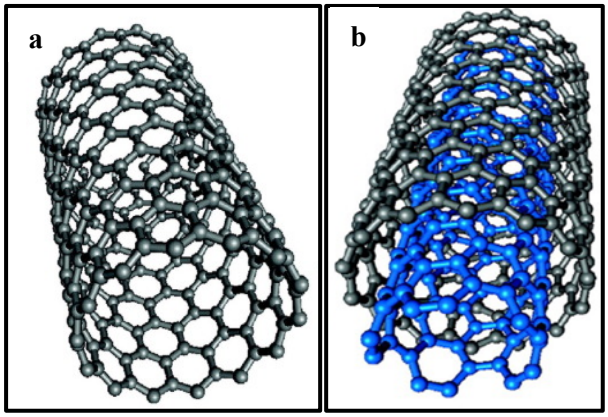

Figure 2.8: Different types of CNTs: (a) SWCNTs and (b) MWCNTs, adapted without modification from (Santhosh *et al*., 2016).

The structural model of MWCNTs has two forms, namely ; the Russian doll (i.e. the concentric tubes have a varying diameter inside it) and Parchment model (i.e. single graphene that is rolled multiplying in a spiral form), as shown in Figure 2.9 (Gupta *et al*., 2019).

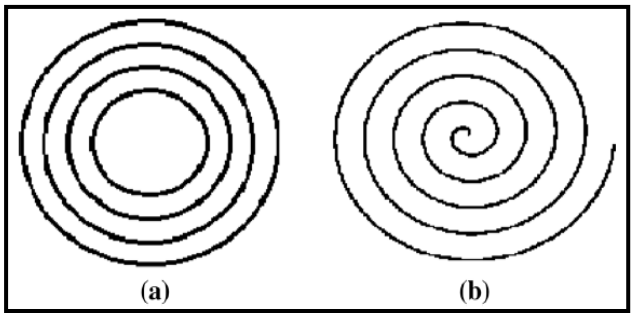

Figure 2.9: Structural model of MWCNTs (a) Russian doll and (b) Parchment.

2.4.2. Synthesis of CNTs

The common techniques used in the production of CNTs are laser ablation, arc discharge and chemical vapour deposition (CVD). CVD is the most preferred technique because of low cost, low power output, materials are synthesized at the low-temperature range, it is simple and it yields relatively high purity materials (Purohit *et al*., 2014). The schematic diagram of CVD adapted from, Maboya *et al*.(2016) is presented in Figure 2.10 without modification.

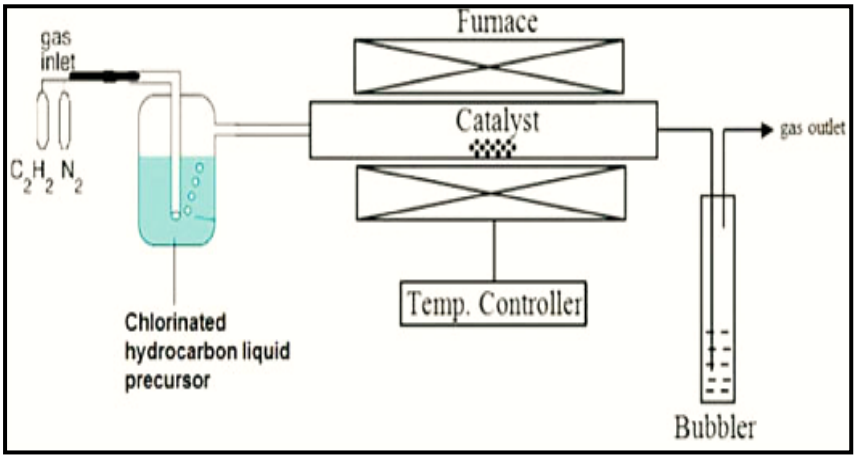

Figure 2.10: Set up of the CVD reactor.

CVD involves the process of placing a substrate-metal catalyst inside a furnace. The carrier gas can be N_2 which is used to prevent oxidation inside the furnace at the required flow rate during the reaction and then C_2H_2 is flown through the reactor tube as the source of carbon.

Thereafter, when the desired temperature is reached, the growth of CNTs is initiated (Aqel *et al*., 2012). In this case, factors such as catalyst nanoparticles size, reaction time, temperature and flow rate of the gases affect the quality and diameter of the CNTs. Apart from the CVD technique, arc discharge method is another technique that is used to synthesize CNTs (as depicted by Figure 2.11).

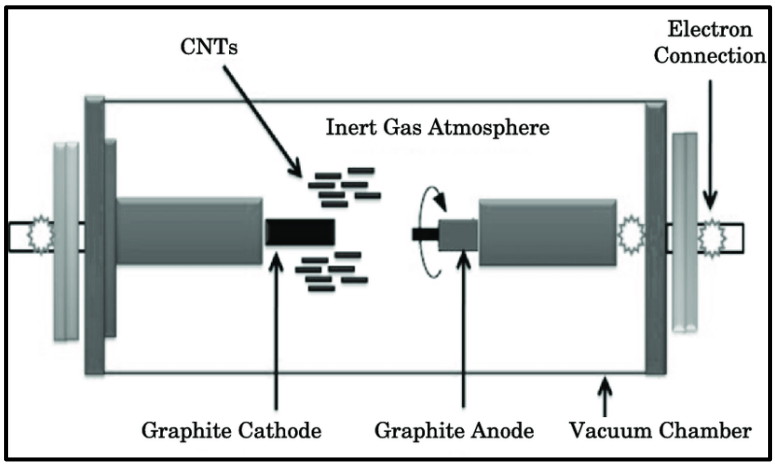

Figure 2.11: Set up of arc discharge, adapted without modification from (Mehra and Jain, 2014).

The arc discharge method involves two graphite rods which are separated by the required length and are connected to the anode and the pure cathode respectively. The anode and cathode is doped with a metal catalyst and are enclosed within an inert gas atmosphere (Aqel *et al*., 2012). A direct current is driven by potential differences and then the two electrodes within them create a high-temperature arc discharge. It is used to vaporize carbon atoms into plasma which results in the formation of SWCNTs. However, this method has difficulties in aligning the growth of the CNTs and consumes a lot of energy even though there is no catalyst used (Golnabi, 2012). Alternatively, lase ablation method can be employed to produce CNTs. The schematic diagram of laser ablation is presented in Figure 2.12.

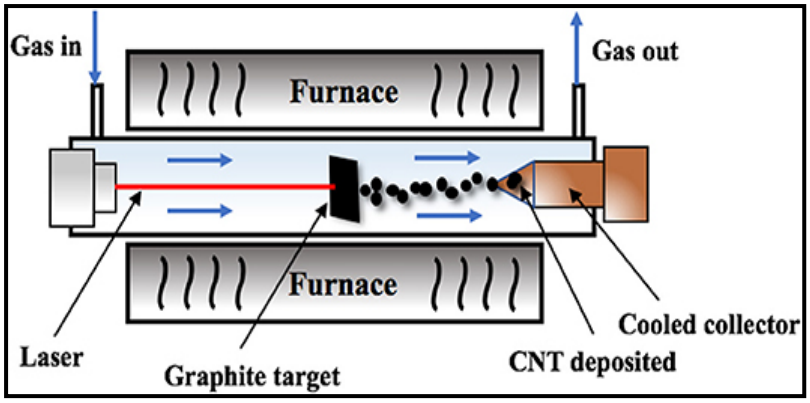

Figure 2.12: Set up of laser ablation method, adapted without modification from (Lu *et al*., 2019).

The laser ablation method involves a laser beam under an inert atmosphere in a high temperature that is used to vaporize the graphite target. This method allows for production of carbon species (e.g. CNTs) wherein the inert gas sweeps them from a high-temperature area to a conical water (i.e. cooled upper collector) (Golnabi, 2012). Thus, SWCNTs can be produced by adding transitional metal such as Ni, Fe or Co to the carbon target (Golnabi, 2012). The quantity and quality of CNTs are affected specifically by temperature, laser, catalyst growth, growth temperature and nature of gases (including their flow rate).

2.4.3. Properties of CNTs

CNTs are large in terms of surface area and aspect ratio (Gupta *et al*., 2019). They have demonstrated distinctive properties that are not limited to thermal, mechanical and electrical; that are ideal in several applications as discussed below.

2.4.3.1. Thermal properties of CNTs

CNTs are relatively stable in high temperature (Rosso, 2001). They are influenced by their distinctive structure and small magnitude. They are good conductors alongside the tube-showing ballistic conduction properties, whilst being good insulators laterally to the axis of the tube (Varshney, 2014). This nanomaterial at room temperature has a thermal conductivity that transmits 600 $W.m^{-1}.K^{-1}$, which is superior to the renowned thermal conductor copper transmitting 385 $W.m^{-1}.K^{-1}$ (Varshney, 2014). The thermal conductivity of CNTs is at least twice that of diamond (Gupta *et al*., 2019).

2.4.3.2. Mechanical properties of CNTs

Flexible CNTs are stronger especially in the axial direction, while soft in radial area. Their strength is due to the sp^2 bonds within each carbon and/or C-C covalent bond and its hexagonal network structure. Moreover, the mechanical strength is two hundred times more than that of steel, even though it is lighter in weight. The radial direction of CNTs is ideal for the formation of its nanocomposites. Furthermore, given their good mechanical properties, CNTs are exposed to a huge distortion in the diagonal direction when a load is applied to the structure of the composite which they are incorporated. CNTs have the highest Young's Modulus between 270 and 950 GPa that is dependent on the diameter of the tube, but not on the chirality of the tube (Meyyappan, 2005). Their tensile strength is in the range of 11-63 GPa and a density of 2.6 g/cm^3 (Yu *et al*., 2000). Hence, the density is relatively low, with a higher aspect ratio. The individual atoms are greater than diamonds (sp^3 and alkene). This type of nanoparticles are weak under compression, as results of the hollow structure and high aspect ratio.

2.4.3.3. Electrical properties of CNTs

The electrical properties of CNTs usually depend on the orientation and diameter of the hexagons (i.e. armchair, zig-zag and chiral) exhibiting properties such as metallic semiconducting. Their energy gap is reduced as the diameter of the CNTs increases. It also can carry huge currents than metals, as a result of low resistivity and tiny heat dissipation. They have minimal resistance and extremely little defects along their structure, due to higher electrical conductivity that exceeds that of copper (Dervishi *et al*., 2009). The carrying capacity of CNTs, is extremely a huge current, surpassing that of superconductors (Gupta *et al*., 2019). This property is ideal for electrical wiring application (Gupta *et al*., 2019). CNTs are reported to have an electrical resistivity as little as 10^{-6} Ω-m, which usually changes with structural modifications (Meyyappan, 2005). Ajayan (1999) reported that dopants such as nitrogen and boron can increase the electrical conductivities of CNTs, causing them to be p- and n-type. The electrical conductivity of the MWCNTs or SWCNTs is amplified, as a result of intercalation of the various metals within the tubes and the chemical dopants (Dervishi *et al*., 2009).

2.4.4. Structural modification of CNTs

In order for CNTs to be applicable in various fields, it requires them to be dispersible in solutions. However, CNTs cannot be dispersed in aqueous solutions, due to weak Van der Waals forces that they exhibit (Mallakpour and Khadem, 2016; Gupta *et al*., 2019). Thus, the

need for surface modification of the CNTs, that will reduce their accumulation and improves their dispersion in various solvents and medium. Functionalization can either be covalent or non-covalent. Through non-covalent functionalization, CNTs retain their original structure and properties, as it involves the delocalization of the π electrons of the CNTs, which are commonly joined with the conjugated compounds through the Van der Waals forces, π-π stacking interactions, hydrogen bonds and electrostatic forces (Mallakpour and Khadem, 2016). Unfortunately, this is easily controlled and impose difficulties in characterization of CNTs due to weekly bonded molecules that results in desorption, leaving the functionalized CNTs to re-aggregates (Gupta *et al*., 2019). Covalent bonding creates the sp^3 carbons that disrupts the transition band of the π electrons in the conductivity and mechanical properties of the CNTs (Gupta *et al*., 2019).

2.4.4.1. Functionalization of CNTs

There are different forms in which functionalization of CNTs can be achieved which includes introducing functional groups such as hydroxyl groups through oxidation. Functionalization plays an essential role in the adsorption properties of the CNTs especially for the uptake of metal ions (Gadhave and Waghmare, 2014; Liu *et al*., 2013; Cho *et al*., 2010). Thus, this exposes the active sites, due to electrostatic chemical bonding. Notably, the common functionalized treatment is oxidation using oxygen.

2.4.4.2. Oxidation of CNTs

Oxidation of CNTs is the treatment that can be achieved through the use of highly concentrated acids such as HNO_3 and H_2SO_4. The acids usually introduce functional groups such as –COOH, −OH and −C=O−, along the sidewalls of the CNTs (Liu *et al*., 2013; Herrera-Herrera *et al*., 2012). Oxidation helps with the removal of catalyst and amorphous carbon (Wepasnick *et al*., 2010); which are a hindrance in exploring the properties and characterization of the CNTs (Yuan *et al*., 2008). In addition, it also allows for better attachment of metal/metal oxides (Sharma *et al*., 2017). Thus, it is ideal for the adsorption of hydroxyl groups of the aforementioned oxides and or relatively low molecular weight and polar pollutants (Lin and Xing, 2008). Moreover, functionalized MWCNTs gives a huge electrical repulsive force between the acid treatment, in which it eliminates tangling and agglomeration among them (Mallakpour and Khadem, 2016). The attached functionalized groups can be identified using X-ray photoelectron spectroscopy (XPS), from the spectral deconvolution of the O1s or C1s

XPS region (Wepasnick *et al*., 2010). However, the π-π make up feature must be taken into consideration for the C1s and also the oxygen having the same binding energies cannot be differentiated (i.e. alcohol, C−OH versus ethers, C−O−C) (Wepasnick *et al*., 2010).

2.4.4.3. Chlorination of CNTs

Modification of the surface of CNTs can also be achieved via chlorination. Chlorination of the carbon nanomaterials has been shown to (1) enhance the growth of CNTs without damaging their crystalline structure (Ghemes *et al*., 2013; Nieto-Márquez *et al*., 2007), (2) act as a purifying agent (Yuan *et al*., 2008) and initiate surface restructuring (Nieto-Márquez *et al*., 2007). Kónya *et al*., (2002) and Pełech *et al*., (2013) reported studies on the efficient chlorination of CNTs. Whilst Ray *et al*., (2007) reported that the electronic as well as the structural properties of nitrogen doped CNTs, can be altered when functionalized with chlorine via the plasma atmosphere. In the latter study, an observation was made that magnetic properties were altered significantly by chlorine and oxygen functionalization (Ray, 2018). The interaction of the cationic species during adsorption was enhanced by the introduction of Cl (Osikoya *et al*., 2015). However, the adsorption efficiency was lower than those obtained using raw CNTs. It was reported that the source of Cl has an effect on the morphology of the CNTs. In this case, trichloroethylene (TCE) and tetrachloroethane (TTCE) yielded "bamboo-like" structures, whilst TCE and dichlorobenzene (DCB) revealed growth of secondary nanofibres and nanoparticles onto the outerwalls of the main CNTs (Maboya *et al*., 2016). This correlate with the study that was conducted by Pełech *et al*. (2012) where carbon tetrachloride (CCl_4) was used in the liquid phase as a source of chlorine and resulted in formation of "bamboo-like" morphology with open tips. Chlorination also resulted in production of CNTs that contained pentagons and heptagons that were less stable than hexagons of the CNTs (Pang *et al*., 1993). Chlorination was reported to be a better substitute as compared to fluorination since the later was corrosive (Barthos *et al*., 2005). It was reported that the use of liquid halogens as functionalizing agents were more effective compared to use of gaseous halogens (Pełech *et al*., 2012) and *(*Barthos *et al*., 2005). Both energy dispersive spectroscopy (EDS) and XPS can be used to identify the inclusion of the chlorine on the CNTs.

2.4.4.4. Doping of CNTs

Doping of CNTs involves the replacement of carbon atoms in their structural matrix by another adatom. It can be achieved in three different ways; (i) endohedral (i.e. filling the inside with

dopants), (ii) exhohedral (i.e. insertion of the dopants among the concentric rings or layers), and (iii) substitution doping (i.e. replacement of the carbon with the dopants the most commonly achieved doping) as reported by Ayala *et al*., (2010). In 1994, the study of doping of CNTs with boron (B) and nitrogen (N) was done through electric discharge method (Stephen *et al*., 1994). The localized electronic states might occur as a result of extrinsic doping causing the nanotube to be chemically active due to smoothness disturbance and have a largely chemically inert nanotube π-cloud (Ewels and Glerup, 2005). Thus, doping is one of the methods commonly used to functionalize nanomaterials such as CNTs. It activates the sites along the nanotubes, leading to an increased surface reactivity (Ewels and Glerup, 2005).

The introduction of nitrogen as a dopant in CNTs allows for CNTs to exhibit the distinctive morphology that is "bamboo-like structure" or nanobell (Ewels and Glerup, 2005). XPS is one of techniques used to evaluate the doping achievement on CNTs through quantifying and qualifying the present nitrogen atoms (Ewels and Glerup, 2005). The N-CNTs tends to coil in the inner region, due to inclusion of the pentagons into graphite network that is facilitated by nitrogen. They also exhibits metallic behaviour just above the Fermi level (Ewels and Glerup, 2005). The N dopant alters the behaviour of the CNTs that are influenced by the nature of the surrounding carbon lattice, resulting in higher tube wall buckling, stability, coiling and intense reactivity (Ewels and Glerup, 2005).

2.5. Iron oxide nanoparticles

The iron is regularly used and is one of the most abundant elements on earth (Chaki *et al*., 2015). In nature, iron is commonly found in combination with other elements (e.g. iron and oxygen and/or sulphur) since it is highly reactive especially under certain conditions. Thus, oxides of iron can be formed and are members of the ferromagnetic family in the class of magnetic materials (Dadfar *et al*., 2019). The maghemite (γ-Fe_2O_3), magnetite (Fe_3O_4) and hematite (α-Fe_2O_3), are the three common forms of iron oxide. In most cases, the preferred magnetic iron oxide is Fe_3O_4, due to its unique properties. The structure of Fe_3O_4 is presented in Figure 2.13 below.

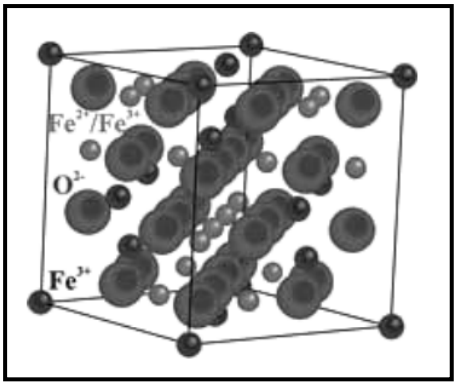

Figure 2.13: Structure of Fe_3O_4 unit cell, adapted without modification from (Blaney, 2007).

Fe^{2+} and Fe^{3+} are the two ions with opposing magnetic moments in which the ferromagneticity is inadequate when they form Fe_3O_4 nanoparticles (Mazrouaa *et al*., 2019). The crystal structure of the Fe_3O_4 is cubic spinel based on the 32 oxygen ions, with a closed packed arrangement along the direction of 111-miller indices. In this case, half of the octahedral sites are occupied by the ferrous ions as a results of superior crystal field stabilization energy. The remaining half is occupied by the ferric ions (adjacent to ferrous ions) and as well as the entire tetrahedral sites (Mazrouaa *et al*., 2019; Cornell and Schwertmann, 2003). The adjacent of ferrous ions to the adjascent ferric ions in the octahedral sites permits the bouncing of electrons between the d-orbitals of the two cations (Mazrouaa *et al*., 2019). The units cell of the magnetite follow the face-centred cubic arrangement that has a crystal lattice parameter α= 0,8396 nm (Cornell and Schwertmann, 2003). As depicted in Figure 2.13, it can be seen that eight formula unit (i.e. z-parameter inside the individual unit cell of magnetite) exist in the crystal lattice of Fe_3O_4 (Blaney, 2007).

2.5.1. Synthesis of Fe3O4

The biological, chemical and physical processes are the three aspects used in categorizing the methods used in the synthesis of nanoparticles such as Fe_3O_4 (Dave and Chopda, 2014). There are various chemical methods that are superior due to their simplicity, viability and reproducibility. Methods such as; co-precipitation, sol-gel, and hydrothermal technique can be used effectively to synthesize Fe_3O_4 nanoparticles. However, among them, co-precipitation is the most preferred method because it is the most simplest and inexpensive. Co-precipitation employs a relatively low temperature, while the solvents used are pleasant to the environment

and results with a product (NPs) that has high yield with a moderate narrow size distribution (Chen and Meng, 2017).

On the other hand, sol-gel method has a good stoichiometric control with a shorter reaction time at a low temperature that produces ultrafine particles with a narrow size. The four stages of sol-gel formations are; (i) hydrolysis, (ii) condensation, (iii) particle growth, and (iv) agglomeration of particles. The route involves using a metal salt mixture co-precipitated by a base in which a colloidal solid solution can be formed whenever a metallo-organic or inorganic precursor is not formed resulting into a concentrated gel. The hydrothermal method uses low temperatures for processing and this makes it an economical method that has a high degree of compositional control (Nejati and Zabihi, 2012). The catalyst is usually added to control pH and initiate the reaction (Morita *et al*., 2004). This involves a chemical reaction with a solvent in a closed system under specific conditions. Sometimes modification of the particle size is controlled by addition of surfactants. Thus, the synthesized nanoparticles can be applied in various disciplines specifically chemistry, medicine, optics, sensor, energy conversion and environment (e.g. waste water treatment).

2.5.2. Properties of Fe_3O_4

2.5.2.1. Physical properties of Fe_3O_4

The Fe_3O_4 has Fe cations that fills the tetrahedral and octahedral sites while the oxygen atoms form face centred cubic-closed packing. It has diameters of about 5 to 20 nm that contains a single domain. It is a metallic lustre that has a dense black colour and the density of 5.18 g/cm^3 (Blaney, 2007). Moreover, its boiling and melting point is around 2326 °C and 1590 °C respectively (Blaney, 2007). There is a cubic crystal structure of the Fe_3O_4 which has closed packed atomic arrangement (Teja and Koh, 2009). However, Fe_3O_4 generally occurs as octahedral crystals and rhombo-dodecahedra in its natural or synthetic form (Cornell and Schwertmann, 2003). Notably, the Fe_3O_4 nanoparticles are not porous (Cornell and Schwertmannm, 2003).

2.5.2.2. Magnetic properties of Fe_3O_4

Fe_3O_4 has the strongest magnetism as compared to the other transition metal oxide forms (Cornell and Schwertmann, 2003). Their magnetic behaviour emanates from the vacancy of the four unpaired electrons in the 3d orbitals (Teja and Koh, 2009). Their magnetic properties are influenced by composition and morphology. Based on the respective occupancy of Fe^{2+} in

the octahedral site and Fe^{3+} in the octahedral and tetrahedral sites, they have resulted in the formation of two interpenetrating magnetic sub-lattices (Cornell and Schwertmann, 2003). The Fe_3O_4 can also be superparamagnetic, when it has no hysteresis loop for an individual domain (Teja and Koh, 2009).

Magnetite has a Curie temperature of 850 K, whilst at room temperature it is ferrimagnetic ((Blaney, 2007; Cornell and Schwertmann, 2003). When there is a temperature increase to the Curie temperature, the thermal instabilities abolish the ferromagnetic alignment of magnetic moments on the sites of the tetrahedral, which results in the weakening of the ferrimagnetic strength (Blaney, 2007). As Curie temperature is achieved, the magnetization becomes zero resulting in superparamagnetism (Blaney, 2007). The composition and morphology influence the magnetic properties of the magnetite.

2.5.2.3. Electrical properties of Fe_3O_4

Fe_3O_4 has the lowest resistivity as compared with its counterparts in the oxides family, as a results of its band gap (i.e. 0.1 eV) which makes it a conductive metallic material (conductivity: 10^2-10^3 Ω^{-1} cm^{-1}) (Cornell and Schwertmann, 2003). However, the occupancy affects its electrical properties in which the split occupancy by Fe^{2+} and Fe^{3+} in the octahedral sites allows for easier movement of the holes from Fe^{2+} to Fe^{3+}. Moreover, the octahedral sites have vacancies that cause the Fe_3O_4 to be a fairly metal deficiency, affecting it to either be n- or p-type semiconductor (Cornell and Schwertmann, 2003).

2.6. Application of nanomaterials in wastewater treatment

As previously reported, the adsorbent such as NiO/CNTs nanocomposites were suitable for the elimination of Pb^{2+} from aqueous solutions (Navaei Diva *et al*., 2017). The MWCNTs/Fe_3O_4 composites also performed well in removing 2,4-dichlorophenol and Cu^{2+} from water, which provided a good method in the water treatment application (Dong *et al*., 2009). In addition, the sorbent material, iron oxide and multi-walled carbon nanotubes hybrid was successfully used in the removal of arsenic in water (Ntim and Mitra, 2012). Furthermore, lead ion from aqueous solution was effectively removed by an adsorbent made of alumina-multiwalled carbon nanotubes material (Gupta *et al*., 2011). Adsorption studies were also done on raw CNTs versus CNTs infused with iron oxide nanoparticles (Fe_xO_y-NPs) for the removal of benzene in water and showed that the Fe_xO_y-NPs/CNTs NPs had higher removal efficiency as compared

to raw CNTs (Abbas *et al*., 2016). Specifically, $CoFe_2O_4$/MWCNTs composite was efficient in eliminating methylene blue due to its higher adsorption capacity (Farghali *et al*., 2012).

Hence, the use of nanomaterial for the removal of heavy metals from wastewater among other things has been a focus for many researchers. Table 2.2 gives a summary of wastewater treatment using different nanomaterials. Studies listed in this table report that the majority of CNTs were used in the composite form and their effectiveness resulted in different adsorption capacity and efficiency. This can be due to different reaction conditions in which the studies were conducted. Thus, the results obtained adsorbing Pb^{2+} ions cannot be compared against each other. Notably, Kabbashi *et al*., (2009) used CNTs to obtain maximum adsorption capacity of 102 mg/g and the adsorption efficiency of 93 %. In the case of Fe_3O_4/CNTs as a adsorbent, it has resulted in a maximum adsorption capacity of 65,40 mg/g (Zhang *et al*., 2012). However, in both instances the nanomaterials did not have Cl and N adatoms.

Table 2.2: Summary of the adsorption studies of lead using nanomaterials as adsorbents.

Adsorbent	Adsorbate	Maximum adsorption capacity (mg/g) and/or adsorption efficiency (%)	References
CNTs **and acidified CNTs**	Pb^{2+}	15.6 mg/g 17.5 mg/g and 87,8%	(Li *et al*., 2002)
MWCNTs	Pb^{2+}	97,08 mg/g	(Li *et al*., 2003)
Fe_3O_4-CNTs	Pb^{2+}	0.51 mmol/g	(Peng *et al*., 2005)
CNTs	Pb^{2+}	90,597 mg/g	(Rahbari and Goharrizi, 2009)
CNTs	Pb^{2+}	102 mg/g and 96,03%	(Kabbashi *et al*., 2009)
N-CNTs	Pb^{2+}	6.74 mmol/g	(Shin *et al*., 2011)
Fe_3O_4 nanoparticles	Pb^{2+}	83 mg/g	(Recillas *et al*., 2011)
Fe_3O_4/MWCNTs **Water-soluble Fe_3O_4 NPs**	Pb^{2+} Pb^{2+}	31 mg/g 96,8 mg/g	(Hu *et al*., 2011) (Wang *et al*., 2012)
Fe_3O_4 NPs	Pb^{2+}	73,0 mg/g	(Mahdavi *et al*., 2012)
Fe_3O_4/CNTs	Pb^{2+}	65,40 mg/g	(Zhang *et al*., 2012)
Fe_3O_4/MWCNTs	Pb^{2+}	13.04 mg/g	(Ji *et al*., 2012)

Fe_3O_4 nanoparticles	Pb^{2+}	83.3 mg/g	(Beyki and Shemirani, 2015)
MWCNTs	Pb^{2+}	97,55%	(Moosa *et al*., 2016)
Fe_3O_4 NPs	Pb^{2+}	100%	(Mahmoud and Abdalkareem, 2017)
Acidified functionalized CNTs	Pb^{2+}	93% and 68%	(Farghali *et al*., 2017)
Nitrogen-functionalized MWCNT	Pb^{2+}	36.23 ng/g	(Oyetade *et al*., 2017)
Fe_3O_4 NPs	Pb^{2+}	93±0.13%	Das and Rebecca, 2018
MWCNTS	Pb^{2+}	333.3 mg/g	(Abdel Salam *et al*., 2020)

Based on the studied literature a few studies have emanated on the use of nitrogen doped carbon nanotubes as adsorbents for heavy metals. However, according to our knowledge there was no study where magnetic iron oxide nanoparticles were attached to nitrogen doped CNTs and used as adsorbents for heavy metals. The loading of magnetic iron oxide nanoparticles will aid in recovery of the materials after adsorption. Also the addition of chlorine in the material will aid in creation greater defects onto the walls of the NCNTs based on previous studies by Maboya *et al*., (2019) which will better enable attachment of iron oxide nanoparticles.

2.7. Water Treatment

2.7.1. Adsorption

Adsorption is the preferred wastewater treatment method, although there are several conventional technologies that are utilized in the water treatment field for eliminating heavy metals as listed in Table 2.3. Thus, it can be said that adsorption is a powerful technique among its counterparts, as a result of its effectiveness and simplicity for a wide range of adsorbents.

Table 2.3: The conventional water treatment technologies, adapted without modification from Volesky, (2001).

Method	Disadvantages	Advantages
Chemical precipitation and filtration	for higher concentrations difficult separation NOT effective	simple cheap

	resulting sludges	
Chemical oxidation or reduction	chemicals required (not universal) biological system (slow rates) climate sensitive	mineralisation mineralisation
Electrochemical treatment	for high concentrations EXPENSIVE	metal recovery
Reserve osmosis	high pressures membrane scaling EXPENSIVE	pure effluent (for recycle)
Ion exchange	sensitive to particles EXPENSIVE RESINS	effective pure effluent metal recovery possible
Adsorption	not for metals	conventional sorbents (carbon)
Evaporation	energy intensive EXPENSIVE resulting sludges	pure effluent (for recycle)

2.7.1.1. Adsorption of Pb

Adsorption is based on the surface phenomenon that is categorised by the amount of the adsorbate in the solution th

at is attached onto the surface pores of the adsorbent due to the Van der Waal forces within the molecules (Chiou, 2003). This process takes place as a result of the presence of less soluble water pollutants in which the pollutant(s) has a larger affinity for carbon than the waste (Gawande *et al*., 2017). The process depends on the molecular structure and solubility of the solute which predicts the adsorption capacity. Furthermore, it involves three stages as described by McKay *et al*., (1985), which are; (i) the transfer of mass of the adsorbate (e.g., Pb) from the bulk solution to the exterior of the particle, (ii) the adsorption of the adsorbate onto the active sites, and (iii) the internal diffusion of the adsorbate that can either be through the pore diffusion model or homogeneous solid diffusion model.

There is a need for the interaction of adsorbent and adsorbate in which the adsorbent is the solid material with pores (surface), where adsorption is taking place. The rate and capacity of adsorption is dependent on the physiochemical nature of the adsorbent since the phenomena is based on the surface of the adsorbent. The surface of the adsorbent can be affected by the surface functional groups. The characteristics of an ideal adsorbent to be used in wastewater treatment must be environmentally friendly such as the possession of huge internal surface

area, high sorption capacity, high selectivity for low concentration pollutants, easy detachment from the adsorbate and reusability (Bhavani and Sujatha, 2014). While the adsorbate is the molecule that is adsorbed onto the pores (surface), it must have a stronger solute-solvent interaction. The extent of adsorption is inversely proportional in which the attraction of adsorbate to nanomaterial must increase as described by Landelius rule (Bhavani and Sujatha, 2014). Adsorption can be categorized into two forms namely; physical and chemical, depending on the nature of forces within the two molecules (i.e. adsorbent and adsorbate). Physical adsorption is a phenomenon that is based on weak Van der Waal forces, wherein the gas molecules are adsorbed onto the surface of the solid material. Moreover, there are a number of chemical and physical absorption characteristics as described in Figures 2.14 and 2.15: Chemical adsorption is categorized by the chemical bonds among the gas molecules and the surface of the adsorbent.

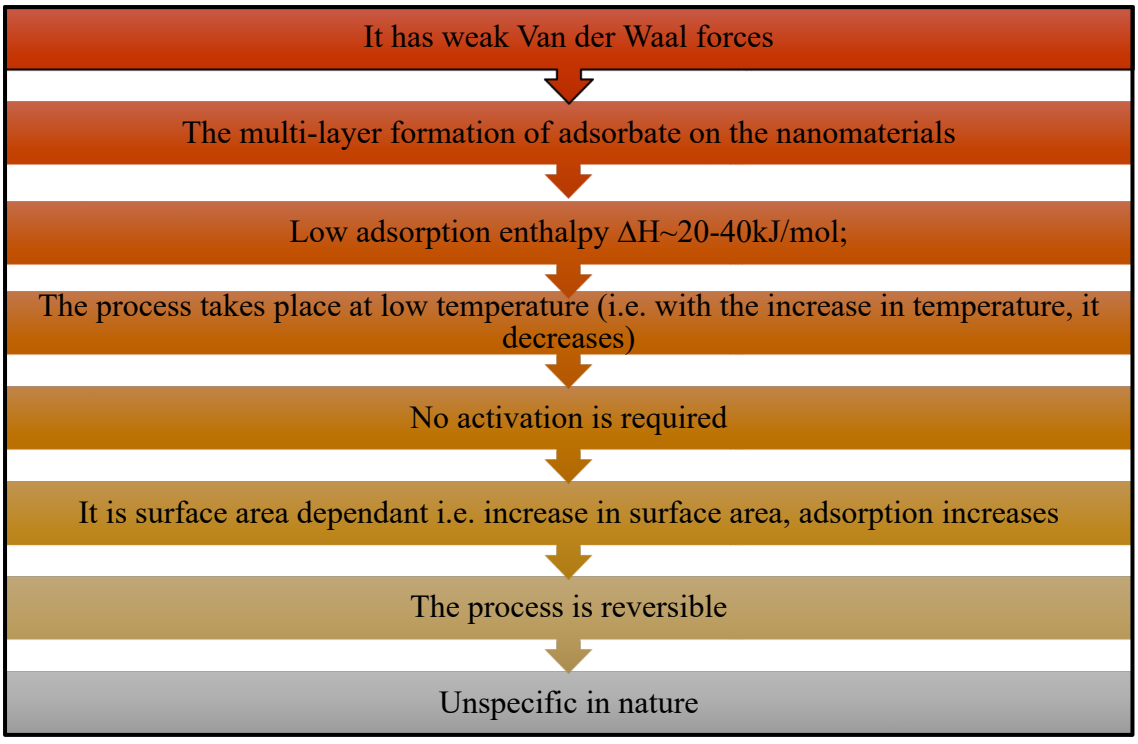

Figure 2.14: Characteristics of physical adsorption process.

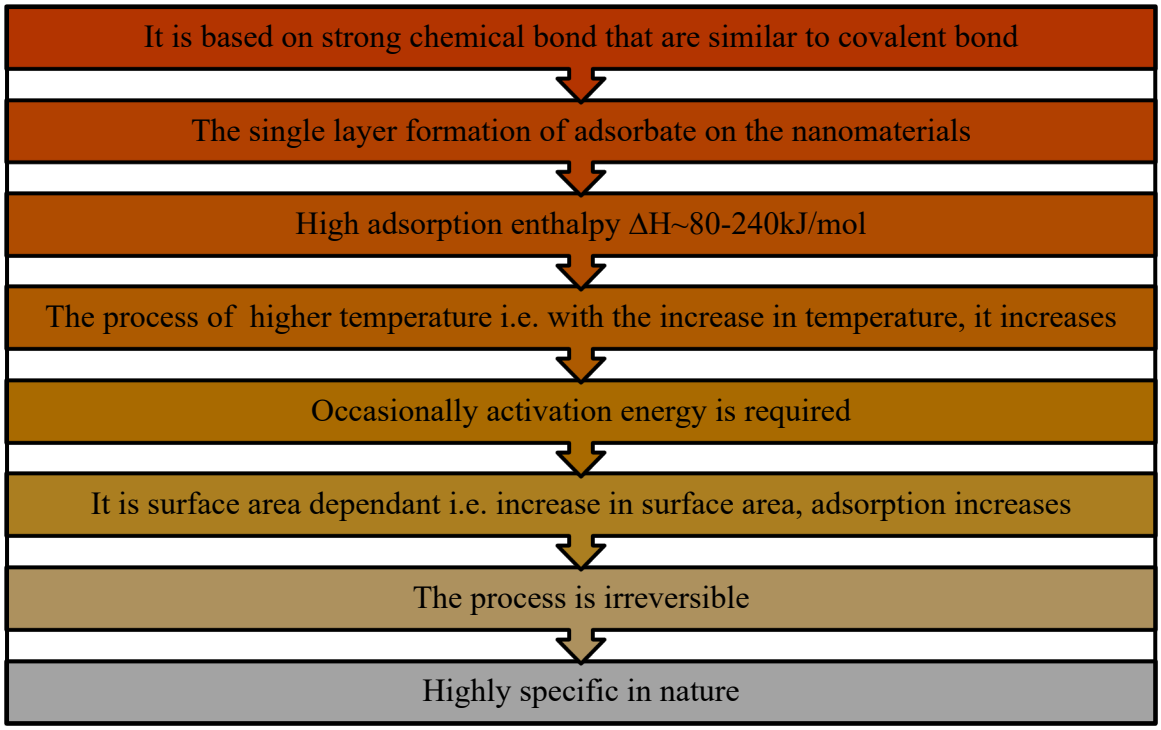

Figure 2.15: Characteristics of chemical adsorption process.

2.7.1.2. Factors affecting adsorption of adsorbate

The adsorption of metal ions from aqueous solutions by adsorbents is strongly dependent on the adsorption parameters namely; (i) the pH of the solution, (ii) the mass of the adsorbent, (iii) the reaction time and (iv) the initial concentration of the analyte.

2.7.1.2.1. Effect of pH (solution)

pH is imperative with regard to the adsorption of metal ions on the surface of the CNTs. It affects the adsorption process as OH^- and H^+ ions have an interaction with the adsorbents. At a pH (solution) higher than that of pH_{pzc} (i.e. point of zero charge), it results in electrostatic interactions due to negative surface that is a favourable condition in absorbing cation ions (Gadhave and Waghmare 2014). The decrease in pH results in the neutralization of the charge, wherein the adsorption cation ions decreases (Gadhave and Waghmare, 2014).

2.7.1.2.2. Effect of adsorbent mass

It is well known, that the increase in the amount of the adsorbate increases the adsorption capacity due to the increase in the number of adsorption sites. However, there are instances where the aforementioned statement does not take place. This is as a result of the increase in the amount of adsorbent that leads to the decrease in the weight of the adsorbent, due to the

interferences created by interaction of the active adsorbent (Das and Das, 2013). Adsorbent mass is used to determine the adsorption capacity of an adsorbent at a specified initial concentration of the adsorbate.

2.7.1.2.3. Effect of initial concentration

At lower concentrations it is known that ions of the adsorbate can interact with the active sites of the adsorbent's surface easily. At higher concentrations there will be less adsorption due to more adsorbate ions that will be competing for the limited active site available on the adsorbent leading to saturation.

2.7.1.2.4. Effect of time

At an initial stage, more vacant spaces are available on the surface of the adsorbent, thus adsorption is taking place faster. However, at a later stage it will be slow due to repulsive forces between the solid and liquid phase. Thus, the longer an adsorbate is exposed to the adsorbent, the more the adsorption will be complete.

2.8. Modelling of adsorption data

The modelling of the adsorption data gives an understanding about the chemical and physical interactions between adsorbent and adsorbate. The information includes the mechanism and the nature of the adsorption process, based on the isotherm and kinetic reactions using their mathematical equations.

2.8.1. Kinetics studies

They are used to ascertain the adsorption uptake in relation to time at constant pressure or concentration and it is also utilized to ascertain the diffusion of adsorbate in the pores (Saha and Grappe, 2017). The three common kinetics models are the pseudo-first-order, pseudo-second-order, and intraparticle diffusion. The Lagergren pseudo-first order model proposes that the rate of sorption is proportional to the number of sites unoccupied by the adsorbate (Ho, 2004). The pseudo-first order equation can be written in the linearized form as shown in Equation 2.1.

$$log(q_e - q_t) = \frac{k_1}{2{,}303}\, t + log\,(q_e) \qquad 2.1$$

where q_t is the adorption capacity (mg/g) at any present time interval (t), q_e is the adsorption capacity at equilibrium and k_1 is the pseudo-first order rate constant (min^{-1}). A graph of log ($q_e - q_t$) versus time is usually plotted and the constant is found. Additionally, the adsorption data can be analysed using the pseudo-second order kinetic model (Ho and Mckay, 1999). The pseudo-second order kinetic model can be written in a linearized form as indicated in Equation 2.2.

$$\frac{t}{q_t} = \left(\frac{1}{q_e}\right) t + \left(\frac{1}{k_2 q_e^2}\right) \qquad \textbf{2.2}$$

where q_t is the adorption capacity (mg/g) at any present time interval (t), q_e is the adsorption capacity at equilibrium and k_2 is the second-order rate constant (g/mg min). The plot of t/q_t versus time (a straight lines) can be achieved and the constants, k_2 and q_e can then be determined thereafter. Intraparticle diffusion are done to have a better understanding of the mechanism and rate-controlling step that affect the kinetics of adsorption, the results experiments can be fitted to the Weber-Morris intraparticle diffusion (IPD) model which is commonly expressed by the equation (Weber and Morris, 1963):

$$q_t = k_p \sqrt{t} + C \qquad \textbf{2.3}$$

where kp is the intraparticle diffusion rate constant (mg/g x $min^{1/2}$), C is the intercept (mg/g).

2.8.2. Adsorption isotherms

Adsorption isotherms are purposively utilised in relation to the concentration of the surfactant in the bulk and the amount adsorbed at the interface (Eastoe and Dalton, 2000). The two common isotherm models are the Langmuir and Freundlich models. The Langmuir isotherm is projected to describe gas-solid phase, which assumes a monolayer on a uniform surface with same affinity and has no lateral interaction. In this case, the adsorbed molecules are localized and can be described by Equation 2.4 (Ayawei *et* al., 2017).

$$\frac{C_e}{q_e} = \left(\frac{1}{Q^o_{max}}\right) C_e + \frac{1}{Q^o_{max} K_L} \qquad \textbf{2.4}$$

where, C_e is the concentration of adsorbate at equilibrium (mg/g), q_e is the quantity or maximum of adsorption capacity (mg/g), q_m is the amount adsorbed (mg/g). K_L is the Langmuir

constant related to the energy of the adsorption. Moreover, it can also be expressed on the basis of dimensional equilibrium parameter R_L given by Equation 2.5:

$$\boldsymbol{R_L = \frac{1}{1+ K_L\, C_o}} \qquad \textbf{2.5}$$

where, K_L is the Langmuir constant (mg/g), C_o is the initial concentration of initial adsorbate (mg/g), R_l lies within 0 and 1 when adsorption is favourable (i.e. when R_L >1 (unfavourable), R_L =1 (linear), R_L =0 (irreversible) and α R_L<1 (favourable)). The Freundlich isotherm estimate the sorption intensity of adsorbent toward adsorbate, it takes place on heterogeneous surface and applies to multilayer and monolayer which can be described by Equation 2.6 (Ayawei *et al*., 2017).

$$\boldsymbol{log\, q_e = n\, log\, C_e + log\, K_f} \qquad \textbf{2.6}$$

where, K_f is the constant adsorption capacity (L/mg), q_e is theconcentration at equilibrium (mg/L), C_e is equilibrium concentration (mg/L), and 1/n is the constant adsorption intensity.

References

Abbas, A., Abussaud, B.A., Ihsanullah, Al-Baghli, N.A.H., Khraisheh, M., and Atieh, M.A., 2016. Benzene removal by iron oxide nanoparticles decorated carbon nanotubes. *Journal of Nanomaterials*, 2016, 1–10.

Abdel Salam, E.T., Abou El-Nour, K.M., Awad, A.A., and Orabi, A.S., 2020. Carbon nanotubes modified with 5,7-dinitro-8-quinolinol as potentially applicable tool for efficient removal of industrial wastewater pollutants. *Arabian Journal of Chemistry*, 13 (1), 109–119.

Ajayan, P.M., 1999. Nanotubes from Carbon. Chemical Reviews, 99 (7), 1787–1799.

Aqel, A., El-Nour, K.M.M.A., Ammar, R.A.A., and Al-Warthan, A., 2012. Carbon nanotubes, science and technology part (I) structure, synthesis and characterisation. *Arabian Journal of Chemistry*, 5 (1), 1–23.

Ayala, P., Arenal, R., Rümmeli, M., Rubio, A., and Pichler, T., 2010. The doping of carbon nanotubes with nitrogen and their potential applications. *Carbon*, 48 (3), 575–586.

Ayawei, N., Ebelegi, A.N., and Wankasi, D., 2017. Modelling and interpretation of adsorption isotherms. *Journal of Chemistry*, 2017, 1–11.

Bailey, S.., Olin, T.., Bricka, R.., and Adrian, D.., 1999. A review of potentially low-cost sorbents for heavy metals. *Water Research*, 33 (11), 2466–2479.

Barthos, R., Bakather, O.Y., Kayvani Fard, A., Ihsanullah, Khraisheh, M., Nasser, M.S., and Atieh, M.A., 2005. Functionalization of single-walled carbon nanotubes by using alkyl-halides. *Carbon*, 43 (2), 321–325.

Beyki, M.H. and Shemirani, F., 2015. Dual application of facilely synthesized Fe_3O_4 nanoparticles: fast reduction of nitro compound and preparation of magnetic polyphenylthiourea nanocomposite for efficient adsorption of lead ions. *RSC Advances*, 5 (28), 22224–22233.

Bhavani, P. and Sujatha, B., 2014. Adsorption of chromium (VI) on biomaterial. *Journal of Chemical and Pharmaceutical Sciences JCHPS Special Issue*, 3, 974–2115.

Blaney, L., 2007. Magnetite (Fe_3O_4): Properties, synthesis, and applications, 15–2007, 33–81.

Boldyrev, M., 2018. Lead: properties, history, and applications. *WikiJournal of Science*, 1 (2), 7.

Cerro-Lopez, M. and Méndez-Rojas, M.A., 2019. Application of nanomaterials for treatment of wastewater containing pharmaceuticals. *Handbook of Environmental Chemistry*, 66, 201–219.

Chaki, S.H., Malek, T.J., Chaudhary, M.D., Tailor, J.P., and Deshpande, M.P., 2015. Magnetite

Fe_3O_4 nanoparticles synthesis by wet chemical reduction and their characterization. *Advances in Natural Sciences: Nanoscience and Nanotechnology*, 6 (3).

Chawla, J., Kumar, R., and Kaur, I., 2015. Carbon nanotubes and graphenes as adsorbents for adsorption of lead ions from water: A review. *Journal of Water Supply: Research and Technology - AQUA*, 64 (6), 641–659.

Chen, D. and Meng, Y., 2017. Synthesis of magnetic oxide nanoparticles for biomedical applications. *Global Journal of Nanomedicine*, 2 (3), 1–4.

Chiou, C.T., 2003. Fundamentals of the adsorption theory. *In: Partition and Adsorption of Organic Contaminants in Environmental Systems*. John Wiley & Sons, Inc., 39–52.

Cho, H.H., Wepasnick, K., Smith, B.A., Bangash, F.K., Fairbrother, D.H., and Ball, W.P., 2010. Sorption of aqueous Zn[II] and Cd[II] by multiwall carbon nanotubes: The relative roles of oxygen-containing functional groups and graphenic carbon. *Langmuir*, 26 (2), 967–981.

Cornell, R.M. and Schwertmann, U., 2003. *The Iron Oxides: Structure, Properties, Reactions, Occurrences and Uses*. Second. Wiley-VCH.

Dadfar, S.M., Roemhild, K., Drude, N.I., von Stillfried, S., Knüchel, R., Kiessling, F., and Lammers, T., 2019. Iron oxide nanoparticles: Diagnostic, therapeutic and theranostic applications. *Advanced Drug Delivery Reviews*, 138, 302–325.

Das, N. and Das, D., 2013. Recovery of rare earth metals through biosorption: An overview. *Journal of Rare Earths*, 31 (10), 933–943.

Das, M.P. and Rebecca, L.J., 2018. Removal of lead(II) by phyto-inspired iron oxide nanoparticles. *Nature Environment and Pollution Technology*, 17 (2), 569–574.

Dave, P.N. and Chopda, L. V., 2014. Application of iron oxide nanomaterials for the removal of heavy metals. *Journal of Nanotechnology*, 2014, 1–14.

defenceWeb, 2019. Ekurhuleni Water Care Company helping SANDF fix Vaal water crisis - defenceWeb [online]. Available from: https://www.defenceweb.co.za/featured/ekurhuleni-water-care-company-helping-sandf-fix-vaal-water-crisis/ [Accessed 22 Oct 2019].

Dervishi, E., Li, Z., Xu, Y., Saini, V., Biris, A.R., Lupu, D., and Biris, A.S., 2009. Carbon nanotubes: Synthesis, properties, and applications. *Particulate Science and Technology*, 27 (2), 107–125.

Dong, C.-K., Li, X., Zhang, Y., Qi, J.-Y., and Yuan, Y.-F., 2009. Fe_3O_4 nanoparticles decorated multi-walled carbon nanotubes and their sorption properties. *Chemical Research in. Chinese Universities*, 25 (6), 936–940.

DWF, 1996. *South African Water Quality Guidelines Volume 1 Domestic Use Department of Water Affairs and Forestry Second edition 1996*.

Eastoe, J. and Dalton, J.S., 2000. Dynamic surface tension and adsorption mechanisms of surfactants at the airwater interface, 85 (2000), 103–144.

Eatemadi, A., Daraee, H., Karimkhanloo, H., Kouhi, M., Zarghami, N., Akbarzadeh, A., Abasi, M., Hanifehpour, Y., and Joo, S., 2014. Carbon nanotubes: properties, synthesis, purification, and medical applications. *Nanoscale Research Letters*, 9 (1), 393.

Eberhard, R., 2018. Cape is no exception_ water crisis risks are systemic and affect all of SA [online]. Available from: https://www.businesslive.co.za/bd/opinion/2018-09-11-cape-is-no-exception-water-crisis-risks-are-systemic-and-affect-all-of-sa/ [Accessed 22 Feb 2020].

Ewels, C.P. and Glerup, M., 2005. Nitrogen doping in carbon nanotubes. *Journal of Nanoscience and Nanotechnology*.

Farghali, A.A., Abdel Tawab, H.A., Abdel Moaty, S.A., and Khaled, R., 2017. Functionalization of acidified multi-walled carbon nanotubes for removal of heavy metals in aqueous solutions. *Journal of Nanostructure in Chemistry*, 7 (2), 101–111.

Farghali, A.A., Bahgat, M., El Rouby, W.M.A., and Khedr, M.H., 2012. Decoration of MWCNTs with $CoFe_2O_4$ nanoparticles for methylene blue dye adsorption. *Journal of Solution Chemistry*, 41 (12), 2209–2225.

Farid, G., 2016. Heavy Metals (Cd, Ni and Pb) Contamination of soils, plants and waters in madina town of faisalabad metropolitan and preparation of gis based maps. *Advances in Crop Science and Technology*, 04 (01), 1–7.

Fernández-Luqueño, F., López-Valdez, F., Gamero-Melo, P., Luna-Suárez, S., Nadia Aguilera-González, E., Martínez, A.I., del Socorro García-Guillermo, M., Hernández-Martínez, G., Herrera-Mendoza, R., Antonio Álvarez-Garza, M., and Rubí Pérez-Velázquez, I., 2013. Heavy metal pollution in drinking water-a global risk for human health: A review, 7 (7), 567–584.

Gadhave, A. and Waghmare, J., 2014. Removal of heavy metal ions from wastewater by carbon nanotubes (CNTs) 1. *International Journal of Chemical Sciences and Applications*, 5 (2), 56–67.

Gawande, S.M., Belwalkar, N.S., and Mane, A.A., 2017. Adsorption and its isotherm – theory. *International Journal of Engineering Research*, 6 (6), 312.

Global lead output set to bounce back in 2019 [online], 2019. Available from: https://www.mining-technology.com/comment/lead-output-in-2019/ [Accessed 23 Oct

2019].

Golnabi, H., 2012. Carbon nanotube research developments in terms of published papers and patents, synthesis and production. *Scientia Iranica*, 19 (6), 2012–2022.

Gupta, N., Gupta, S.M., and Sharma, S.K., 2019. Carbon nanotubes: Synthesis, properties and engineering applications. *Carbon Letters*, 29 (5), 419–447.

Gupta, V.K., Agarwal, S., and Saleh, T.A., 2011. Synthesis and characterization of alumina-coated carbon nanotubes and their application for lead removal. *Journal of Hazardous Materials*, 185 (1), 17–23.

Herrera-Herrera, A. V., González-Curbelo, M. ángel, Hernández-Borges, J., and Rodríguez-Delgado, M. ángel, 2012. Carbon nanotubes applications in separation science: A review. *Analytica Chimica Acta*, 734, 1–30.

Ho, Y.S., 2004. Citation Review of lagergren kinetic rate equation on adsorption reactions. *Scientometrics*, 59 (1), 171–177.

Ho, Y.S. and Mckay, G., 1999. Pseudo-second order model for sorption.pdf, 34, 451–465.

Hu, J., Zhao, D., and Wang, X., 2011. Removal of Pb(II) and Cu(II) from aqueous solution using multiwalled carbon nanotubes/iron oxide magnetic composites. *Water Science and Technology*, 63 (5), 917–923.

Igwe, J., 2007. A review of potentially low cost sorbents for heavy metal removal and recovery. *Terrestrial and Aquatic Environmental Toxicology*, 1 (2), 60–69.

Iijima, S., 1991. Helical microtubules of graphhitic carbon. *Nature*, 354, 56–58.

Iijima, S.; Ichihashi, T. Single-shell carbon nanotubes of 1-nm diameter. *Nature* 1993, *363*, 603– 605.

ILA, 2012. Lead production & statistics < Lead facts | ILA - International Lead Association Website [online]. Available from: https://www.ila-lead.org/lead-facts/lead-uses--statistics [Accessed 27 Feb 2020].

Ji, L., Zhou, L., Bai, X., Shao, Y., Zhao, G., Qu, Y., Wang, C., and Li, Y., 2012. Facile synthesis of multiwall carbon nanotubes/iron oxides for removal of tetrabromobisphenol A and Pb(II). *Journal of Materials Chemistry*, 22 (31), 15853.

Kabbashi, N.A., Atieh, M.A., Al-Mamun, A., Mirghami, M.E., Alam, M.D.Z., and Yahya, N., 2009. Kinetic adsorption of application of carbon nanotubes for Pb(II) removal from aqueous solution. *Journal of Environmental Sciences*, 21 (4), 539–544.

Kónya, Z., Vesselenyi, I., Niesz, K., Kukovecz, A., Demortier, A., Fonseca, A., Delhalle, J., Mekhalif, Z., Nagy, J.B., Koós, A.A., Osváth, Z., Kocsonya, A., Biró, L.P., and Kiricsi, I., 2002. Large scale production of short functionalized carbon nanotubes. *Chemical*

Physics Letters, 360 (5–6), 429–435.

Kroto, H.W., Heath, J.R., O'Brieb, S.C., Curl, R.F., and Smalley, R.E., 1985. C60: Buckminsterfullerene. *Letters to Nature*, 318, 162–163.

Lead producer countries and their percentage in world production [online], 2009. Available from:http://www.yourarticlelibrary.com/essay/lead-producer-countries-and-their-percentage-in-world-production/25474 (Accessed 26 Feb 2020).

Li, Y.-H., Ding, J., Luan, Z., Di, Z., Zhu, Y., Xu, C., Wu, D., and Wei, B., 2003. Competitive adsorption of Pb^{2+}, Cu^{2+} and Cd^{2+} ions from aqueous solutions by multiwalled carbon nanotubes. *Carbon*, 41 (14), 2787–2792.

Li, Y.-H., Wang, S., Wei, J., Zhang, X., Xu, C., Luan, Z., Wu, D., and Wei, B., 2002. Lead adsorption on carbon nanotubes. *Chemical Physics Letters*, (357), 263–266.

Lin, D. and Xing, B., 2008. Adsorption of phenolic compounds by carbon nanotubes: Role of aromaticity and substitution of hydroxyl groups. *Environmental Science and Technology*, 42 (19), 7254–7259.

Lingamdinne, L.P., Koduru, J.R., and Karri, R.R., 2019. A comprehensive review of applications of magnetic graphene oxide based nanocomposites for sustainable water purification. *Journal of Environmental Management*, 231 (July 2018), 622–634.

Liu, X., Wang, M., Zhang, S., and Pan, B., 2013. Application potential of carbon nanotubes in water treatment: A review. *Journal of Environmental Sciences*, 25 (7), 1263–1280.

Lu, H., Wang, J., Stoller, M., Wang, T., Bao, Y., and Hao, H., 2016. An overview of nanomaterials for water and wastewater treatment. *Advances in Materials Science and Engineering*, 2016, 1–10.

Lu, Z., Raad, R., Safaei, F., Xi, J., Liu, Z., and Foroughi, J., 2019. Carbon nanotube based fiber supercapacitor as wearable energy storage. *Frontiers in Materials*, 6 (June), 1–14.

Maboya, W.K., Coville, N.J., and Mhlanga, S.D., 2016. The synthesis of carbon nanomaterials using chlorinated hydrocarbons over a Fe-Co/$CaCO_3$ catalyst. *South African Journal of Chemistry*, 69, 15–26.

Mahdavi, S., Jalali, M., and Afkhami, A., 2012. Removal of heavy metals from aqueous solutions using Fe_3O_4, ZnO, and CuO nanoparticles. *Journal of Nanoparticle Research*, 14 (8), 846.

Mahmoud, Z.H. and Abdalkareem, A.A., 2017. Removal of Pb^{2+} ions from water by magnetic iron oxide nanoparticles that prepared via ECD, (June).

Mallakpour, S. and Khadem, E., 2016. Carbon nanotube–metal oxide nanocomposites: Fabrication, properties and applications. *Chemical Engineering Journal,* 302, 344–367.

Mazrouaa, A.M.., Mohamed, M.G.., and Fekry, M., 2019. Physical and magnetic properties of iron oxide nanoparticles with a different molar ratio of ferrous and ferric. *Egyptian Journal of Petroleum*, 28 (2), 165–171.

McKay, G., Otterburn, M.S., and Aga, J.A., 1985. Fuller's earth and fired clay as absorbents for dyestuffs external mass transport processes during adsorption. *Water, Air, and Soil Pollution*, 26, 149–161.

Mehra, N., Pharma, S., and Jain, N.K., 2014. Functionalized Carbon Nanotubes and Their Drug Delivery Applications. *Nanostructured Drug Delivery*, 4 (June), 328–369.

Meyyappan, M., 2005. *Carbon nanotubes: Science and applications.* CRC Press.

Mihalchik, A.L., Ding, W., Porter, D.W., McLoughlin, C., Schwegler-Berry, D., Sisler, J.D., Stefaniak, A.B., Snyder-Talkington, B.N., Cruz-Silva, R., Terrones, M., Tsuruoka, S., Endo, M., Castranova, V., and Qian, Y., 2015. Effects of nitrogen-doped multi-walled carbon nanotubes compared to pristine multi-walled carbon nanotubes on human small airway epithelial cells. *Toxicology*, 333, 25–36.

Moosa, A.A., Ridha, A.M., and Hussien, N.A., 2016. Adsorption, heavy metals, isotherm, bioadsorption, carbon nanotube; adsorption, heavy metals, isotherm, bioadsorption, carbon nanotube. *American Journal of Materials Science*, 6 (5), 115–124.

Morita, M., Rau, D., Kajiyama, S., Sakurai, T., Baba, M., and Iwamura, M., 2004. 'Luminescence properties of nano-phosphors: metal-ion doped sol-gel silica glasses'. *Materials Science-Poland*, 22 (1), 5–15.

Navaei Diva, T., Zare, K., Taleshi, F., and Yousefi, M., 2017. Synthesis, characterization, and application of nickel oxide/CNT nanocomposites to remove Pb^{2+} from aqueous solution. *Journal of Nanostructure in Chemistry*, 7 (3), 273–281.

Nejati, K. and Zabihi, R., 2012. Preparation and magnetic properties of nano size nickel ferrite particles using hydrothermal method. *Chemistry Central Journal*, 6 (1), 23.

Ntim, S.. and Mitra, S., 2012. NIH Public Access. Removal of trace arsenic to meet drinking water standards using iron oxide coated multiwall carbon nanotubes, 56 (5), 2077–2083.

Osikoya, A.O., Dikio, C.W., Ayawei, N., Wankasi, D., Afolabi, A.S., and Dikio, E.D., 2015. Synthesis, characterization and adsorption studies of chlorine–doped carbon nanotubes. *Advances in Materials Science and Applications*, 4 (2), 53–62.

Oyetade, O.A., Skelton, A.A., Nyamori, V.O., Jonnalagadda, S.B., and Martincigh, B.S., 2017. Experimental and DFT studies on the selective adsorption of Pb^{2+} and Zn^{2+} from aqueous solution by nitrogen-functionalized multiwalled carbon nanotubes. *Separation and Purification Technology*, 188, 174–187.

Panchangam, S.C., 2015. Engineering & science focus: AITK A monthly academic bulletin Article : *Engineering & Science Focus*: *AITK*, (September), 1–4.

Pang, L.S.K., Saxby, J.D., and Chatfield, S.P., 1993. Thermogravimetric analysis of carbon nanotubes and nanoparticles. *The Journal of Physical Chemistry*, 97, 6941–6942.

Pełech, I., Narkiewicz, U., Moszyński, D., and Pełech, R., 2012. Simultaneous purification and functionalization of carbon nanotubes using chlorination. *Journal of Materials Research*, 27 (18), 2368–2374.

Pełech, I., Pełech, R., Narkiewicz, U., Moszyński, D., Jędrzejewska, A., and Witkowski, B., 2013. Chlorination of carbon nanotubes obtained on the different metal catalysts. *Journal of Nanomaterials*, 2013, 1–9.

Peng, X., Luan, Z., Di, Z., Zhang, Z., and Zhu, C., 2005. Carbon nanotubes-iron oxides magnetic composites as adsorbent for removal of Pb(II) and Cu(II) from water. *Carbon*, 43 (4), 880–883.

Prasek, J., Drbohlavova, J., Chomoucka, J., Hubalek, J., Jasek, O., Adam, V., and Kizek, R., 2011. Methods for carbon nanotubes synthesis—review. *Journal of Materials Chemistry*, 21 (40), 15872.

Purohit, R., Purohit, K., Rana, S., Rana, R.S., and Patel, V., 2014. Carbon nanotubes and their growth methods. *Procedia Materials Science,* 6, 716–728.

Rahbari, M. and Goharrizi, A.S., 2009. Adsorption of lead(II) from water by carbon nanotubes: equilibrium, kinetics. Source: *Water Environment Research*, 81 (6), 598–607.

Ray, S.C., 2018. Nitrogenated carbon nanotubes functionalized with chlorine and oxygen: Electronic and magnetic properties for electronic/magnetic device applications. *Frontier Research Today*, 1, 1006.

Ray, S.C., Pao, C.W., Tsai, H.M., Chiou, J.W., Pong, W.F., Chen, C.W., Tsai, M.-H., Papakonstantinou, P., Chen, L.C., Chen, K.H., and Graham, W.G., 2007. Electronic structures and bonding properties of chlorine-treated nitrogenated carbon nanotubes: X-ray absorption and scanning photoelectron microscopy studies. *Applied Physics Letters*, 90 (19), 192107.

Recillas, S., García, A., González, E., Casals, E., Puntes, V., Sánchez, A., and Font, X., 2011. Use of CeO_2, TiO_2 and Fe_3O_4 nanoparticles for the removal of lead from water. *Desalination*, 277 (1–3), 213–220.

Reddy, B.P.N., Gupta, B., and Gacche, R.N., 2009. An arsenal for 21st century noxious diseases: carbon nanomaterials. *International Journal of nanotechnology and Applications*, 3 (2), 61–76.

Rosso, M.A., 2001. *Origins, properties, and applications of carbon nanotubes and fullerenes*. California.

Sadegh, H., Shahryari Ghoshekandi, R., Masjedi, A., Mahmoodi, Z., and Kazemi, M., 2016. A review on Carbon nanotubes adsorbents for the removal of pollutants from aqueous solutions. *International Journal of Nano Dimension*, 7 (2), 109–120.

Saha, D. and Grappe, H.A., 2017. Adsorption properties of activated carbon fibers. *In: Activated Carbon Fiber and Textiles*. Elsevier, 143–165.

Sankhla, M.S., Kumari, M., Nandan, M., Kumar, R., and Agrawal, P., 2016. Heavy metals contamination in water and their hazardous effect on human health-A review. *International Journal of Current Microbiology and Applied Sciences*, 5 (10), 759–766.

Santhosh, C., Velmurugan, V., Jacob, G., Jeong, S.K., Grace, A.N., and Bhatnagar, A., 2016. Role of nanomaterials in water treatment applications: A review. *Chemical Engineering Journal*, 306, 1116–1137.

Sharma, A., Gudala, S., Ambati, S.R., Penta, S., Mahapatra, S.P., Vedula, R.R., Pola, S., and Acharya, B., 2017. Synthesis of heterocyclic compounds catalyzed by metal/metal oxide-multiwall carbon nanotube nanocomposites. *Journal of the Chinese Chemical Society*, 64 (6), 589–606.

Shin, K.-Y., Hong, J.-Y., and Jang, J., 2011. Heavy metal ion adsorption behavior in nitrogen-doped magnetic carbon nanoparticles: Isotherms and kinetic study. *Journal of Hazardous Materials*, 190 (1–3), 36–44.

Singh, R.M. and Gupta, A., 2017. Water pollution-sources , effects and control water pollution-sources , effects and control. *Research gate,* 5 (3).

Stephen, O., Ajayan, P.M., Colliex, C., Redlich, P., Lambert, J.M., Bernier, P., Lefin, P., and de Dy-, G., 1994. Doping graphitic and carbon nanotube structures with boron and nitrogen.

Tchounwou, P.B., Yedjou, C.G., Patlolla, A.K., and Sutton, D.J., 2010. *Molecular, Clinical and Environmental Toxicology*. National Institures of Health Public Access. Basel: Birkhäuser Basel.

Teja, A.S. and Koh, P.Y., 2009. Synthesis, properties, and applications of magnetic iron oxide nanoparticles. *Progress in Crystal Growth and Characterization of Materials*, 55 (1–2), 22–45.

Tiwari, S., Tripathi, I.P., and Tiwari, H.L., 2013. Effects of lead on environment. *International Journal of Emerging Research in Management &Technology*, 2 (6), 1–5.

Varshney, K., 2014. Carbon nanotubes: A review on synthesis, properties and applications.

International Journal of Engineering Research and General Science, 2 (4), 660–677.

Volesky, B., 2001. Detoxification of metal-bearing effluents: Biosorption for the next century. *Hydrometallurgy*, 59 (2–3), 203–216.

Wang, L., Li, J., Jiang, Q., and Zhao, L., 2012. Water-soluble Fe_3O_4 nanoparticles with high solubility for removal of heavy-metal ions from waste water. *Dalton Transactions*, 41 (15), 4544.

Weber, W. and Morris, J., 1963. Kinetics of adsorption on carbon from solution. *Journal of the Sanitary Engineering Division*, 89 (2), 31–60.

Wepasnick, K.A., Smith, B.A., Bitter, J.L., and Howard Fairbrother, D., 2010. Chemical and structural characterization of carbon nanotube surfaces. *Analytical and Bioanalytical Chemistry*, 396 (3), 1003–1014.

WHO, 2014. Drinking water and sanitation Progress on. *Unicef*.

WHO, 2015. Lead exposure in African children: Contemporary sources and concern.

World water vision: Its origin and purpose, 2000. Colombo.

Wu, H., Liu, G., Wang, X., Zhang, J., Chen, Y., Shi, J., Yang, H., Hu, H., and Yang, S., 2011. Solvothermal synthesis of cobalt ferrite nanoparticles loaded on multiwalled carbon nanotubes for magnetic resonance imaging and drug delivery. *Acta Biomaterialia*, 7 (9), 3496–3504.

Yu, M.-F., Lourie, O., Dyer, M.J., Moloni, K., Kelly, T.F., and Ruoff, R.S., 2000. *Strength and breaking mechanism of multiwalled carbon nanotubes under tensile load*.

Yuan, J.M., Chen, X.H., Chen, X.H., Fan, Z.F., Yang, X.G., and Chen, Z.H., 2008. An easy method for purifying multi-walled carbon nanotubes by chlorine oxidation. *Carbon*, 46 (9), 1266–1269.

Zhang, C., Sui, J., Li, J., Tang, Y., and Cai, W., 2012. Efficient removal of heavy metal ions by thiol-functionalized superparamagnetic carbon nanotubes. *Chemical Engineering Journal*, 210, 45–52.

Zhang, Y., Wu, B., Xu, H., Liu, H., Wang, M., He, Y., and Pan, B., 2016. Nanomaterials-enabled water and wastewater treatment. *NanoImpact*, 3–4, 22–39.

Ziervogel, G., Franklin, B., and Thorson, J., 2019. *Unpacking the cape town drought:Lessons learned report for cities support programme undertaken by african centre for cities*.

CHAPTER 3

Technical instruments used to characterize nanomaterials

3. Brief introduction

This chapter gives a description of the characterization techniques utilized in this research project. Various analytical/technical instruments were employed to analyse the nanomaterials fabricated in this study. The carbon nanomaterials (CNMs) were characterised using various analytical instruments such as powder X-ray diffraction (PXRD), scanning electron microscopy (SEM), transmission electron microscopy (TEM), thermal gravimetric analysis (TGA), X-ray photoelectron spectroscopy (XPS), Raman spectroscopy, Brunauer-Emmett-Teller analysis (BET), and atomic absorption spectroscopy (AAS).

3.1. Powder X-ray diffraction spectroscopy

PXRD is a simple, rapid technique, with minimal sample preparation and it is a non-destructive technique that is primarily utilized for phase identification of solid sample. This technique is ideal for both organic and inorganic materials. It basically generates information on a unit cell dimensions. The information such as structures, preferred crystal orientations such as texture, phases and other structural parameters namely an average grain size, crystal defects and strains, crystallinity and thermal expansion can be determined using this technique. This method is from the X-ray crystallography family, that is founded on constructive interference of monochromatic X-rays and a crystalline sample (Bunaciu *et al*., 2015). The X-rays are created by a cathode tube, filtered to produce monochromatic radiation which is then collimated to concentrate and then focused to the sample, when there is contact between the X-rays and the sample. Thereafter, this result in constructive interferences (by diffracted rays) being produced. The constructive interferences that satisfy Bragg's Law are therefore sent to the detector in which the diffracted ray is processed and counted. As a result, the diffraction pattern of the sample is obtained. Thus, the diffraction pattern is described by Bragg's equation given below (Chatterjee, 2012).

$$n\lambda = 2dsin\theta \qquad 3.1$$

where n is an integer, λ is the wavelength of the X-ray, θ is the angle of the incident and diffraction ray, d is the spacing between the atomic planes. This equation describes the interferences pattern of the X-rays scattered by the crystals and it also demonstrates the relation of wavelength (i.e. electromagnetic radiation to the diffraction angle and the lattice spacing in a crystal pair). The d-spacings are distinctive for each compound and for this reason, the diffraction peaks are converted to d-spacings for various crystals identification. Thus, these d-spacings can always be matched to the reference pattern. The data can be recorded at 2θ from 5° to 90° for every sample. The typical interspacing of a crystal is approximately 2 to 3 Å which allows the use of X-ray as the appropriate radiation in the study of the crystal structure. For the electromagnetic radiation to be diffracted, the spacing in the grating should be of the same order as the wavelength. However, this technique has drawbacks about mixed materials with a limit of detection of approximately 2% for every sample. There is complexity in indexing pattern of non-isomeric crystal systems in a unit cell mostly for overlapping peaks. The use of this technique is not only limited to analysis of carbon materials but also materials such as polymers, and metal catalyst.

Figure 3.1: Bruker D2 Phaser PXRD.

Figure 3.1 depicts the PXRD spectroscopy that was employed in analysing all the prepared samples (i.e., finely ground and homogenized) in this study. It utilizes Cu-Kα irradiation and

with a 30 kV X-ray tube that has a current of 30 mA at a range of $10° \leq 2\theta \leq 70°$. The Bragg-Brentano has an incident angle within the X-ray source and the sample with the 2θ of the diffraction angle being within the detector and the incident beam. The analysis requires minimal sample preparation. The sample is usually transferred onto the sample holder, then flattened with a flat glass slide with minimal pressure applied to achieve a smooth-flat surface uniform distribution of sample and height. The scans can be measured over a period of an hour and the data of spectrum is reported as a pattern of peak(s) intensity as the function of 2θ. Therefore, the resulted peak(s) or patterns at their position along the 2θ range can be identified through peak searching where the respective phases were matched using the EVA software.

3.2. Electron microscopy

Electron microscopy is commonly used in the field of science which uses a beam of electrons and electromagnetic lenses to form an image of a specimen (Bozzola, 2001). It typically utilises electron-optical systems that have lenses such as an electromagnetic and an electrostatic lenses which work in high vacuum systems (Udochukwu, 2005). Their operation under high vacuum enables the electron beam to travel in a straight line. The common electron microscopy includes scanning electron microscopy (SEM) and transmission electron microscopy (TEM) which gives 3D and 2D images respectively. These microscopies can be coupled with energy dispersive spectroscopy (EDS).

3.2.1. Scanning electron microscopy

SEM is based on a beam of energetic electron scanning fine exterior of different materials through imaging at various resolution. It can also the give information on elemental chemical composition of most samples depending on the sample nature. The electron beam is focused on the surface of the material where it generates several types of signals and are generated as a function of a position of the surface from the different types of signals. These signals give different information such as secondary electron, structure of the surface, backscattered electrons, average elemental information and also structural information, X-rays and Auger electrons, elemental composition with various thickness sensitivity. Thus, the specimen's information such as composition, surface topography, and morphology can be obtained. The electron beam in the gun is generated by the current that heat the tungsten wire. This electron beam is accelerated by the anode, then travels through the electromagnetic fields and lenses; wherein the beam is focused down towards the specimen. The deflection coils mechanism

navigates the beam to the direction of the specimen, to scan the surface in a rectangular frame. The interaction between the surface of specimen and beam can result in secondary electrons beam or backscattered electrons. The secondary electrons that are emitted, are directed to the detector, which converts it into a signal that is sent to a screen creating the final image. Therefore, the additional detectors collect the backscattered electron and create the corresponding images. The surface topography and the material has an effect on the electron in relation to the intensity as well as the angle of the emission (Mattox, 2010).

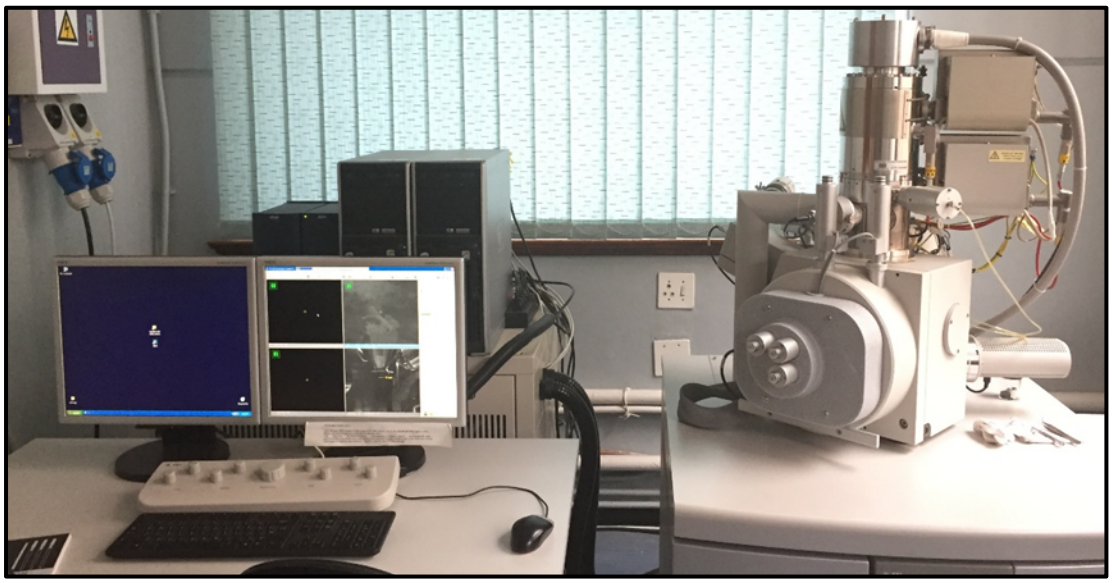

Figure 3.2: FEI Nova Nanolab 600 SEM.

In this study, as shown by Figure 3.2, FEI Nova Nanolab SEM was employed to determine the morphology and chemical composition of the nanomaterials (NMs). The fabricated NMs were spread on a carbon tape which was mounted to an aluminium stub. The prepared sample was then coated with a thin layer gold-palladium to prevent interference of the sample with electron beam (charging). The stub was mounted onto the stage of the microscope and the sample was analysed.

3.2.2. Transmission electron microscopy

TEM is a technique is based on electrons transmitting through the specimen for imaging the internal fine structure. The monochromatic beam of electrons are accelerated through a potential of 40 to 120 kV and passed through a strong magnetic field that acts as a lens (Kubo *et al*., 2013). It creates a different type of scattering during the interaction between the electron

beam and the specimen (i.e. inelastically, elastically and unscattered). Moreover, it provides information such as compositions, morphological, topographical and crystalline. Mostly, its resolution is approximately 2 nm (Kubo *et al*., 2013). The beam of electrons that are transmitted through an ultra-thin specimen wherein there is an interaction, as it passes through. The image forms as a result of the interaction between the specimen and electrons. Therefore, the image is enlarged and focused onto the imaging device such as fluorescent screen, on a layer of photographic film, or sensor such as charged-couples device (CCD) camera is used for detection. As the TEM images are of high quality and finest details entailing the internal structure can be observed. The information from TEM is dependent critically on the following components; highest resolving power of the microscope (i.e. often less than 3 nm), the energy spread of the electron beam (i.e. usually several eV), the thickness of the specimen (i.e. regularly less than 1μm and the stability), and composition of the specimen (Goodhew, 2011). The appropriate specimen should be a weak phase object that is extremely thin and that permits the electron beam to pass through. However, the amplitude should not be affected as the modest phase shift might occur (Goodhew, 2011). Thus, TEM is a versatile technique for its multiple use and/or applications.

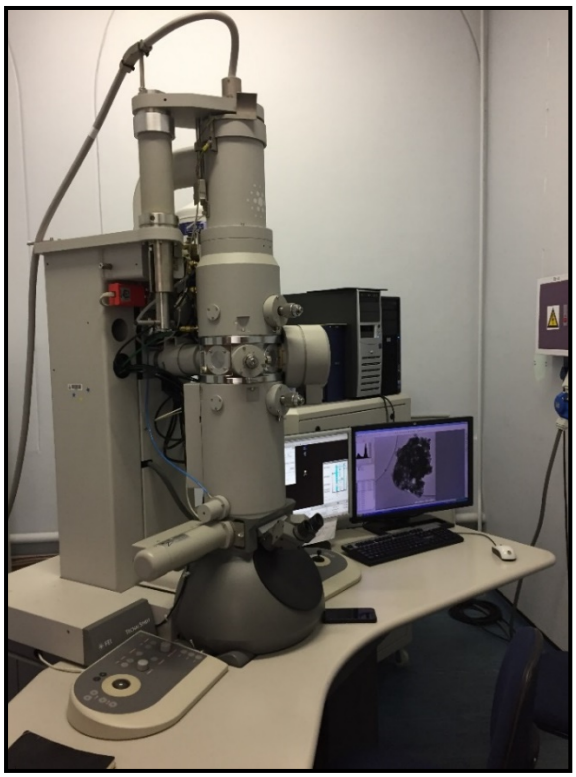

Figure 3.3: A FEI Tecnai T12 TEM.

In this study, the FEI Tecnai T12 TEM (as depicted by Figure 3.3), was employed to study the morphology of the nanomaterials (NMs). The sample preparation entails; a tiny amount of NMs added into a vial with a dispersing medium (methanol) and ultra-sonicated until it was completely dispersed, to achieve a homogeneous suspension of the NMs. The droplets of the solution were deposited on to the copper grid (i.e., Structure Probe, Inc. (SPI) Carbon grid (200 mesh)) and it was then permissible to dry at room temperature. The copper grid was mounted onto the sample holder, then into the sample chamber of the instrument, and then analysed at a 120 KeV accelerating voltage. These aforementioned electron microscopies are commonly coupled to EDX. This analytical technique is typically utilised for quantifying and qualifying all elements (excluding H, He and Li) and also the chemical composition of extremely small material. All Element have distinctive atomic structure and thus there can be distinguished on the electromagnetic emission spectrum with distinctive peaks. It is founded on the interaction of the specimen with the X-ray beam.

These X-rays have wavelength and energies pertaining to the element's characteristic (Ferrando, 2016). The high beam of X-rays are directed onto the specimen. Atoms inside the specimen that have unexcited electron leaps to the nucleus, when at rest. The electron in the inner shell might be excited by the incident beam that results in ejecting an electron from the shell causing a hole due to the ejected electron. The electron from the outer, higher-energy shell migrates to the hole to fill it. This movement results in energy difference between higher energy and the lower energy shell forming an X-ray (Rahman *et al*., 2011). Moreover, TEM can be coupled with EDS in which the EDS measures the energy of the emitted X-rays from the specimen. The difference in energy between the two aforementioned shells is the characteristic of the X-rays energy including the atomic structure of the element from the source of emission; that is ideal for the measurement of the elemental composition of the specimen. A spectrum with a total amount of the element, peak patterns histogram, and map images can be used to represent the data from EDS. The plot of data on the spectrum is the energy level received from the X-ray. The peak height or intensity shows the percentage of the element. In this study, EDX analysis was employed for elemental analysis of NMs.

3.3. Thermal gravimetric analysis

TGA is a technique in the family of the thermal analysis that is simple with high precision. TGA is utilized to determine the temperature at which the material decomposes. It is usually

operated at a temperature up to 1000 °C (Ng *et al*., 2018). The purity and thermal stability of the materials fabricated, and the residual of the catalyst left can be obtained. The mass of the material is monitored as a function of temperature and time, within a controlled atmosphere (i.e. air and N_2) wherein the temperature program is also controlled. The material display weight loss or gain, because of decomposition, oxidation, or dehydration. TGA is effective for quantitative analysis of thermal reactions that are associated with mass changes.

The desired mass (as per instrument's specification) is placed on the sample holder on top of a recording balance, in a controlled atmosphere within a furnace, where the temperature programme is utilized to gradually heat the sample until the desired temperature is reached. The mass is recorded onto the balance over a specified time. There are some parameters affect the TGA data such as furnace heating rate, furnace atmosphere, the weight of the sample and the sample particle size (Ng *et al*., 2018).

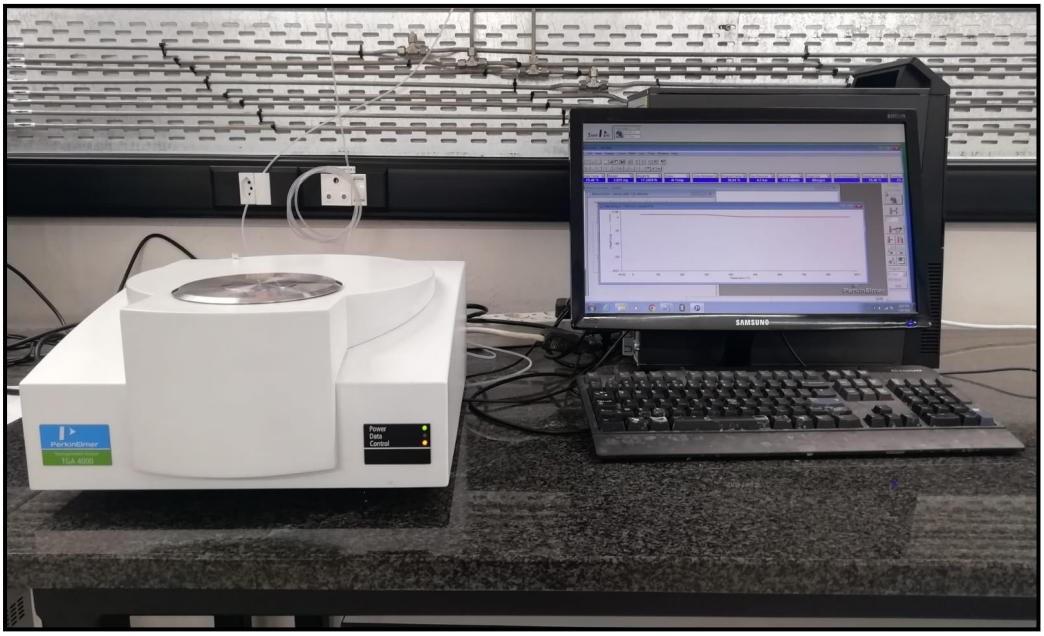

Figure 3.4: Perkin Elmer TGA STA 4000 series.

In this study, the Perkin Elmer TGA STA 4000 depicted in Figure 3.4, was employed in the characterisation of the fabricated NMs. It was utilised to determine the mass loss of the fabricated NMs. Approximately 10 mg of the NMs was placed onto a ceramic pan (i.e. sample holder) which were supported onto an analytical balance found in the chamber of the furnace in the analyser. The sample material was heated in a stream of air at heating rate of 20 °C/min from 35 to 900 °C. The results were evaluated using the Pyris software and the data was given

as a plot of mass change (in percentage) versus temperature. These data gave information about the purity and thermal stability of the NM.

3.4. X-ray photoelectron spectroscopy

XPS is an analytical technique that is non-destructive, powerful, and versatile that falls within the family of electron spectroscopies. It is also referred to as electron spectroscopy for chemical analysis. It entails surface analysis, typically used for establishing the elemental, chemical and electronic structure and the chemical state of the compound (Mattox, 2012). It is based on the photoelectric effect (Ferrando, 2016). The photoelectric effect involves ejecting electrons on the surface of the material, due to the interaction with photons. It usually requires a low-energy (i.e. 1.5 KeV) (Franinović, 2012). The penetrating depth in a solid material is the order of 1-10 micrometres (Moulder *et al*., 1992). The technique is used to determine the kinetic energy spectrum of photoelectrons that are ejected from the specimen's surface area through irradiating constant energy, hv, in a vacuum that is typically better than 10^{-7} Pa (Konno, 2016). This can be represented by the equation below.

$$\boldsymbol{KE = hv - BE - \emptyset} \qquad \textbf{3.2}$$

where BE is the binding energy, hv is the photon energy and $\emptyset$ is the work function. Typical soft X-rays utilised include MgKα (1235.6 eV) or AlKα (1486.6 eV) (Moulder *et al*., 1992). The binding energies are distinctive to each element and they are utilised to ascertain and determine the concentration of the exterior elements. All elements can be analysed but excluding H and He; due to their low atomic number (i.e. below 3). The specimen is irradiated with soft X-rays on the surface. However, these X-rays are filtered before irradiating in which the electron in the core are emitted after absorbing a photon, leading to a photoelectric effect. These emitted photoelectrons are divided according to their respective energies. The entire photon-electrons that were emitted are denoted by atomic level, then sent to the detector. Thus, the total number of the emitted electrons is relative to the concentration of the emitted electrons on the surface.

Figure 3.5: A PHI 5000 Versaprobe XPS.

In this study, the XPS PHI 5000 Versaprobe system with a Al Kα X-ray source, as depicted in Figure 3.5, was employed in the characterization of the fabricated NMs. The specimen was flat and smooth, which was mounted onto the sample holder; latter to the sample chamber. The spectra was recorded with aluminium anode (Al Kα = 1486.6 eV) operated at 50 μm, 12.5 W and 15 kV energy. The plot of data obtained is the intensities of photoelectrons against the binding energy or kinetic energy. The computer software (Multipak version 8.2) was utilized to analyse XPS data.

3.5. Raman spectroscopy

Raman spectroscopy is a powerful, rapid, non-destructive analytical technique; that is founded on scattering as a result of the Raman effect (Bumbrah and Sharma, 2016). Raman scattering is the process of inelastic light scattering. In this case, the energy is exchanged between the incident, exciting electromagnetic wave and ionic lattice of the solid material (Ferrando, 2016). It gives a depth understanding in the fundamental aspect of all types of hybridizations from three to zero dimensional NMs including graphite, graphene, CNTs and fullerenes in terms of electronic and vibrational properties (Dresselhaus *et al*., 2010; Dresselhaus, Jorio and Saito, 2010). The graphitic material such as MWCNTs on the Raman spectra has spectral features that are characterised by distinctive peaks which are; (1) the G-band between the 1580 cm^{-1}

and 1604 cm^{-1} region and also G-band at 2683 cm^{-1}, (2) D-band and 2D-band around the 1342 cm^{-1} and also around 2600 cm^{-1} region respectively (Bokobza and Zhang, 2012). The quality of the sample is measured by the peak area ratios (i.e. I_d/I_g) (Costa *et al*., 2008).

During sample analysis, the monochromatic radiation illuminates the sample whereby there is an interaction between the sample and light which results in the light beam reflected, scattered and/or absorbed. Raman is based on scattering and thus the scattering has molecular information of the sample. It utilises the laser source to radiates the sample, that results in elastic scattering also known as Rayleigh scattering and a minor fraction of inelastic scattering also known as Raman scattering. The charge coupled device (CCD) detector captures the resulting beam, then data is transformed into a Raman spectrum. This spectrum gives information such as crystalline size, clustering of the sp^2 phase, the presence of sp^2 or sp^3 hybridization, introduction of chemical impurities, the magnitude of the mass density, the optical energy gap, elastic constant, doping, defects and other crystal disorder, edge structure, strain, number of graphene layers, nanotube diameter, chirality, curvatures and lastly the metallic versus semiconducting behaviour (Ferrari and Robertson, 2004).

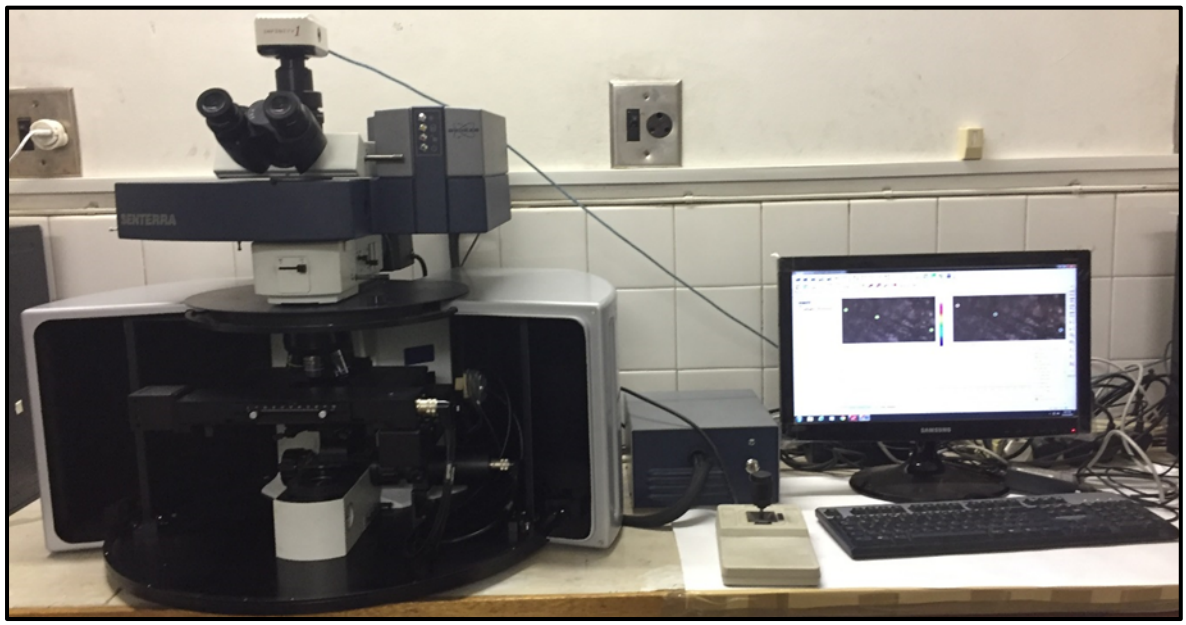

Figure 3.6: Bruker Senterra Raman Spectroscopy.

In this study, the Raman spectroscopy Bruker Senterra depicted in Figure 3.6, was employed in the characterisation of the fabricated NMs. It was fitted with 50x objective lens that was utilised for imaging the sample. The laser excitation wavelength was set at 532 nm. The spectra

were recorded between the ranges of 4000 cm^{-1} to 10 cm^{-1}. The spectral data were evaluated using the OPUS software. As a result, the fabricated NMs were characterised to determine the graphicity and crystallinity. However, Jobin-Yvon T64000 Ultraviolet (UV) LabRam HR-micro Raman spectrometer with an Olympus BX41 microscope was also used to analyse some samples that was operated at 514.5 nm.

3.6. Brunauer-Emmett-Teller

The BET technique is widely utilised to estimate the overall surface area measurement through surface adsorption with the uptake of a gas molecules, micropore volume (t-plot) method and pore size through the adsorption and desorption isotherms. This technique was firstly used by Stephen Brunnauer, Paul Hugh Emmett and Edward Teller in 1938. The technique is an extension of the Langmuir theory which represents the surface area. The use of liquid N_2 at low temperature (i.e. -195 °C) was used as adsorbate. It denotes the monolayer adsorption and half multi-layer adsorption capacity and assume the adsorption technique that there is a surface homogeneousness to complete gas adsorption at a permeating level, limited interaction of molecules and also at different kinetic limitation (Brunauer *et al*., 1938).As previously mentioned in the assumptions, the BET equation can be used to determine the rate of adsorption and desorption (Siperstein *et al*., 2021).

$$\boldsymbol{v = \frac{V_m cP}{P_o} - P\left[1 + \frac{(c-1)P}{P_o}\right]} \qquad \textbf{3.3}$$

Where v is the adsorbed volume, v_m is the monolayer volume absorbed, P is the pressure (equilibrium), P_o is the permeation pressure at the temperature of the isotherm, c is the BET constant adjusted parameter.

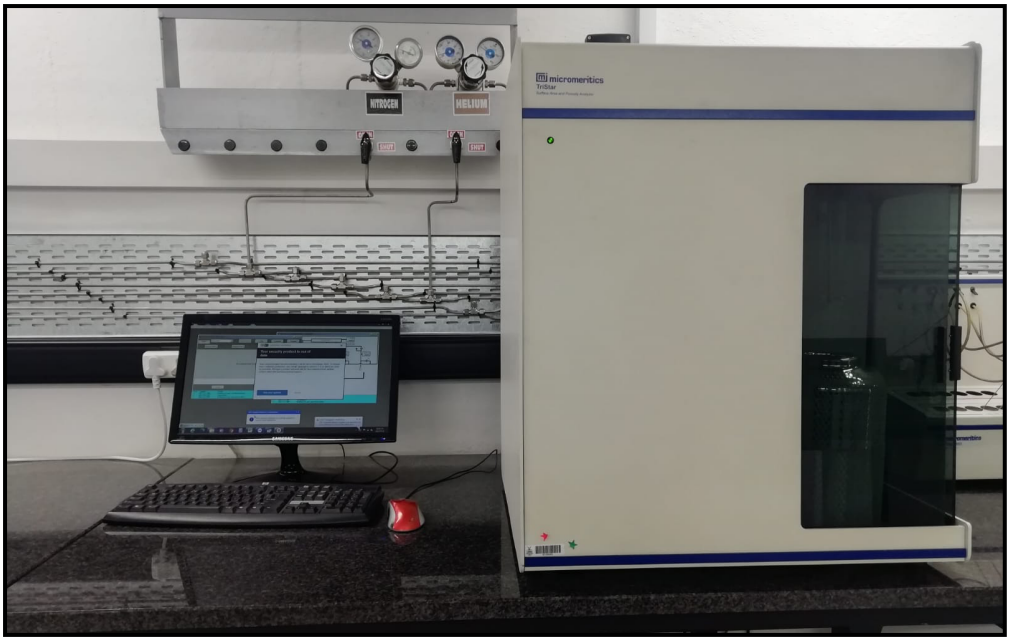

Figure 3.7: A Micromeritics RS232 Brunnauer -Emmett-Teller (BET) surface area and porosity analyser.

In this study, the BET instrument depicted by Figure 3.7, was employed in the characterisation of the fabricated NMs. It was utilised to estimate the surface area, pores size and pore volume. Approximately 100 mg was weighed and transferred into the glass tube. The samples was degassed under liquid nitrogen at 150 °C overnight using vacuum pump, this was done to remove impurities thereafter the degassed sample was transferred to the analyser (Tristar) for analysis. In which the sample was exposed to N_2 at various relative pressure or saturation vapour pressure (P_o) that resulted in adsorption being recorded. The computer program determined/evaluated the surface area of the samples utilising the adsorption isotherms through relating the surface area to the volume of the gas adsorbed on the samples (NMs) as a monolayer coverage.

3.7. Atomic Absorption Spectroscopy

AAS is an non-destructive analytical technique that is simple and reliable in quantification and qualification of metal and metalloids that needs to be in liquid (Garca and Báez, 2012). The sample are treated with the acid to convert them into liquids for easier conversion to gaseous phase. It uses a hallow cathode lamps as a radiation source. The lamp is created with the tungesten anode and a hollow cylindrical cathode used for the determination of the element of interest in a glass tube filled with argon gas to establish an inert environment. In addition, it

consist of atomizer that convert the liquid sample into gaseous phase. The gaseous phase of the sample is then transported into the monochromator in which the light source convert the sample into a amplified electrical signal that can be recorded. The signal is then sent to the detector to be converted into a spectrum that gives information about the amount or concentration of the element of interest being investigated.

Figure 3.8: An Agilent Technologies 200 series AAS.

The filtered liquid sample (~10 mL) is introduced by being aspirated into the flame. The flame is usually created by using acetylene or air etc. In this study, Agilent Technologies 200 series AAS as shown in Figure 3.8, was utilized in the determination of the final concentraion if the Pb^{2+} ions post adsorption.

References

Anjum, D.H., 2016. Characterization of nanomaterials with transmission electron microscopy. *IOP Conference Series: Materials Science and Engineering*, 146 (1), 012001.

Bokobza, L., Zhang, J., 2012. Raman spectroscopic characterization of multiwall carbon nanotubes and of composites. *Express Polymer Letters*, 6, 601–608.

Bozzola, J.J., 2001. Electron Microscopy. *In: Encyclopedia of Life Sciences*. Chichester, UK: John Wiley & Sons, Ltd, 603–614.

Brunauer, S., Emmett, P.H., and Teller, E., 1938. Adsorption of gases in multimolecular layers. *Journal of the American Chemical Society*, 60 (2), 309–319.

Bumbrah, G.S., Sharma, R.M., 2016. Raman spectroscopy – Basic principle, instrumentation and selected applications for the characterization of drugs of abuse. Egypt. *Journal of Forensic Science*, 6, 209–215.

Bunaciu, A.A., Udriştioiu, E. Gabriela, Aboul-Enein, H.Y., 2015. X-ray diffraction: Instrumentation and applications. *Critical Reviews in Analytical Chemistry,* 45, 289–299.

Chatterjee, N., 2012. Electron Microprobe Analysis.

Costa, S., Borowiak-Palen, E., Kruszyńska, M., Bachmatiuk, A., Kaleńczuk, R.J., 2008. Characterization of carbon nanotubes by Raman spectroscopy. *Material Science*, 26.

Dresselhaus, Mildred S., Jorio, A., Hofmann, M., Dresselhaus, G., Saito, R., 2010. Perspectives on carbon nanotubes and graphene Raman spectroscopy. *Nano Letters,* 10, 751–758.

Dresselhaus, M.S., Jorio, A., Saito, R., 2010. Characterizing graphene, graphite, and carbon nanotubes by Raman spectroscopy. *Annual Review Condensed Matter Physics*, 1, 89–108.

Ferrando, R., 2016. Synthesis and Experimental Characterization of Nano alloy Structures. *In: Frontiers of Nanoscience*, Elsevier Ltd, pp. 47–74.

Ferrari, A.C., Robertson, J., 2004. Raman spectroscopy of amorphous, nanostructured, diamond-like carbon, and nanodiamond. *Philosphical Transactions of the Royal Society A Mathematical Physical and Engineering Sciences*, 362, 2477–2512.

Franinović, M., 2012. X-ray photoelectron spectroscopy.

Garca, R. and Báez, P.A., 2012. Atomic absorption spectrometry (AAS). *In: Atomic Absorption Spectroscopy*, InTech, 99–100.

Goodhew, P.J., 2011. General introduction to transmission electron microscopy TEM. *In: Aberration-corrected analytical transmission electron microscopy*, John Wiley and Sons,

pp. 1–19.

Konno, H., 2016. X-ray photoelectron spectroscopy. *In: Materials Science and Engineering of Carbon*, Elsevier, pp. 153–171.

Kubo, T., Kobayashi, H., Hashimoto, T., Okada, M., Kondo, M., Nakano, K., Wayama, M., and Kamino, T., 2013. Applications of 40-120kV Analytical TEM for nanoscience. *Microscopy and Microanalysis*, 19 (S2), 1328–1329.

Mattox, D.M., 2010. Substrate ("real") surfaces and surface modification. *In: Handbook of physical vapor deposition (PVD) processing*, Elsevier, pp. 25–72.

Moulder, J.F., Stickle, W.F., Sobol, P.E.', Bomben, K.D., Chastain, J., 1992. Handbook of X-ray photoelectron spectroscopy a reference book of standard spectra for identification and interpretation of XPS data. Perkin-Elmer Corporation, Minnesota.

Ng, H.M., Saidi, N.M., Omar, F.S., Ramesh, K., Ramesh, S., and Bashir, S., 2018. Thermogravimetric analysis of polymers. *In: Encyclopedia of Polymer Science and Technology*, Hoboken, NJ, USA: John Wiley & Sons, Inc., 1–29.

Rahman, M.M., Khan, S.B., Jamal, A., Faisal, M., Aisiri, A.M., 2011. Iron oxide nanoparticles.

Siperstein, F.R., Avendaño, C., Ortiz, J.J., and Gil-Villegas, A., 2021. Analytic expressions for the isosteric heat of adsorption from adsorption isotherm models and two-dimensional <scp>SAFT-VR</scp> equation of state. *AIChE Journal*, 67 (3), 1–12.

Udochukwu, M., 2005. Applications of Electron Microscopy in Materials and Metallurgical Engineering, Owerri.

CHAPTER 4

Synthesis of Chlorinated Nitrogen-doped Carbon Nanotubes (ClNCNTs) and Their Surface Modification with Fe_3O_4 Nanoparticles

4. Introduction

This chapter presents the production of chlorinated nitrogen-doped carbon nanotubes (ClNCNTs) by pyrolysis of a mixture of acetonitrile and dichlorobenzene over bi-metallic catalyst (Fe-Co/$CaCO_3$) using a CVD method. Fe_3O_4 nanoparticles (NPs) were also loaded onto the surface of the ClNCNTs using the co-precipitation method. Effect of different loadings of iron oxide by varying the added iron salt concentration was also evaluated on the distribution of the nanoparticles on the surface of the ClNCNTs.

4.1. Study background

Carbon nanotubes (CNTs) possess unique properties which include high mechanical strength and high electrical, and thermal conductivities. These properties make them ideal to be used in various nanoscience and nanotechnology fields such as gas sensors, biomedical, electrochemistry, water treatment, catalysis, etc. CNTs are commonly produced with methods such as arc discharge, laser ablation and chemical vapour deposition (CVD). The horizontal CVD is the favourable method, because it is simple and uses low power (Singh and Song, 2001; Mabena *et al*., 2011). Furthermore, it simultaneously allows for the production of CNTs using highly excessive carbon sources (i.e. acetylene) and in-situ surface modification of the CNTs (Singh and Song, 2001). Surface modification with chlorination (Maboya *et al*., 2016) and doping with nitrogen (Tetana *et al*., 2012) have been previously reported.

It was found that chlorination created defects on the walls of the CNTs which resulted in secondary growth of carbon nanofibers (CNFs) on the outer walls of the main CNTs (Maboya *et al*., 2016), while doping with nitrogen using precursors such as acetonitrile altered the morphology of the CNTs resulting in bamboo-like structures with compartments that resulted in increased structural defects of the material (Tetana *et al*., 2012). Furthermore, nitrogen doping modified the inherent properties including the adsorption sites of the CNTs (Amadou *et al*., 2008; Zhou *et al*., 2004). In other studies it was shown that addition of a mixture of nitrogen and chlorine sources during production of CNTs resulted in the improvement of their field emission properties due to defects created (Ray, 2018). Synthesis of ClNCNTs using an injection CVD method, resulted in CNTs of various interesting morphologies that depended

on the amount of chlorine added to the feed and some were open-ended whilst others were closed-ended (Maboya *et al*., 2021). Thus, it is envisaged that doping CNTs with nitrogen and surface modification with chlorine may result in production of materials that can be applied in various fields. Defect sites in these materials can be used as attachment sides for metal nanoparticles and can aid in increasing their adsorption properties. The increased adsorption sites are vital for various nano-adsorption studies and other applications such as field emission devices.

Carbon nanomaterials have been modified with various inorganic particles in order to enhance their applications in specific fields. For example, in water treatment carbon nanotubes were modified with magnetic metal oxide nanoparticles in order to render them recoverable after use as adsorbents. In antibacterial studies, they have been modified with metal or metal oxide nanoparticles in order to enhance their antibacterial activities. Inorganic nanoparticles that are used to modify the surface of the CNTs include metal oxides such as magnetite (Fe_3O_4), maghemite (γ-Fe_2O_3) and hematite (α-Fe_2O_3). Several studies were reported in which the effective loading of Fe_3O_4 nanoparticles onto the CNTs exterior were done using techniques such as chemical evaporation (Masipa *et al*., 2013), thermal decomposition (Maity *et al*., 2008), hydrothermal (Yu *et al*., 2017), sonochemical (Rahmawati *et al*., 2017) and co-precipitation (Abdalla *et al*., 2016). Co-precipitation was the favourable method because it is fast, simple and requires low power use.

The modification of CNTs with metal oxides has enhanced their functionality to advance them in the fields such as gas sensors (Elnabawy *et al*., 2019), adsorption (Zong and Gou, 2014), catalysis (Safari and Zarnegar, 2013), biomedical (Abdollah *et al*., 2017) and so forth. The magnetic metal oxide nanoparticles (i.e. Fe_3O_4) are favourable, based on properties such as low toxicity and biodegradability (Yu *et al*., 2017). In order for Fe_3O_4 to attach to the exterior surface of the CNTs, the activation of the support via oxidation with nitric acid is needed. Oxidation with nitric acid create defects on the CNT walls, forming COOH, C=O and C-OH functional groups through covalent linkages (Mallakpour and Soltanian, 2016). At these defect sites, nucleation of the Fe_3O_4 nanoparticles occurs resulting in the formation of the Fe_3O_4/CNTs nanocomposite. The nanocomposite has properties such as higher chemical specificity (Matei *et al*., 2011), high adsorption capacity (Elnabawy *et al*., 2019), superparamagneticity, good surface area and high reactivity (Dong *et al*., 2009). Thus, the

enhanced properties of the nanocomposite, has potential to be applied in water treatment as nano-adsorbents. Therefore, it is envisaged that combining both the Fe_3O_4 and CNTs nanoparticles (especially with a particle size of less than 50 nm) (Matei *et al*., 2011) can result in creation of nanocomposites that possess improved adsorption properties. Moreover, this inherent characteristic will heighten the water treatment field and will allow for easy separation.

Hence, the main focus of this study was to synthesise and evaluate the role of both chlorine and nitrogen on the morphology of the CNTs. We also report on the modification of the surface of this chlorinated nitrogen-doped CNTs with different loading of magnetic Fe_3O_4 nanoparticles. The Fe_3O_4 loaded and un-loaded ClNCNTs were characterized using transmission electron microscopy (TEM), Energy-dispersive X-ray spectrocopy coupled with SEM, powder X-ray diffraction spectroscopy (p-XRD), Raman spectroscopy, Thermal gravimetric analysis (TGA), Brunauer, Emmett and Teller (BET) and X-ray photoelectron spectroscopy (XPS) techniques.

4.2. Experimental Procedures

4.2.1. Materials

Acetonitrile (CH_3CN), 1,2-dichlorobenzene (DCB), nitric acid (HNO_3), calcium carbonate ($CaCO_3$), ammonium iron(II) sulphate hexahydrate ($(NH_4)_2Fe(SO_4)_2.6H_2O$), ammonium hydroxide, cobalt (II) nitrate hexahydrate ($Co(NO_3)_2•6H_2O$), Iron (III) nitrate nonahydrate ($Fe(NO_3)_3•9H_2O$), Iron (III) chloride hexahydrate ($FeCl_3•6H_2O$), and ethanol (C_2H_5OH, 99%) were purchased from Sigma Aldrich and were all used as received.

4.2.2. Preparation of the bi-metallic catalyst

The 10% Fe-Co/$CaCO_3$ was prepared using the steps outlined and also completely characterized in the previous work reported by Mhlanga *et al*., (2009). The report also presents detailed information on the material's optimization and characterization. In this work, the material was used as a catalyst in the synthesis of ClNCNTs. However, the catalyst method of preparation was such that the calculated quantities of $Fe(NO_3)_3•9H_2O$ (4.02 g) and $Co(NO_3)_2•6H_2O$ (2.93 g) nitrates were weighed and transferred into two separate beakers. Precisely, about 15 mL of distilled water was added into each beaker containing the inorganic salts to create 0.3 M Fe and 0.3 M Co precursor solutions and then later mixed in a beaker and

transferred into a burette. The mixture was added dropwise using a burette to a beaker containing 10 g of $CaCO_3$ support while stirrring using a magnetic stirrer at room temperature. The mixture was stirred for a further 30 min and directly dried in an oven for 16 h at 100°C. Thereafter, the product (of the mixture) was cooled to room temperature and transferred to a mortar for it to be grounded with a pestle until a fine powder was produced, this was followed by screening with molecular sieves. The catalyst powder was then calcined at 400 °C for 16 h in a static air oven.

4.2.3. Synthesis and purification of ClNCNTs

The production of ClNCNTs was carried out using the method by Maboya *et al*., (2018). Figure 4.1 shows a schematic representation of the CVD reactor that was used for the synthesis of ClNCNTs. CNTs were synthesized at 800°C under an C_2H_2 (90 mL/min) and N_2 (240 mL/min) atmosphere. Briefly about 1.00 g of the catalyst was weighed and transferred to a quartz boat which was then inserted into the quartz tube. The quartz tube was inserted into the furnace. The time and temperature of the reaction was set at 1 h and 800 °C, respectively. N_2 was bubbled into the reactor at 40 mL/min while the reactor's temperature was raised to 800 °C at the heating rate of ~10 °C/min. The flow of N_2 was then adjusted to 240 mL/min, and C_2H_2 (90 mL/min) was introduced into the system when the temperature had reached 800 °C. The two gases were bubbled through an acetonitrile:dichlorobenzene (CH_3CN:DCB) solvent mixture of 1:1 volume ratio and the vapors were flown into the reactor. After 1 h of reaction, the system was cooled to room temperature in the presence of N_2 (40 mL/min) before removing the product from the reactor. The product was weighed and then purified with a 30 % HNO_3 at 110 °C for 4 h and later dried in an oven at 100 °C overnight.

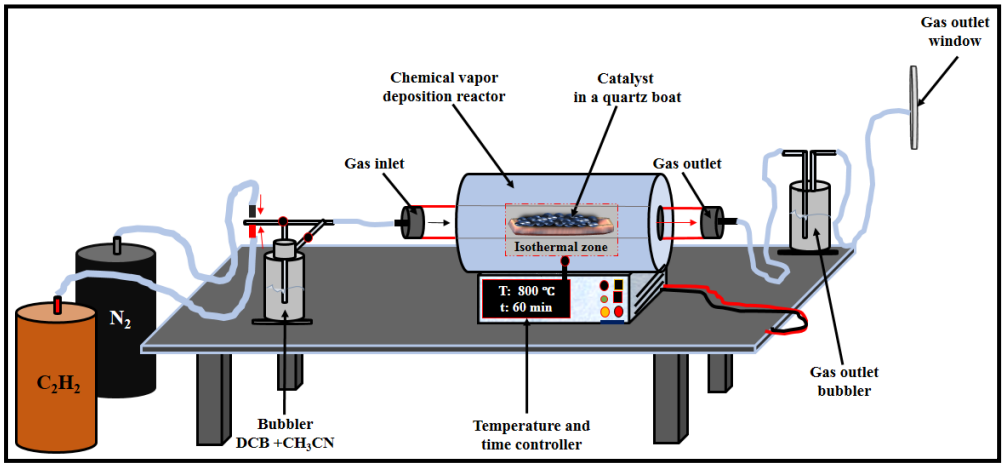

Figure 4.1: The schematic presentation of a CVD used to synthesize ClNCNTs.

The carbon yield reported in percentage was calculated using the formula below (Romero et al. 2007):

$$Carbon\ (\%) = \frac{[M_{tot} - M_{cat}]}{M_{cat}} \times 100 \qquad 4.1$$

where M_{cat} is the quantity of the catalyst and M_{tot} is the total weight of the sample after fabrication. Thus it was found that, when 1.0 g of a bi-metallic catalyst was used, about 3.9 g of the carbonacious product was produced.

4.2.4. Synthesis of ClNCNTs/Fe_3O_4 nanoparticles

The purified ClNCNTs were used as support for loading the Fe_3O_4 nanoparticles. The synthesis or metal oxide loading procedure was adapted from Daneshvar Tarigh and Shemirani, 2013. About 0.21 g of $(NH_4)_2Fe(SO_4)_2 \cdot 6H_2O$ and 0.18 g $FeCl_3 \cdot 6H_2O$ were dispersed in 50 mL of distilled water by vigorous stirring. The purified ClNCNTs (~ 0.15 g) was then added to the solution and the mixture was stirred at 70 °C under an argon atmosphere for 10 min. The pH was adjusted to 10 by adding 5 mL of 0.8 M NH_4OH solution dropwise. The reaction was further stirred at 70 °C for 30 min and allowed to cool to room temperature. The product was then filtered by making use of a magnet to separate the Fe_3O_4/ClNCNTs from the solvent. The Fe_3O_4/ClNCNTs composite was washed with distilled water several times until the pH reached 7, followed by washing with 150 mL of ethanol. The composite formed was dried at 60 °C overnight. The schematic presentation of the synthesis method is presented in Figure 4.2.

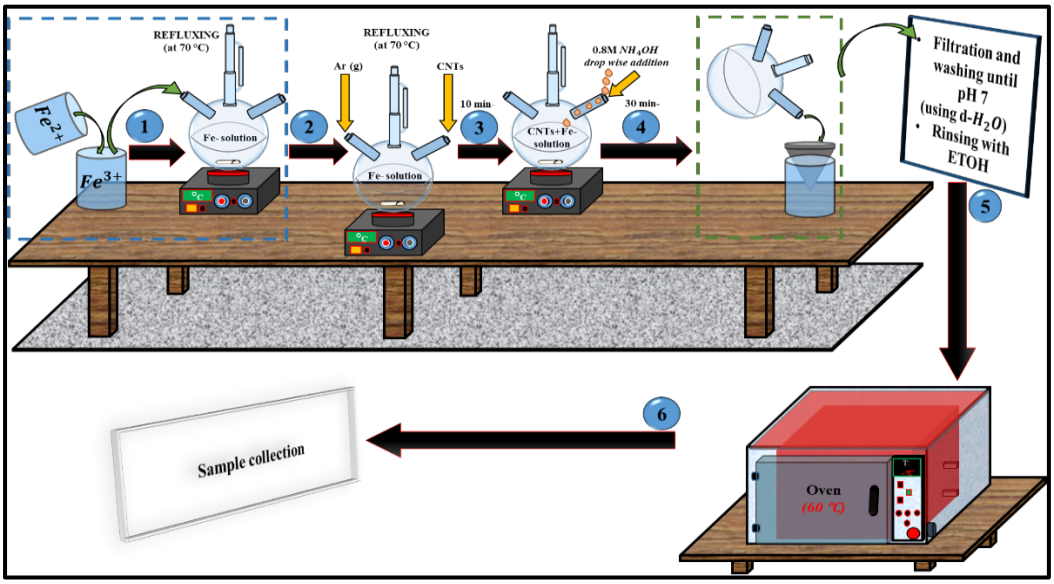

Figure 4.2: The schematic presentation of a reflux system used to synthesize Fe_3O_4/ClNCNTs via a co-precipitation method.

The above method produced ClNCNTs with 53 % Fe_3O_4 loading. The synthesis procedure was repeated varying the metal loadings to 10, 20 and 30 % by varying the amounts of $(NH_4)_2Fe(SO_4)_2 \cdot 6H_2O$ and $FeCl_3 \cdot 6H_2O$. Table 4.1 shows the various amount of the metal salts used for each loading.

Table 4.1: Reaction parameters of the loading of Fe_3O_4 onto ClNCNTs.

Fe_3O_4 loading (%)	Fe^{2+} (g)	Fe^{3+} (g)	Temperature (°C)	Reaction time (min)
10	0.04	0.03	70	40
20	0.08	0.07	70	40
30	0.12	1.00	70	40
***53**	0.21	0.18	70	40

*reference percentage loading

4.2.5. Characterization techniques and data analysis

The materials were characterized using the following techniques: TEM, PXRD, EDX, Raman spectroscopy, XPS, TGA and BET (see Chapter 3 for detailed instrument settings).

Briefly, the morphology and size distribution of the CNTs before and after HNO_3 acid treatment were analysed by transmission electron microscopy (TEM) using a FEI TECNAI G^2 SPIRIT. The samples for TEM analysis were prepared by sonication in ethanol and thereafter deposited on a holey carbon-coated TEM Cu grid. The morphology and size distribution of the CNTs were also determined by scanning electron microscopy using FEI Quanta 400. The powdered samples were placed on top of a tape that was attached to a stub. The samples were coated with carbon and palladium to prevent them from charging. The CNTs were also characterized by Raman spectroscopy using a Jobin-Yvon T6400 micro-Raman spectrometer. Excitation was provided by a 532 nm green laser with spectral resolution of 3-5 cm^{-1}. The impurity content of the CNTs was monitored by thermogravimetric analysis (TGA) using a Perkin Elmer TGA 7. The sample was loaded onto a platinum pan and heated to 900 °C at a heating rate of 5 °C/min, in a flowing air stream at 20 mL/min. XPS analysis was performed using a PHI 5000 Versaprobe – Scanning ESCA Microprobe operating with a 100 µm 25 W 15 kV Al monochromatic X-ray beam. The samples were sputtered with a 2kV 2µA 1×1mm raster – Ar ion gun at a sputter rate of about 18 $nm.min^{-1}$ for 60 seconds.

4.3. Results and discussions

Different amounts (i.e. 10, 20, 30 and 53 wt.%) of Fe_3O_4 nanoparticles were loaded onto ClNCNTs in order to determine the optimun loading of nanoparticles as shown in Table 4.1 and the results are discussed below.

4.3.1. Structural Analysis

The morphology of the ClNCNTs un-loaded and loaded with Fe_3O_4 nanoparticles were characterized using TEM. Figure 4.3 shows TEM images of ClNCNTs and Fe_3O_4/ClNCNTs prepared with different metal salt loadings. Open-ended bamboo compartmeted CNTs and some hollow shaped CNTs were observed from the TEM image of ClNCNTs (Figure 4.3a). The ClNCNTs had an average diameter of 61 ± 32 nm (supplementary Figure S.1a), which was measured using Image J software. The open-ends are due to presence of chlorine and the bamboo-compartments are a result of nitrogen doping. After loading with Fe_3O_4 nanoparticles, the ClNCNTs maintained their morphology evidenced by bamboo-like compartments and hollow cavities as observed before (Figure 4.3b to e). Well distributed iron oxide nanoparti cles of uniform sizes distributed along the radial length of ClNCNT could be observed from materials loaded with 20 wt.% iron oxide (Figure 4.3c). The particle sizes of Fe_3O_4 nanoparticles at 20 wt.% loading appeared smaller with average sizes of 10 ± 4.5 nm and they exhibited spherical shapes (Figures 4.3c and 4.4), also measured using Image J software. The nanoparticles produced from materials produced from a 10 wt.% iron oxide (Figure 4.3b), also had small average diameters of around 10 nm (supplementary Figure S1b), but the nanoparticles appeared clustered but well distributed along the radial length of the CNTs. Increasing the metal loading to 30 wt.% (Figure 4.4d), resulted in formation of nanoparticles that are clumped together and were not well distributed, and the estimeted average particle size was about 17 ± 8 nm (supplementary Figure S1c). For 53 wt.% iron oxide loading (Figure 4.3e), the nanoparticles were agglomerated and situated in any position of the nanotube and the estimated average diameter was about 19 ± 4 nm (Figure S1d). Fe_3O_4 nanoparticles were attached at defect sites of the ClNCNTs which were enhanced by simultaneous inclusion of chlorine and nitrogen. Maboya *et al*., (2016) also observed that incorporation of chlorine into the structural matrix of CNTs resulted in growth of secondary carbon nanofibers on the outer walls of the main CNTs which were believed to have grown from defect sites created by chlorination.

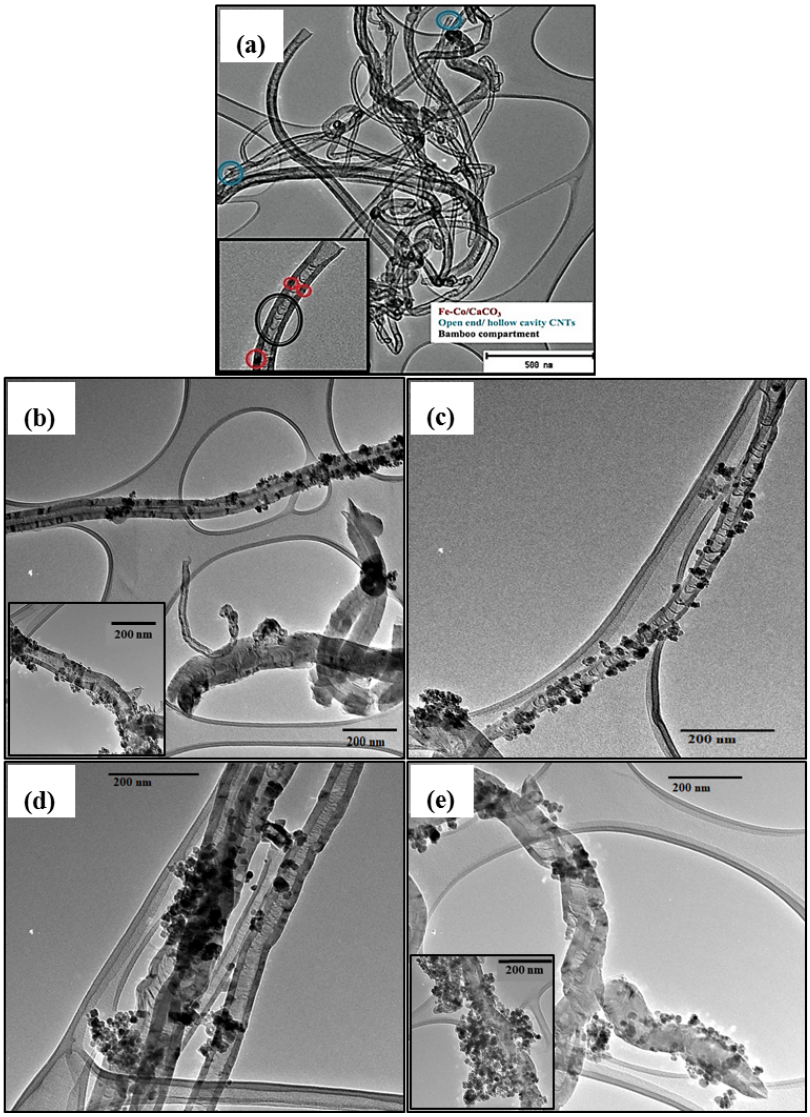

Figure 4.3: TEM images of ClNCNTs un-loaded (a) and loaded with Fe_3O_4 using metal salts of different weight percentages (b)10 wt.%, (c) 20 wt.%, (d) 30 wt.%, and (e) 53 wt.% .

Kayvani Fard and his co-workers, (2016) also studied the effect of different metal loadings (i.e. 1, 10, 30 and 50 wt.%) on the surface of the CNTs and their use as adsorbents for oil. They observed that when the ratio of metal loading was increased to 30 wt.% and 50 wt.%, the size of the Fe_3O_4 nanoparticles increased resulting in nanoparticle agglomeration *(*Kayvani Fard *et al*., 2016). Consequently, this study revealed that the 20 wt.% loading showed better distribution with minimal agglomeration of the Fe_3O_4 nanoparticles along the radial length of the ClNCNTs. Hence, the composite prepared with 20 wt.% loading of Fe_3O_4 nanoparticles was used as an adsorbent material for lead ion in this study.

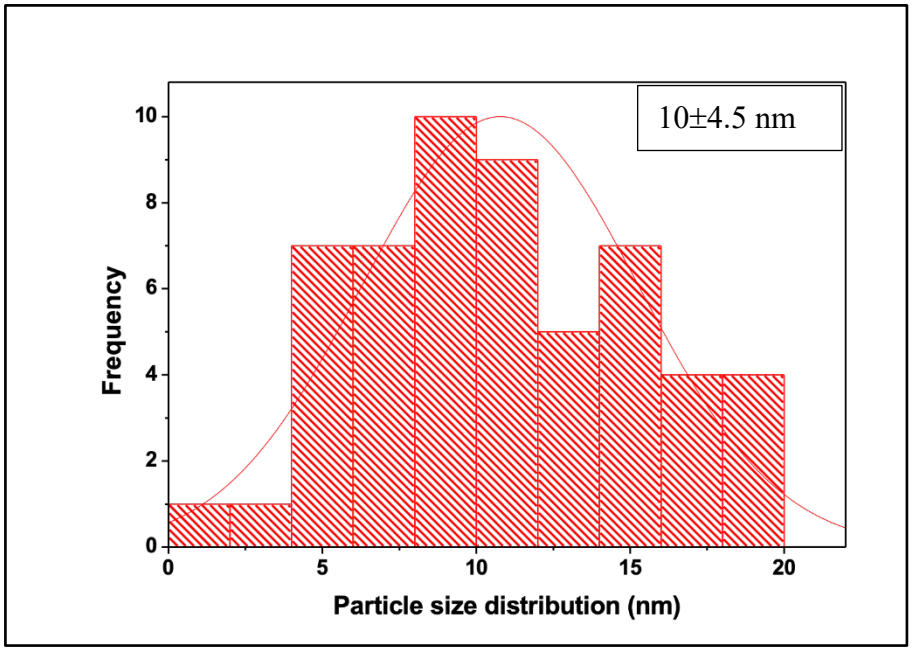

Figure 4.4: Histogram representing the average particles diameter of Fe_3O_4 nanoparticles loaded on ClNCNTs produced using a 20 wt.% metal loading.

4.3.2. Elemental and crystallographic analysis

The presence of Fe_3O_4 nanoparticles loaded on the surface of the ClNCNTs was also confirmed by EDX and XRD diffraction analysis. Elemental analysis data of the Fe_3O_4 un-loaded and loaded ClNCNTs, which represent the atomic weight percentage (wt.%) of the elements such as Fe, O and C is presented in Table 4.2. It was evident that the amount of both Fe and O in the samples increased with an increase in the weight percent of the metal solution added. Figure 4.5 presents the elemental distribution curve of a 20 wt.% metal loading and all the expected elements are present except N and Cl. The non-detection of N and Cl could be due to the detection limit of the EDX detector used by the SEM instrument, as the amount are minimals. It is worth noting that EDX is not a highly quantitative technique and that the part of the sample analysed is not a true representation of the whole synthesized material.

Table 4.2: EDX analysis of ClNCNTs un-loaded and loaded with Fe_3O_4 nanoparticles with different amounts of metal salt solution.

Element	CNTs Samples				
	ClNCNTs	Fe_3O_4 (10 %) /ClNCNTs	Fe_3O_4 (20 %) /ClNCNTs	Fe_3O_4 (30 %) /ClNCNTs	Fe_3O_4 (53%) /ClNCNTs
	wt.%	wt.%	wt.%	wt.%	wt.%
C	72.9	85.7	72.0	52.2	40.8
O	6.1	11.0	19.3	30.3	35.5
Fe	0.0	3.4	8.7	17.5	23.9
N	21.1	0.0	0.0	0.0	0.0
Total	100.0	100.0	100.0	100.0	100.0

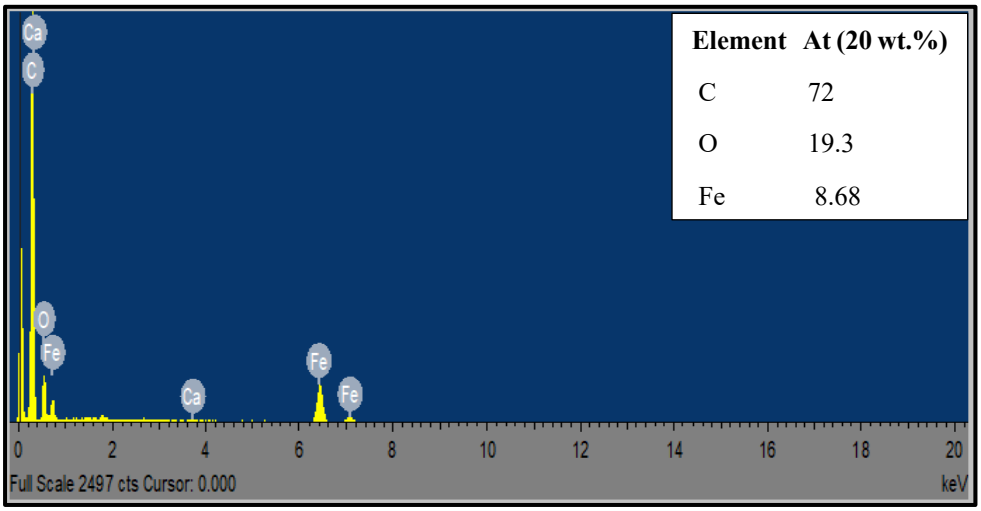

Figure 4.5: EDX of ClNCNTs loaded with Fe_3O_4 generated from a 20 wt.% metal salt solution.

Figure 4.6 shows the X-ray difraction patterns of ClNCNTs un-loaded and loaded with Fe_3O_4. The main diffraction peaks observed from the ClNCNTs materials were attributed to graphitic carbon structures at 2θ = 26.6 and 43° corresponding to the (002) and (100) difraction planes. The ClNCNTs un-loaded sample had an additional plane (101) that was previously attributed to the stacking of the honeycomb lattice layers (Lambin *et al*., 2002). For Fe_3O_4 loaded ClNCNTs, the (220), (331), (400), (422), (511) and (440) planes of Fe_3O_4 were observed at 2θ = 31°, 37°, 43, 54°, 58°, and 63°, which confirms successful loading. Loading with Fe_3O_4 has resulted in the shielding of the planes (100) and (101) in which similar observation were reported in literature by Rahmawati *et al*., (2017).

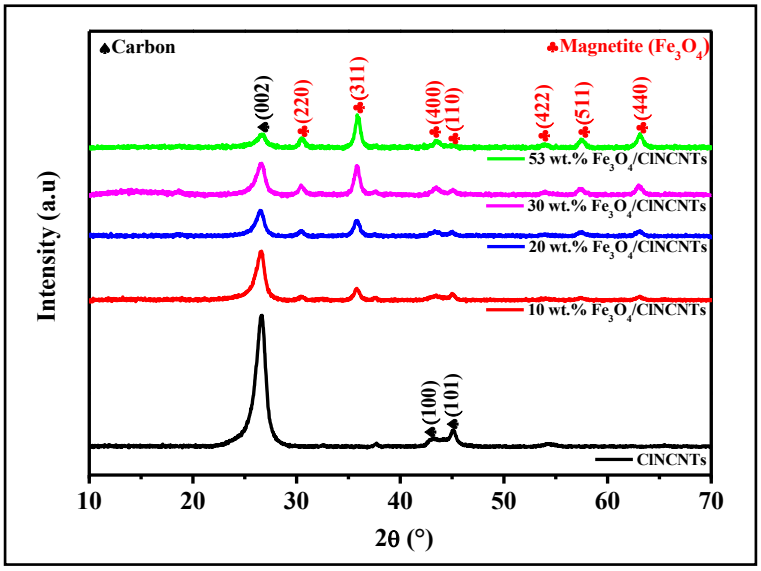

Figure 4.6: PXRD patterns of ClNCNTs un-loaded and loaded with with different metal salt loading of 10, 20, 30 and 53 wt.%.

The magnetite phase of the Fe_3O_4 loaded ClNCNTs was maintained regardless of the metal loading amount. It can be observed that the intensity plane of ClNCNTs at (002) decreased, while the planes indexed to Fe_3O_4 intensified with the increase in metal loading as supported by full width at half maximum data for the formation of Fe_3O_4/ClNCNTs nanocomposite (see Table 4.4). It might be attributed to the increase in the attachments of Fe_3O_4 NPs that are on the exterior of the CNTs (Zhou *et al*., 2016).

Table 4.3: Full width at maximum data from PXRD diffraction patterns of Fe_3O_4/ClNCNTs produced with different metal loading of Fe_3O_4: 10, 20, 30 and 53 wt.% metal solution loadings.

Phase	Plane	FWHM for Fe_3O_4/ClNCNTs with different metal loadings			
		10 wt.%	20 wt.%	30 wt.%	53 wt.%
Carbon	002	22.59	11.75	14.75	5.65
Magnetite	311	5.4	7.39	13.5	15.0
Magnetite:Carbon		1:0.24	1:0.63	1:0.92	1:2.65

4.3.3. Raman spectroscopy analysis

Raman spectroscopy is a technique that can be used to investigate the crystallinity and defects in the structure of the carbon nanomaterials and other nanomaterials. Figure 4.7 represents the Raman spectra of un-loaded ClNCNTs and Fe_3O_4 loaded ClNCNTs. Two intense peaks appearing at around 1359 cm^{-1} and 1575 cm^{-1} for both ClNCNTs and Fe_3O_4/ClNCNTs can be observed. The band centered at 1575 cm^{-1} is called the G-band and it demonstrates the graphite-like tangential mode, while the D-band centered at 1359 cm^{-1} is attributed to disorder and sp^3-hybridized carbon in the hexagonal framework of the nanotube walls. On the other hand, weak peaks at 1359 cm^{-1} and 1575 cm^{-1} were observed in the spectrum of Fe_3O_4/ClNCNTs in comparison to those of pure ClNCNTs. This may be due to the chemical interaction between CNTs and Fe_3O_4 nanoparticles in which the metal nanoparticles increased structural defects. This data correlates with both the TEM and the XRD where less ClCNTs and a reduction in the graphitic diffraction peak were observed with an increase in metal loading, especially at 53 wt.% metal loading.

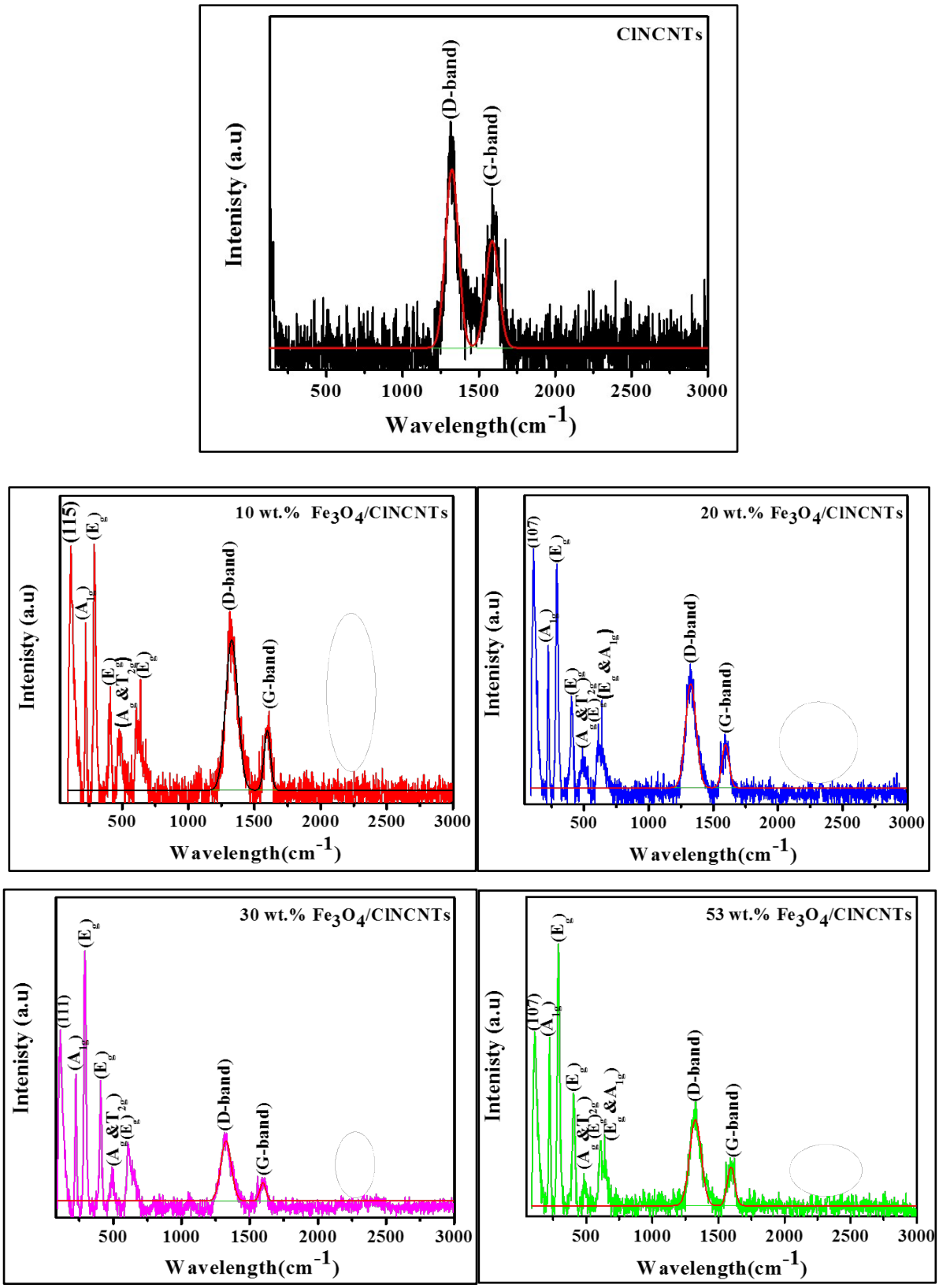

Figure 4.7: Raman spectra of ClNCNTs un-loaded and loaded with different metal salt loading of 10, 20, 30, and 53 wt.% respetively.

In addition to the G- and D-bands, there are peaks below 1000 cm^{-1} on the Raman spectra of Fe_3O_4 loaded ClNCNTs which can be attributed to the presence of Fe_3O_4. It is evident that the excitation of the laser power (60 mW) has changed the phase of Fe_3O_4 to α-Fe_2O_3, as depicted on Table 4.4 and similar observations were reported in the literature (Sathish *et al*., 2012, Owens and Orosz, 2006). The vibrational modes in the range between 474-490 cm^{-1} and also 643-651 cm^{-1} are reported to be the characteristic of both α-Fe_2O_3 and Fe_3O_4 (Szatkowski *et al*., 2015). An additional vibrational modes in the range between 107-115 cm^{-1} were observed, but they cannot be ascribed to both α-Fe_2O_3 and Fe_3O_4 but they fall in the fingerprint region.

Table 4.4: Raman main vibrational modes of ClNCNTs unloaded and loaded with different metal salt loading of 10, 20, 30 and 53 wt.%.

Material		**Fe_3O_4/ClNCNTs 10 wt.%**	**Fe_3O_4/ClNCNTs 20 wt.%**	**Fe_3O_4/ClNCNTs 30 wt.%**	**Fe_3O_4/ClNCNTs 53 wt.%**
Vibration modes	**Phase**	**Wavenumber (cm^{-1})**			
*	*	115	107	111	107
A_{1g}	**α-Fe_2O_3**	221	229	227	226
E_g	**α-Fe_2O_3**	291	295	295	295
E_g	**α-Fe_2O_3**	418	410	410	405
A_{1g} & T_{2g}	**α-Fe_2O_3 & Fe_3O_4**	474	486	490	486
E_g	**α-Fe_2O_3**	604	616	612	612
E_g and A_{1g}	**α-Fe_2O_3 & Fe_3O_4**	-	643	-	643

* Fingerprint region

To further evaluate the crystallinity of the CNTs in terms of their defects density, the area of D- and G-bands were used in relation to their peak intensities to determine their intensity ratios (i.e. I_D/I_G). An increase in I_D/I_G ratio is attributed to material with high structural defects and/or disorders (Ferrari and Robertson, 2001; Ferrari and Robertson, 2004) (Mishra and Ramaprabhu, 2011). An increase in metal loading of Fe_3O_4, resulted in higher I_D/I_G values (Bakather *et al*., 2017). The I_D/I_G increased after addition of 10 wt.% metal loading and then decreased as more metal was loaded onto the ClNCNTs. This decrease can be attribited to less involvement of the iron oxide nanoparticles in disorder creation on the outerwalls of the CNTs as we increase the metal loading. An increase in I_D/I_G observed for a 30 wt.% metal loading could be attributed to experimental error that could have occurred during synthesis (Table 4.5).

Table 4.5: Summary of Raman data of the ClNCNTs un-loaded and loaded with Fe_3O_4 nanoparticles.

Sample	D-band	G-band	I_D/I_G
ClNCNTs	1323.3	1587.5	1.6
10 wt.%Fe_3O_4/ClNCNTs	132.5	1596.6	4.8
20 wt.%Fe_3O_4/ClNCNTs	1326.3	1595.0	3.6
30 wt.%Fe_3O_4/ClNCNTs	1326.6	1597.0	5.7
53 wt.%Fe_3O_4/ClNCNTs	1326.4	1595.4	3.5

4.3.4. XPS analysis of ClNCNTs and 20 wt.% Fe_3O_4/ClNCNTs

XPS analysis was performed in order to further quantify the amounts of atoms present in the synthesized materials. Figure 4.8 represent the survey spectra of both materials un-loaded and loaded with Fe_3O_4 nanoparticles. It is evident that the introduction of Fe_3O_4 nanoparticles to the structure of ClNCNTs has resulted in the reduction of carbon (97 to 86 %) but an increase in the amount of oxygen (1 to 8%). This could be due to the formation of a Fe-O-C bond. A wide scan XPS spectra revealed the presence of C1s, Cl2p, N1s and O1s peaks, with an additional Fe2p peak present from ClNCNTs loaded with Fe_3O_4 nanoparticles. However, the C12p spectra of ClNCNTs loaded with Fe_3O_4 nanoparticles could not be deconvoluted. In which it could be attributed to the masking of Cl2p, after the introduction of the Fe_3O_4 nanoparticles to the structural matrix of ClNCNTs.

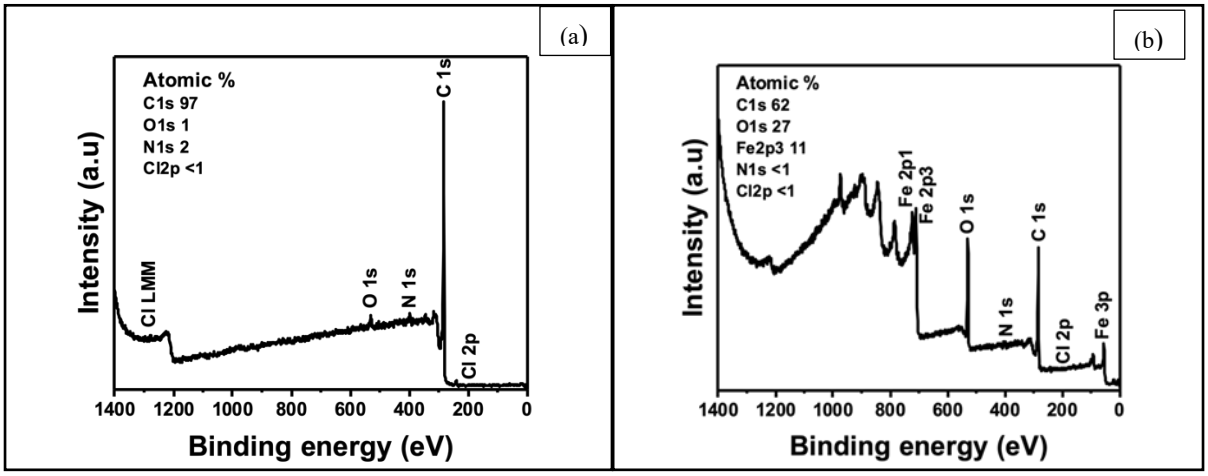

Figure 4.8: XPS survey scan of (a) ClNCNTs un-loaded and (b) loaded with 20 wt.% Fe_3O_4.

In the case of ClNCNTs un-loaded, the deconvoluted C1s peak gave rise to different types of carbon atoms that were hybridized differently (i.e., sp^2 and sp^3) suggesting different bonding

configurations as shown in Figure 4.9a (Pimenta *et al*., 2007). Three peaks were deconvoluted at around 285, 286.0 and 288.5 eV and were due to C-C sp^2, C-OH and C-Cl bonding configurations, respectively. The O1s spectrum un-loaded ClNCNTs has been resolved into three components at 531.9 eV(C–O), 535.7 eV(H_2O) and 533.8 eV (N=O), assigned to oxygen species in the carbonyl aliphatic, hydroxyl from water molecules, and nitrogen bonded to oxygen (Figure 4.9b). The N1s XPS spectra was deconvoluted into four peaks at 398.0, 398.5, 400.1 and 401.0 eV, assigned to pyridinic, pyrrolic, quaternary and oxygenated nitrogen, respectively (Figure 4.9c). Lastly, Figure 4.9d, shows the deconvoluted Cl2p peak that only revealed the presence of chloride ions Cl $2p_{3/2}$ with the peak appearing at 198 eV.

For ClNCNTs loaded with 20 wt.% Fe_3O_4, the C1s was deconvoluted into three peaks at 285.5, 286.5 and 288.5 eV corresponding to C-N/C-C, C=N/C-C and C-OH, respectively (Figure 4.10a). The O1s was deconvulated, to which four peaks were observed at ~530, 531.9, 532.5 and 534.5 eV assigned to oxygen species O^{2-}, C-O-C, O=C-O and C-OH, respectively, (Figure 4.10b). The deconvoluted O1s peak at 531.9 eV, is believed to arise due to the presence of R–O of FeO(OH) species (Barr, 1978). Furthermore, the Nls was deconvulated inot four peaks at 397.9 398.5, 400.1 and 401.0 eV, ascribed to pyridinic, pyrrolic, quaternary and oxygenated nitrogen, respectively (Figure 4.10c). Pyrrolic N also increased greatly in feeds containing Fe_3O_4, authors have suggested that pyrrolic N arises due to N substitution in a Stone-Wales defect (Gong *et al*., 2009; Shan and Cho, 2010) or due to asymmetric local bonding (Arenal *et al*., 2014). The presence of a lower amount of graphitic or quaternary peak suggests that the materials correlated with XRD, and Raman spectra. The high-resolution Fe2p spectrum for the loaded ClNCNTs (Figure 4.10d) showed two distinct peaks (Fe$2p_{3/2}$ and $2p_{1/2}$) located at 725.6 and 712 eV accompanied by a broad satellite peak. The spin energy separation of Fe$2p_{3/2}$ and Fe$2p_{1/2}$ is 13.6 eV, which indicates that Fe in the composite is Fe^{3+} and no other Fe^{2+} state was present (Armelao *et al*., 1995; Yamashita and Hayes, 2008). These peaks reveal the presence of Fe containing particles on the CNTs surfaces and it can also be suggested that the Fe_3O_4 attached themselves onto the CNTs by various configurations.

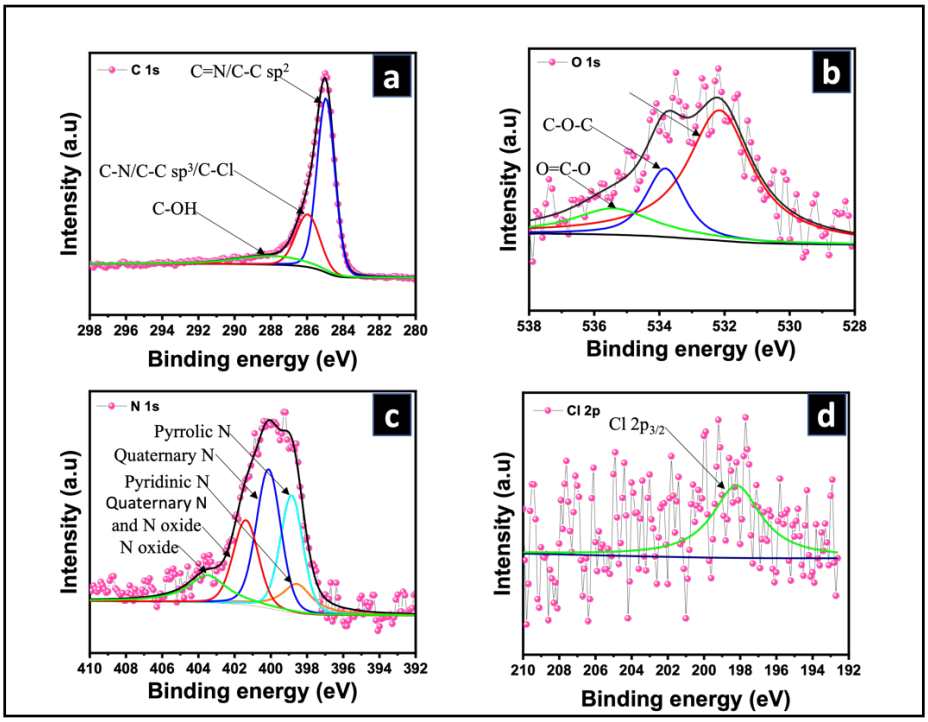

Figure 4.9: XPS survey scan of the deconvoluted spectra of ClNCNTs; (a) C1s, (b) O1s, (c) N1s, and (d) Cl2p.

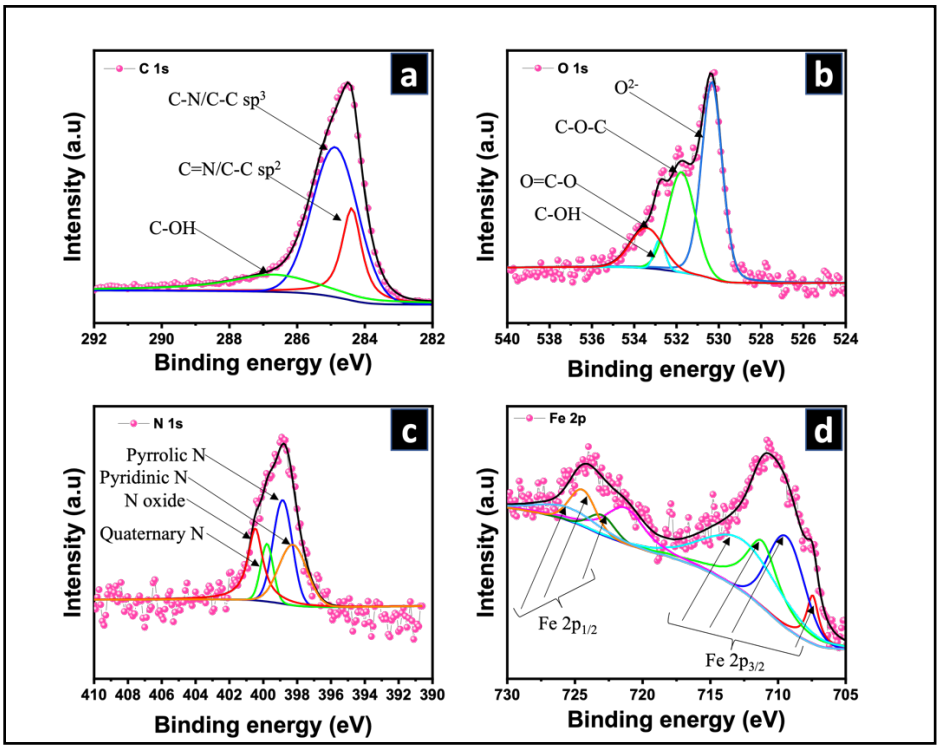

Figure 4.10:XPS survey scan of the deconvoluted spectra of Fe_3O_4/ClNCNTs; (a) C1s, (b) O1s, (c) N1s, and (d) Fe 2p.

4.4.4. Surface area and porosity analysis

The BET surface area analysis was conducted to measure the surface area, pore volume and pore size of the ClNCNTs un-loaded and loaded with Fe_3O_4 at different weight percentages (Table 4.6). The interpretation of the results was based on the adsorption-desorption of liquid N_2 at 77 K. The greater the enhancement of the surface area, the increase in the number of adsorption sites (Bakather *et al*., 2017). The BET surface area value obtained for ClNCNTs un-loaded was 37.1 m^2/g and for the Fe_3O_4 loaded samples were 38.2 m^2/g, 42.9 m^2/g, 40.4 m^2/g and 55.3 m^2/g for 10, 20, 30 and 53 wt.% Fe_3O_4 loadings respectively (see Table 4.6). Thus, the surface area increased with an increase in metal oxide loading. Intersitingly, the surface area of the 30 wt.% Fe_3O_4 loaded sample was a little lower than that of the 20 wt.% and 53 wt.%. The outlier in the surface area for materials loaded with 30 wt% confirms that there was indeed an experimental error that occurred during synthesis of this materials as a similar behaviour was oberved from the Raman data.

A large increase in the surface area for materials loaded with 53 wt.% is due to the large amounts of Fe_3O_4 nanoparticles present in this materials as we know they also posess large surface areas. Moreover, similar observation can be seen for pore volume and this can result in the adsorption capacity of the Fe_3O_4/ClNCNTs being higher (Bakather *et al*,. 2017). However, there might be a hindarance in the adsorption sites of the ClNCNTs if the high content loading is used as nano-adsorbents because of having a higher surface area, as they will be covered with Fe_3O_4. Thus, the adsorption sites contributing to the adsorption of metal ion will only be from Fe_3O_4. Therefore, it will be ideal to use the nano-adsorbent that can adsorp with both the adsorption sites from the ClNCNTs and Fe_3O_4; thus, when the 20 wt.% Fe_3O_4 based nanocomposite is used.

Table 4.6: Summary of BET data of the ClNCNTs un-loaded and loaded with Fe_3O_4 nanoparticles.

Material	BET surface area (m^2/g)	Pore volume (cm^3/g)	Pore diameter (nm)
ClNCNTs	37.1	0.19	21.6
Fe_3O_4/ClNCNTs (10 wt.%)	38.2	0.19	20.2
Fe_3O_4/ClNCNTs (20 wt.%)	42.9	0.27	24.9
Fe_3O_4/ClNCNTs (30 wt.%)	40.4	0.23	22.7
Fe_3O_4/ClNCNTs (53 wt.%)	55.3	0.30	20.8

The plots of adsorption and desorption nitrogen isotherms of ClNCNTs and Fe_3O_4/ClNCNTs prepared with different metal loading of Fe_3O_4; 10 wt.%, 20 wt.%, 30 wt.%, and 53 wt.% are depicted in Figure 4.11. All the hysteresis loops show a type four isothermal behaviour and this is due to the presence of the both mesopores and micropores (Huang *et al*., 2021). It is evident from the results obtained that there is a slight hysteresis at a high relative pressure, which might be attributed to capillary condensation (Farghali *et al*., 2017).

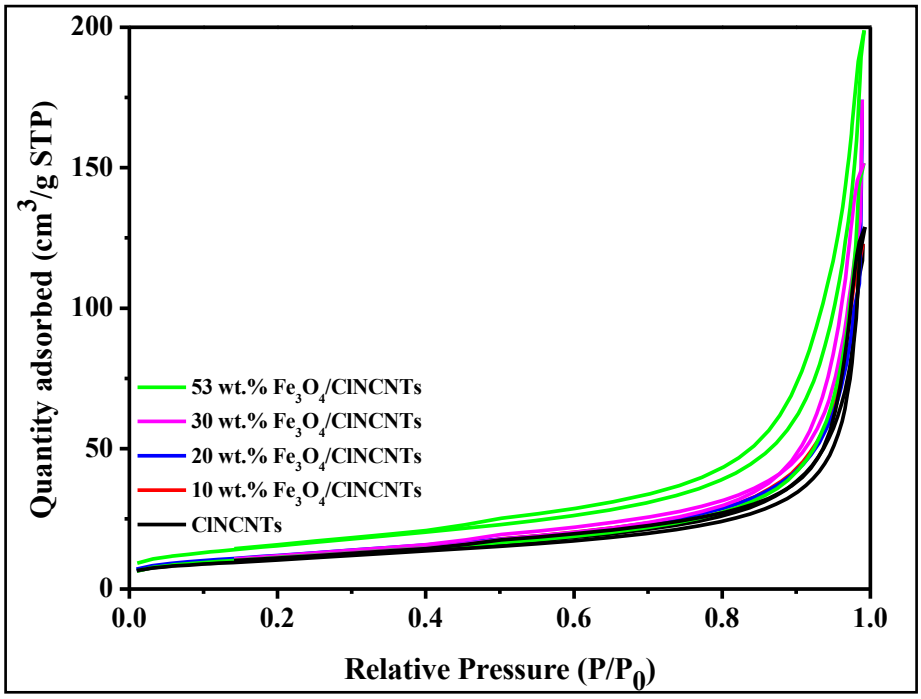

Figure 4.11: Plots of adsorption and desorption nitrogen isortherms for ClNCNTs and Fe_3O_4/ClNCNTs.

4.4.5. Thermal gravimetric analysis

The thermal stability and purity of the ClNCNTs un-loaded and loaded with Fe_3O_4 nanoparticles were also investigated. TGA was also used to characterise the iron oxide content in the nanocomposites. TGA profiles and derivative TGA (DTGA) curves are presented in Figure 4.12. ClNCNTs shows an obvious weight loss in the temperature range of 600 to 730 °C due to oxidation of carbon nanotubes. ClNCNTs materials loaded with Fe_3O_4 nanoparticles showed the weight loss at lower temperatures range of about 530–720 °C (Figure 4.12a), leaving iron oxide residue weight of about 13.4, 22.3, 26.0 and 44.8 % (for materials containing 10, 20, 30 and 53 wt.% iron oxide loadings respectively. It is evident that loading of the Fe_3O_4 nanoparticles resulted in the decrease of the decomposition temperature i.e., thermal stability (Figure 4.12b). This is attributed to the catalytic role of metal oxide nanoparticles in the oxidation of carbon materials (Li *et al*., 2007).

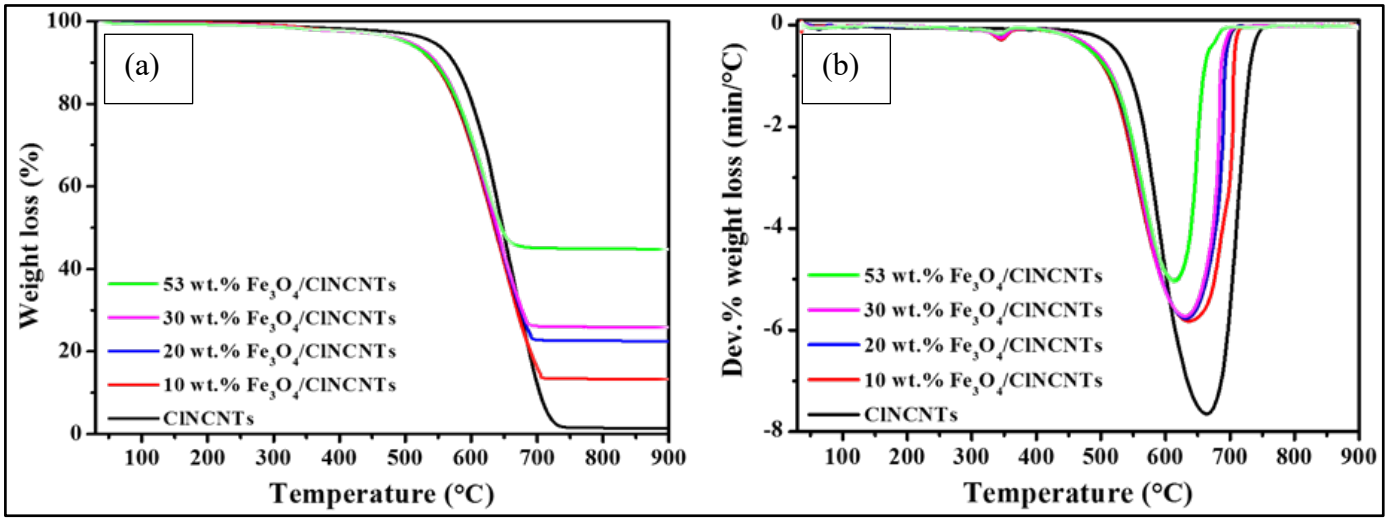

Figure 4.12:(a) TGA and (b) the corresponding derivative (DTGA) curves of the un-loaded and loaded ClNCNTs.

4.5. Conclusion

Synthesis of ClNCNTs and its surface modification with Fe_3O_4 nanoparticles was successfully achieved. Bamboo-compartmented and hollow CNTs were observed from nanotubes synthesized in the presence of chlorine and nitrogen. Loading of various amounts of iron salt to the ClNCNTs resulted in the formation of sphere-like Fe_3O_4 on the surface of the ClNCNTs as evidenced by TEM data. The identity of the nanoparticles was confirmed by powder-XRD and XPS as Fe_3O_4. Defects creation by co-addition of chlorine and nitrogen to the ClNCNTs

was evidenced by Raman spectroscopy. The optimum metal loading of Fe_3O_4 that achieved uniform, mono-dispersed nanoparticles distributed along the radial length of the ClNCNTs was from the nanocomposites containing 20 wt.%, since the aim was to utilize both the properties of Fe_3O_4 and ClNCNTs during adsorption. An increase in metal oxide loading from 30 and 53 wt.% resulted in agglomeration of Fe_3O_4 nanoparticles. Furthermore, for 10 wt.% metal loading nanoparticles were clumped, even though they were observed along the radial length of the CNTs. The surface area of the material increased with an increase in the amount of Fe_3O_4 used during metal loading. XPS data also confirmed the presence of different environments of nitrogen and also the presence of the inorganic chloride ion. Defects created at the walls of the ClNCNTs by chlorine and nitrogen enabled better attachment of Fe_3O_4 nanoparticles.

References

Abdalla, A.M., Ghosh, S., and Puri, I.K., 2016. Decorating carbon nanotubes with co-precipitated magnetite nanocrystals. *Diamond and Related Materials*, 66, 90–97.

Abdollah, S.M., Fereshteh, F., and Nazanin, F., 2017. Synthesis and modification of iron oxide nanoparticles (magnetite) for biomedical applications. *Research Journal of Biotechnology*, 12 (9), 87–95.

Amadou, J., Chizari, K., Houllé, M., Janowska, I., Ersen, O., Bégin, D., and Pham-Huu, C., 2008. N-doped carbon nanotubes for liquid-phase CC bond hydrogenation. *Catalysis Today*, 138 (1–2), 62–68.

Armelao, L., Bertoncello, R., Crociani, L., Depaoli, G., Granozzi, G., Tondello, E., and Bettinelli, M., 1995. XPS and UV–VIS study of high-purity Fe_2O_3 thin films obtained using the sol–gel technique. *Journal of Materials Chemistry*, 5 (1), 79–83.

Arenal, R., March, K., Ewels, C.P., Rocquefelte, X., Kociak, M., Loiseau, A., and Stéphan, O., 2014. Atomic Configuration of Nitrogen-Doped Single-Walled Carbon Nanotubes. *Nano Letters*, 14 (10), 5509–5516.

Bakather, O.Y., Kayvani Fard, A., Ihsanullah, Khraisheh, M., Nasser, M.S., and Atieh, M.A., 2017. Enhanced adsorption of selenium ions from aqueous solution using iron oxide impregnated carbon nanotubes. *Bioinorganic Chemistry and Applications*, 2017, 1–12.

Barr, T.L., 1978. An ECSA Study of the Termination of the Passivation of Elemental. *The Journal of Physical Chemistry*, 82 (16).

Daneshvar Tarigh, G. and Shemirani, F., 2013. Magnetic multi-wall carbon nanotube nanocomposite as an adsorbent for preconcentration and determination of lead (II) and manganese (II) in various matrices. *Talanta*, 115, 744–750.

Dong, C.K., Li, X., Zhang, Y., Qi, J.Y., and Yuan, Y.F., 2009. Fe_3O_4 nanoparticles decorated multi-walled carbon nanotubes and their sorption properties. *Chemical Research in Chinese Universities*, 25 (6), 936–940.

Elnabawy, H.M., Casanova-Chafer, J., Anis, B., Fedawy, M., Scardamaglia, M., Bittencourt, C., Khalil, A.S.G., Llobet, E., and Vilanova, X., 2019. Wet chemistry route for the decoration of carbon nanotubes with iron oxide nanoparticles for gas sensing. Beilstein *Journal of Nanotechnology*, 10 (1), 105–118.

Farghali, A.A., Abdel Tawab, H.A., Abdel Moaty, S.A., and Khaled, R., 2017. Functionalization of acidified multi-walled carbon nanotubes for removal of heavy metals in aqueous solutions. *Journal of Nanostructure in Chemistry*, 7 (2), 101–111.

Ferrari, A.C. and Robertson, J., 2001. Resonant Raman spectroscopy of disordered, amorphous, and diamondlike carbon. *Physical Review B*, 64 (7), 075414.

Ferrari, A.C. and Robertson, J., 2004. Raman spectroscopy of amorphous, nanostructured, diamond–like carbon, and nanodiamond. Philosophical Transactions of the Royal Society of London. Series A: *Mathematical, Physical and Engineering Sciences*, 362 (1824), 2477–2512.

Gong, K., Du, F., Xia, Z., Durstock, M., and Dai, L., 2009. Nitrogen-Doped Carbon Nanotube Arrays with High Electrocatalytic Activity for Oxygen Reduction. Science, 323 (5915), 760–764.

Gupta, V.K., Agarwal, S., and Saleh, T.A., 2011. Synthesis and characterization of alumina-coated carbon nanotubes and their application for lead removal. *Journal of Hazardous Materials*, 185 (1), 17–23.

Huang, L., Liu, L., Huang, W., Zhao, B., Shen, Z., Bao, Y., and Znad, H., 2021. Recovery of lanthanum cations by functionalized magnetic multi-walled carbon nanotube bundles. *RSC Advances*, 11 (8), 4751–4759.

Kayvani Fard, A., Rhadfi, T., Mckay, G., Al-marri, M., Abdala, A., Hilal, N., and Hussien, M.A., 2016. Enhancing oil removal from water using ferric oxide nanoparticles doped carbon nanotubes adsorbents. *Chemical Engineering Journal*, 293, 90–101.

Lambin, P., Loiseau, A., Culot, C., and Biro, L.P., 2002. Structure of carbon nanotubes probed by local and global probes, 40, 1635–1648.

Li, J., Tang, S., Lu, L., and Zeng, H.C., 2007. Preparation of Nanocomposites of Metals, Metal Oxides, and Carbon Nanotubes via Self-Assembly. *Journal of the American Chemical Society*, 129 (30), 9401–9409.

Mabena, L.F., Sinha Ray, S., Mhlanga, S.D., and Coville, N.J., 2011. Nitrogen-doped carbon nanotubes as a metal catalyst support. *Applied Nanoscience*, 1 (2), 67–77.

Maboya, W.K., 2018. Use of Chlorintaed Carbon Materials to make Nitrogen Doped and Un-doped Carbon Nanomaterials and their use in Water Treatment. Johannesburg.

Maboya, W.K., Coville, N.J., and Mhlanga, S.D., 2016. The synthesis of carbon nanomaterials using chlorinated hydrocarbons over a Fe-Co/$CaCO_3$ catalyst. *South African Journal of Chemistry*, 69 (July).

Maboya, W.K., Coville, N.J., and Mhlanga, S.D., 2021. Fabrication of chlorine nitrogen co-doped carbon nanomaterials by an injection catalytic vapor deposition method. *Materials Research Express*, 8 (1), 015007.

Maity, D., Ding, J., and Xue, J.-M., 2008. Synthesis of magnetite nanoparticles by thermal

decomposition: time, temperature, surfactant and solvent effects. *Functional Materials Letters*, 01 (03), 189–193.

Mallakpour, S. and Soltanian, S., 2016. Surface functionalization of carbon nanotubes: Fabrication and applications. *RSC Advances*, 6 (111), 109916–109935.

Masipa, P.M., Magadzu, T., and Mkhondo, B., 2013. Decoration of Multi-walled Carbon Nanotubes by Metal Nanoparticles and Metal Oxides using Chemical Evaporation.

Matei, E., Predescu, A., Vasile, E., and Predescu, A., 2011. Properties of magnetic iron oxides used as materials for wastewater treatment. *Journal of Physics*: *Conference Series*, 304 (1), 012022.

Mishra, A.K. and Ramaprabhu, S., 2011. Nano magnetite decorated multiwalled carbon nanotubes: A robust nanomaterial for enhanced carbon dioxide adsorption. *Energy and Environmental Science*, 4 (3), 889–895.

Mhlanga, S.D., Coville, N.J., Mondal, K.C., Carter, R., and Witcomb, M.J., 2009. The effect of synthesis parameters on the catalytic synthesis of multiwalled carbon nanotubes using Fe-Co/$CaCO_3$ catalysts. *South African Journal of Chemistry*, 62, 67–76.

Owens, F.J. and Orosz, J., 2006. Effect of nanosizing on lattice and magnon modes of hematite. *Solid State Communications*, 138 (2), 95–98.

Pimenta, M.A., Dresselhaus, G., Dresselhaus, M.S., Cançado, L.G., Jorio, A., and Saito, R., 2007. Studying disorder in graphite-based systems by Raman spectroscopy. *Physical Chemistry Chemical Physics*, 9 (11), 1276–1290.

Rahmawati, R., Melati, A., Taufiq, A., Sunaryono, Diantoro, M., Yuliarto, B., Suyatman, S., Nugraha, N., and Kurniadi, D., 2017. Preparation of MWCNT-Fe_3O_4 nanocomposites from iron sand using sonochemical route. *IOP Conference Series: Materials Science and Engineering*, 202 (1), 012013.

Ray, S.C., 2018. Nitrogenated carbon nanotubes functionalized with chlorine and oxygen: Electronic and magnetic properties for electronic/magnetic device applications. *Frontier Research Today*, 1, 1006.

Romero, A., Garrido, A., Nieto-Márquez, A., de la Osa, A.R., de Lucas, A., and Valverde, J.L., 2007. The influence of operating conditions on the growth of carbon nanofibers on carbon nanofiber-supported nickel catalysts. *Applied Catalysis A: General*, 319, 246–258.

Safari, J. and Zarnegar, Z., 2013. Biginelli reaction on Fe_3O_4–MWCNT nanocomposite: excellent reactivity and facile recyclability of the catalyst combined with ultrasound irradiation. *RSC Advances*, 3 (39), 17962.

Sathish, M., Tomai, T., and Honma, I., 2012. Graphene anchored with Fe_3O_4 nanoparticles as

anode for enhanced Li-ion storage. *Journal of Power Sources*, 217, 85–91.

Singh, C. and Song, W., 2001. Carbon nanotube structure, synthesis, and applications. In: K. Donaldson, C. Poland, R. Duffin, and J. Bonner, eds. *The Toxicology of Carbon Nanotubes*. Cambridge: Cambridge University Press, 1–37.

Shan, B. and Cho, K., 2010. Oxygen dissociation on nitrogen-doped single wall nanotube: A first-principles study. *Chemical Physics Letters*, 492 (1–3), 131–136.

Szatkowski, T., Wysokowski, M., Lota, G., Pęziak, D., Bazhenov, V. V., Nowaczyk, G., Walter, J., Molodtsov, S.L., Stöcker, H., Himcinschi, C., Petrenko, I., Stelling, A.L., Jurga, S., Jesionowski, T., and Ehrlich, H., 2015. Novel nanostructured hematite–spongin composite developed using an extreme biomimetic approach. *RSC Advances*, 5 (96), 79031–79040.

Tetana, Z.N., Mhlanga, S.D., Bepete, G., and Coville, N.J., 2012. The synthesis of nitrogen-doped multiwalled carbon nanotubes using an Fe-Co/$CaCO_3$ catalyst. *South African Journal of Chemistry*, 65, 39–49.

Yang, J., Hou, B., Wang, J., Tian, B., Bi, J., Wang, N., Li, X., and Huang, X., 2019. Nanomaterials for the removal of heavy metals from wastewater. *Nanomaterials*, 9 (3), 424.

Yamashita, T. and Hayes, P., 2008. Analysis of XPS spectra of Fe^{2+} and Fe^{3+} ions in oxide materials. *Applied Surface Science*, 254 (8), 2441–2449.

Yu, R., Jiang, C.-F., Chu, W., Ran, M.-F., and Sun, W.-J., 2017. Decoration of CNTs' surface by Fe_3O_4 nanoparticles: Influence of ultrasonication time on the magnetic and structural properties. *Chinese Chemical Letters*, 28 (2), 302–306.

Zhou, X., Fang, C., Li, Y., An, N., and Lei, W., 2016. Preparation and characterization of Fe_3O_4-CNTs magnetic nanocomposites for potential application in functional magnetic printing ink. *Composites Part B: Engineering*, 89, 295–302.

Zhou, Z., Gao, X., Yan, J., Song, D., and Morinaga, M., 2004. A first-principles study of lithium absorption in boron- or nitrogen-doped single-walled carbon nanotubes. *Carbon*, 42 (12–13), 2677–2682.

Zong, P. and Gou, J., 2014. Rapid and economical synthesis of magnetic multiwalled carbon nanotube/iron oxide composite and its application in preconcentration of U(VI). *Journal of Molecular Liquids*, 195, 92–98.

CHAPTER 5

Use of ClNCNTs and 20 wt.% Fe_3O_4/ClNCNTs-Based Nanocomposites as Nano-Adsorbents for Pb^{2+} Ions in Aqueous Solutions

5. Introduction

This chapter presents preliminary data on the use of ClNCNTs and 20 wt.% Fe_3O_4 loaded ClNCNTs as adsorbents for Pb^{2+} ions in aqueous solution.

5.1. Background

Lead (Pb) is used in everyday items such as batteries, toys, cabling, ammunition etc., (Ilac, 2012). Its versatile use is due to its properties such as resistance to acid, corrosion, low melting point, ductility, absorption of radiation, sound, and vibrations (Boldyrev, 2018). South Africa is amongst the leading Pb producers globally (U.S. Geological Survey, 2021). Although it is a useful metal, its exposure to human can result in brain damage, infertility, hearing loss, fatigue, among others (Panchangam, 2015). Exposure to lead can occur via ingestion, respiration and dermal (Tiwari *et al*., 2013; Panchangam, 2015). The World Health Organization (WHO) has classified Pb as one of the top ten global health metals of concern (WHO, 2021). Thus, there is a need to remove Pb from wastewater before discharging it into the water obtaining receiver. The permissible level of Pb in drinking water is below 0.05 mg/L (Sidhaarth and Jeyanthi, 2013).

Techniques for the removal of Pb from wastewater, include chemical precipitation, coagulation, reverse osmosis, and ion exchange. However, these techniques have drawbacks which include being expensive, results in inadequate removal of Pb and high consumption of energy (Barakat, 2011). To overcome some of the afore-mentioned drawbacks, a more favourable technique is adsorption. Adsorption employ a wide range of nano-adsorbents possessing an ideal surface area, thus providing better adsorption sites. These nano-adsorbents which include agricultural waste, carbon nanomaterials, metal oxides nanoparticles, activated carbon etc., have been efficiently utilized in tackling metal pollutants such as lead during wastewater treatment. These nano-adsorbents are ideal, since they possess properties such as high surface area, and are highly porous (Sidhaarth and Jeyanthi, 2013). To enhance the effectiveness of CNTs in the adsorption of Pb, and to increase their adsorption sites, surface modification of CNTs was found to be advantageous. It has been reported that surface

modification improves the performance of the nano-adsorbents (Manyangadze *et al*., 2020). Surface modification of CNTs can be achieved by loading their surface with metal oxides such as the magnetite (Fe_3O_4) nanoparticles for their beneficial use taking advantage of their magnetic properties that will aid in easier separation after post adsorption in addition to increased adsorption sites. Furthermore, addition of nitrogen and chlorine create defects that enhances their adsorption sites (Amadou *et al*., 2008; Ray, 2018). Hence, ClNCNTs and ClNCNTs loaded with 20 wt.% Fe_3O_4 are anticipated to be appropriate nano-adsorbents. A 20 wt.% Fe_3O_4 was chosen to be used since from its TEM image it exhibited uniform, mono-dispersed nanoparticles. Furthermore, the properties of both the CNTs and nanoparticles can contribute to the adsorption studies. To our knowledge, the use of ClNCNTs loaded and unloaded with Fe_3O_4 nanoparticles as nano-adsorbents for Pb^{2+} ions in aqueous solutions has never been documented. Hence, this study presents the exploration of ClNCNTs and 20 wt.% Fe_3O_4/ClNCNTs as potential nano-adsorbents for the removal of Pb^{2+} ions from aqueous solution. Several factors that affect the adsorption process will be evaluated which includes the effect of varying pH, mass of adsorbent, time, and concentration of adsorbate. In this study, the characterization of the adsorbent before adsorption including kinetic modelling and adsorption isotherms would be employed for purposes of understanding the adsorption process of lead by the prepared nanocomposites.

5.2. Experimental Procedures

5.2.1. Reagents

Lead acetate ($Pb(C_2H_3O_2)_2$), hydrochloric acid (HCl) and sodium hydroxide (NaOH), were purchased from Sigma Aldrich and employed without further purification. The stock solutions were prepared using ultra-pure water.

5.2.2. Batch adsorption experiments

5.2.2.1. Preparation of Pb stock solution

The stock solution of the Pb was prepared by weighing 1.57 g of lead acetate and adding it to a 1000 L volumetric flask, followed by dissolving it and filling the flask to the mark with ultrapure water, to achieve a 1000 mg/L concentrated Pb^{2+} ions solution. The appropriate concentrations needed for adsorption studies were prepared from the stock solution. Atomic adsorption spectroscopy (AAS) calibration standards were obtained using 5, 10, 15, 20 and 25 mg/L solutions prepared from the stock solution through serial dilutions.

5.2.2.2. Adsorption Experiments

The batch adsorption experiments of ClNCNTs were carried out at room temperature using 5-100 mg/L initial Pb^{2+} ions concentrations, by shaking them for 16 h at 200 rpm. Parameters such as pH, adsorbent dosage, initial Pb^{2+} ions solution concentration, and contact time were varied to establish the optimum conditions for removal of Pb^{2+} ions. Typically, a desired amount of ClNCNTs as adsorbent was mixed with the Pb^{2+} ions solution. About 1 mL of the aliquots were collected at various time intervals and were filtered through a 0.45 μm PVDF membrane. Thereafter, atomic absorption spectroscopy (AAS) was used to determine the final concentration of the aliquots. Similar conditions were applied when using a 20 wt.% Fe_3O_4/CINCNTs adsorbent; the shaking time used was 20 min. The adsorption capacity (mg/g) was calculated using Equation 5.1:

$$\boldsymbol{q_e = \frac{(C_i - C_{eq})V}{m}} \qquad \mathbf{5.1}$$

where q_e is the adsorption capacity (mg/g), C_i is the initial concentration and C_{eq} is the equilibrium concentration (mg/L), m is the mass of the adsorbent (g) and V is the volume of the solutions (L). The percentage metal ion removal (% MR) was be calculated as:

$$\% \boldsymbol{MR} = \left(\frac{\boldsymbol{C_i - C_{eq}}}{\boldsymbol{C_i}}\right) \boldsymbol{X\ 100} \qquad \mathbf{5.2}$$

where C_i is the initial concentration of adsorbate (mg/L) and C_{eq} is the equilibrium concentration of adsorbate (mg/L).

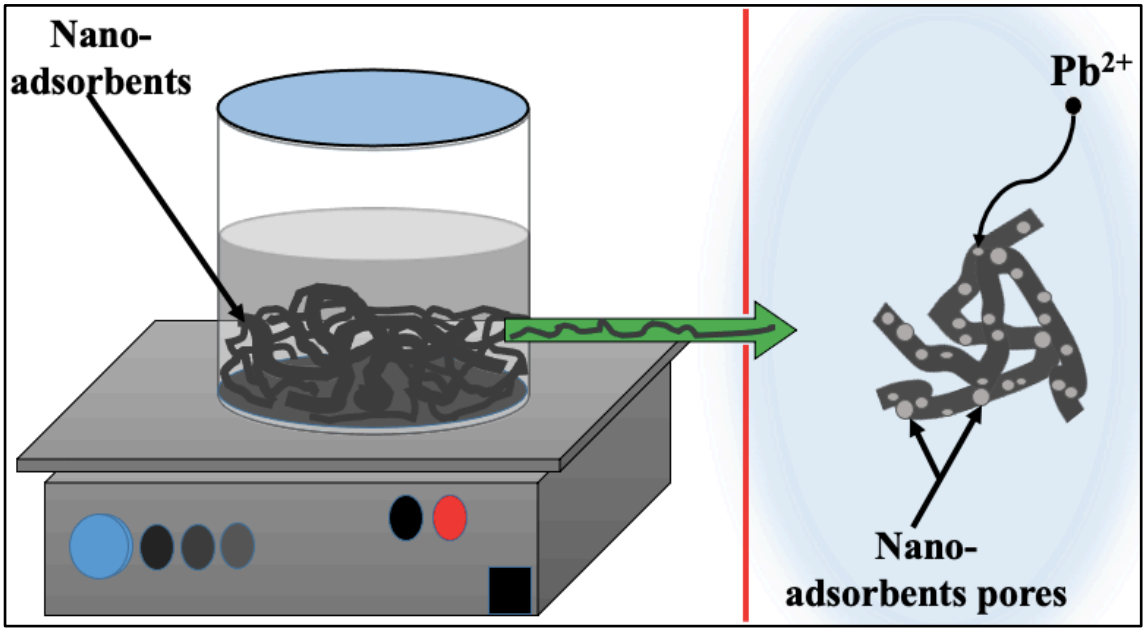

Figure 5.1: Schematic representation of adsorption batch studies.

5.2.2.2.1 Adsorption kinetics

The kinetics of the experimental data were determined using pseudo-first-order (PFO), and pseudo-second-order (PSO) adsorption models and intraparticle diffusion (IPD); was calculated manually and also using the Ky plot software.

5.2.2.2.1.1 Pseudo-first order model

The Lagergren pseudo-first-order model proposes that the rate of adsorption is proportional to the number of sites unoccupied by the adsorbate (Ho, 2004). The pseudo-first-order equation can be written in a non-linear (Equation 5.3) and linear (Equation 5.4) equations as follows:

$$q_t = q_e(1 - e^{-tk1}) \qquad 5.3$$

$$\log(q_e - q_t) = \frac{k_1}{2,303} + \log(q_e) \qquad 5.4$$

where q_t is the adsorption capacity (mg/g) at any present time interval (t), q_e is the adsorption capacity at equilibrium and k_1 is the pseudo-first-order rate constant (1/min).

5.2.2.2.1.2 Pseudo-second order model

The adsorption data can be analysed using the pseudo-second-order kinetic model (Ho and Mckay, 1999). The pseudo-second-order kinetic model can be written in a non-linear (Equation 5.5) and linear (Equation 5.6) as follows:

$$\mathbf{q_t = \frac{q_e^2 k_2}{1 + k_2 q_e t}} \qquad \mathbf{5.5}$$

$$\mathbf{\log(q_e - q_t) = \frac{k_1}{2,303} + \log(q_e)} \qquad \mathbf{5.6}$$

where q_t is the adsorption capacity (mg/g) at any present time interval (t), q_e is adsorption capacity at equilibrium and k_1 is the pseudo-second order rate constant (min^{-1}). The parameters q_e, k_2 and h were obtained from the slope and intercept of the t/q_t versus time. In which the initial adsorption rate was calculated from the equation below:

$$\mathbf{h = k_2 q_e^2} \qquad \mathbf{5.7}$$

where h is the initial adsorption rate (mg/g/min), q_e is adsorption capacity at equilibrium and k_2 is the second-order rate constant (g/mg min).

5.2.2.2.1.3 Intraparticle diffusion

To have a better understanding of the mechanism and rate-controlling step that affect the kinetics of adsorption, the results of the experiments can be fitted to the Weber-Morris intraparticle diffusion (IPD) model which is commonly expressed by the equation (Weber and Morris, 1963):

$$\mathbf{q_t = k_p \sqrt{t} + C} \qquad \mathbf{5.8}$$

where k_p is the intraparticle diffusion rate constant ($mg/g.min^{1/2}$), C is the intercept (mg/g).

5.2.2.2.2 Adsorption isotherms

The adsorption isotherms are significant as they give data about the adsorption capacity and how the adsorbate cooperates with the adsorbents, which are basic in optimizing the use of an

adsorbent. Herein, Langmuir and Freundlich models were employed to determine the best descriptor of the study. They were calculated manually and also with Ky plot software.

5.2.2.2.2.1. Langmuir isotherm model

The Langmuir isotherm is projected to describe the gas-solid phase, which assumes monolayer adsorption on a uniform surface with the same affinity and has no lateral interaction. This isotherm is governed by Equation 5.9 non-linear and Equation 5.10 linear below.

$$\mathbf{q_e = \frac{Q^o_{max}\, K_L\, C_e}{1 + K_L\, C_e}} \qquad \mathbf{5.9}$$

$$\mathbf{\frac{C_e}{q_e} = \left(\frac{1}{Q^o_{max}}\right) C_e + \frac{1}{Q^o_{max}\, K_L}} \qquad \mathbf{5.10}$$

where C_e is a concentration of the adsorbate at equilibrium (mg/g), q_e is the quantity or maximum adsorption capacity (mg/g), q_m is the amount adsorbed (mg/g). K_f is the Langmuir constant related to the energy of the adsorption. The crucial characteristic of the Langmuir isotherm can be achieved by a constant called equilibrium parameter or separation factor (R_L) calculated by Equation 5.11:

$$\mathbf{R_L = \frac{1}{1 + K_L\, C_o}} \qquad \mathbf{5.11}$$

where, K_L is the Langmuir constant (mg/g), C_o is initial concentration of initial adsorbate (mg/g), R_l lies within 0 and 1 when adsorption is favourable: when R_L >1- unfavourable, R_L =1- linear, R_L =0 - irreversible and R_L <1- favourable.

5.2.2.2.2.2. Freundlich isotherm model

The Freundlich model is an observational relationship depicting the uptake of adsorbate particles on a heterogeneous surface. The model assumes multi-layer adsorption and accepts the existence of various sites with different energies on the surface of the adsorbent. This isotherm is governed by Equation 5.12 non-linear and Equation 5.13 linear below.

$$\mathbf{q_e = K_F C_e^n} \qquad \mathbf{5.12}$$

$$\log q_e = n \log C_e + \log K_f \quad \textbf{5.13}$$

where, K_f is a constant adsorption capacity (L/mg), q_e is the concentration at equilibrium (mg/L), C_e is the equilibrium concentration (mg/L), n is a constant adsorption intensity. Furthermore, to determine the best-suited model, the chi-squared χ^2 of the experimental data can be calculated using the equation:

$$\chi^2 = \frac{(q_{e,exp} - q_{e,calc})^2}{q_{e,exp}} \quad \textbf{5.14}$$

where, $q_{e,exp}$ and $q_{e,calc}$ (mg/g) are the amount of adsorbate uptake at equilibrium and achieved, respectively. In which the χ^2 value that is close to zero or 1 is best fitted to the model.

5.3. Results and Discussions

5.3.1. Adsorption studies

5.3.1.1. Effect of pH solution

pH of the solution plays a vital role in the adsorption of metal ions, as it affects the surface bonding sites of the adsorbent (Abdel Salam *et al*., 2020; Sarı and Tuzen, 2008). The effect of pH was investigated using ClNCNTs nano-adsorbents. Figure 5.2 depicts the experimental data for the effect of pH (2-6). Based on the data, it is evident that at pH 2, there is minimal adsorption capacity of Pb^{2+} ions due to the presence of H^+ ions which are competing with metal (Pb^{2+}) ions for binding sites (Sarı and Tuzen, 2008). However, at pH (3-5) there was a slight but significant increase in the adsorption capacity of nanocomposite for Pb^{2+} ions, which could be due to lesser competition between the protons and metal species (Morris, 1991). When the pH was increased to 6, there was a slight decrease in the adsorption capacity due to hydroxyl ions becoming predominant, leading to the precipitation of lead hydroxides in solution (Hamza *et al*., 2013). The 20 wt.% Fe_3O_4/ClNCNTs was also investigated under similar conditions in which similar trend was also observed. In addition, it was evident that the 20 wt.% Fe_3O_4/CINCNTs had a higher adsorption capacity in comparison to ClNCNTs. This can be attributed to a higher surface area (42.9 cm^3/g) providing more binding sites for Pb^{2+}ions while for ClNCNTs the surface area was 37.1 cm^3/g (Chapter 4, section 4.4.4. for BET data). pH values higher than 6 were not investigated, to prevent the hydrolysis and precipitation of Pb^{2+} ions. Therefore, the chosen optimum pH value was pH 5.

The point of zero charge (pH_{PZC}) value was established by using a plot that shows the change in pH against initial pH (supplementary Figure S3). The pH_{PZC} was 4.19 and 4.23 for ClNCNTs and 20 wt.% Fe_3O_4/CINCNTs loaded CNTs nano-adsorbents, respectively. This suggests that below these values the surface will be positively charged while above this values the surface will be negatively charged (Oyetade *et al*., 2017). It is an indication that there was an electrostatic attraction between the Pb^{2+} ions and adsorbents at pH 5. In addition, it was reported that the increase in pH changes the charge of the adsorbent to become negative; thus, electrostatic interactions are favourable for the cation adsorption, as the H^+ ions are decreasing (Hamza *et al*., 2013).

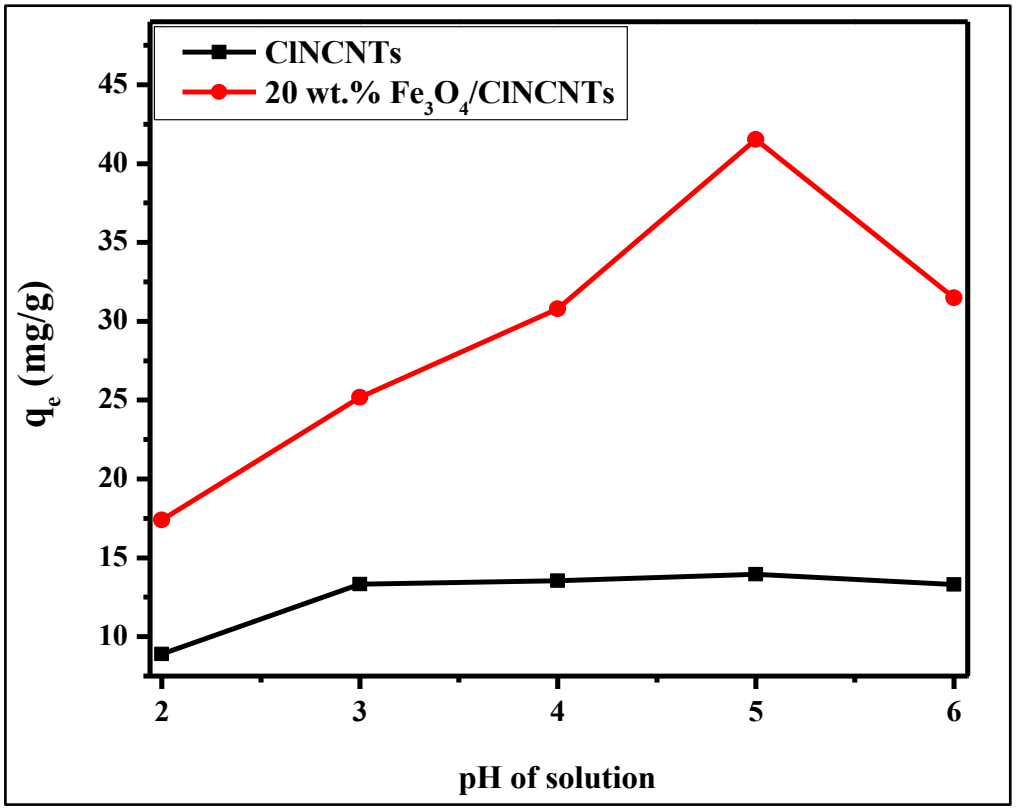

Figure 5.2: Effect of initial pH on Pb^{2+} ions removal using ClNCNTs and 20 wt.% Fe_3O_4/CINCNTs (initial concentration: 100 mg/L, adsorbent mass: 0.05 g, contact time = 16 h, shaking speed: 200 rpm and temperature: 298 K).

5.3.1.2. Effect of adsorbent mass

The effect of adsorbent mass (0.01 to 0.05 g) for the removal of Pb^{2+} ions was evaluated using ClNCNTs while the other parameters were kept constant. As shown in Figure 5.3, an increase in the mass of the adsorbent resulted in an increase in the removal efficiency of the Pb^{2+} ions. This was attributed to an increase in the adsorption sites as the mass of the adsorbent increased. At 0.05 g mass of ClNCNTs a maximum removal efficiency of 70 % was achieved. The 20 wt.% Fe_3O_4/CINCNTs was also investigated under similar conditions and 76 % maximum removal efficiency was obtained. The higher removal efficiency of a 20 wt.% Fe_3O_4/CINCNTs, compared to ClNCNTs, was attributed to a higher surface area (42.9 cm^3/g) which provided more adsorption sites. The concentration of the Pb^{2+} ions in solution was reduced with an increase in the mass of the nano-adsorbents, as more sites were available for adsorption (Oyetade *et al*., 2017).

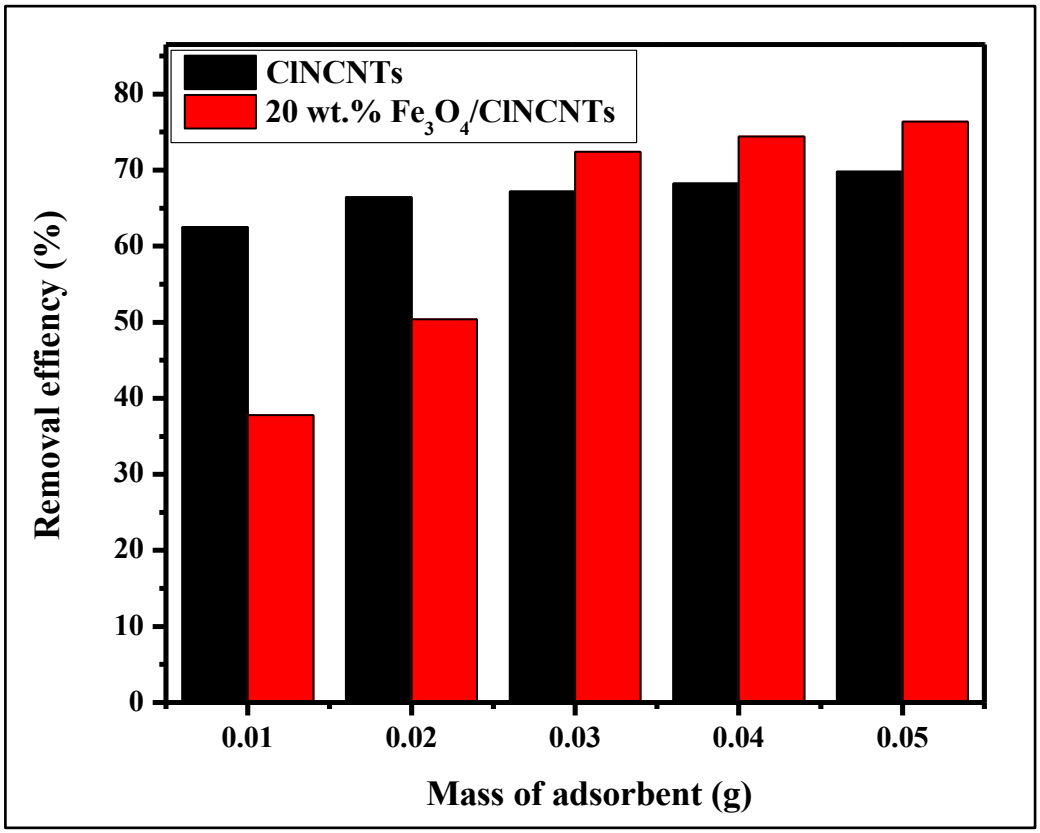

Figure 5.3: Effect of dosage mass of un-loaded ClNCNTs and 20 wt.% Fe_3O_4/CINCNTs loaded ClNCNTs (0.01 to 0.05 g) on Pb^{2+} ions removal (initial concentration: 100 mg/L, contact time = 16 h, shaking speed: 200 rpm, pH: 5, and temperature: 298 K).

5.3.1.3. Effect of initial concentration

The initial concentration of the adsorbate plays a vital role, as a given mass of the nano-adsorbent can adsorb a fixed quantity of the solute (Adegoke *et al*., 2017). The effect of initial concentration (5 to 100 mg/L) for the removal of Pb^{2+} ions using ClNCNTs was varied, while the other parameters were kept constant. As shown in Figure 5.4, the adsorption capacity of Pb^{2+} ions increased with an increase in the initial concentration from 5 mg/L to 100 mg/L. This was attributed to strong driving forces at higher concentrations, that allows for the Pb^{2+} ions to move towards the available binding sites (Hamza *et al*.,2013; Rahimnejad *et al*., 2018). The 20 wt.% Fe_3O_4/CINCNTs nanoadsorbents was also investigated under similar conditions. In the case of a 20 wt.% Fe_3O_4/CINCNTs, similar trend was also observed. The adsorption capacities at low concentrations (5 to 25 mg/L) were lower which might be attributed to repulsion between the adsorbent and adsorbate, as both had positive charges. At higher concentrations (50 mg/L to 100 mg/L), it is evident that the adsorption capacity was higher, although the adsorption capacity was still higher for 20 wt.% Fe_3O_4/CINCNTs. This was attributed to availability of abundant vacant adsorption sites on the surface of the adsorbents as it had a larger surface area.

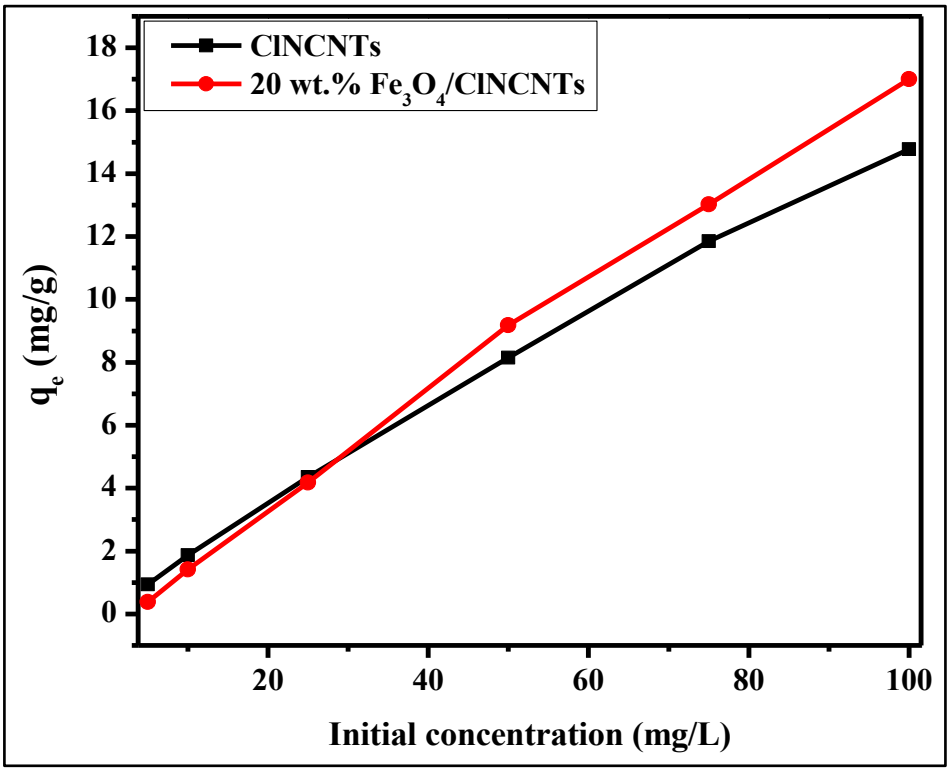

Figure 5.4: Effect of initial Pb^{2+} ions concentration on the adsorption capacity over ClNCNTs and 20 wt.% Fe_3O_4/CINCNTs (adsorbent mass: 0.05 g, time: 16 h, shaking speed: 200 rpm, pH: 5 and temperature: 298 K).

5.3.1.4. Effect of contact time

The effect of contact time was investigated over a period of 5 to 1440 minutes using ClNCNTs while varying the initial concentration from 5 to 100 mg/L. It was evident that the increase in initial concentration resulted in an increase in the adsorption capacity. This was attributed to strong driving forces at higher concentrations, that allowed for the Pb^{2+} ions to move towards the available binding sites (Hamza *et al*., 2013). The process of adsorption happened in three stages: in the first stage, the Pb^{2+} ions were adsorbed rapidly; then in the second stage the adsorption process was slower and lastly saturation was reached at around 30 min.

It can be seen from Figure 5.5 that the adsorbent adsorbed more Pb^{2+} ions when initial concentrations were higher. This could be due to available adsorption sites on the adsorbent material and the affinity of the adsorbent material towards Pb^{2+} ions. Also, metal removal increased with an increase in contact time for various studied concentrations of Pb^{2+} ions. The amount of sorbent metal ion on the particles increased rapidly during the initial stages and then progressively reached equilibrium. The high removal rate at the beginning of the contact time was due to the large number of vacant binding sites available for the adsorption of Pb^{2+} ions. At high contact times the outer surface of the adsorbent became exhausted and saturated with metal ions, which caused the rate of metal ion uptake to decrease and reach equilibrium. The trend was observed for both adsorbents used in the study.

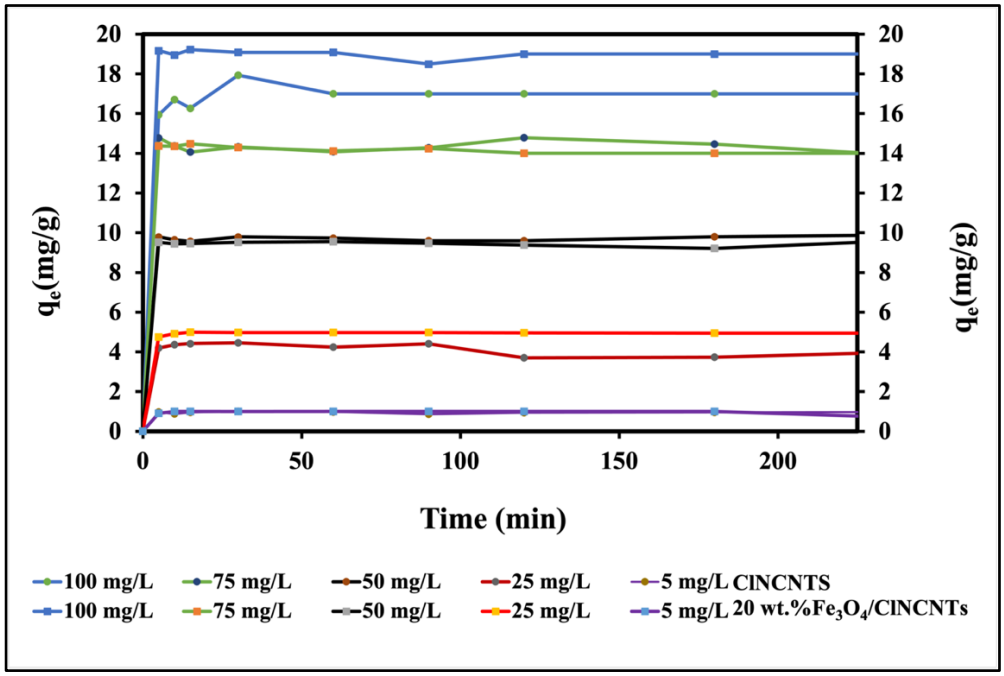

Figure 5.5: Effect of contact time on Pb^{2+} ions uptake onto ClNCNTs and 20 wt.% Fe_3O_4/ClNCNTs, respectively with different solution concentrations of 5 to 100 mg/L (pH: 5, adsorbent mass: 0.05 g, shaking speed: 200 rpm and temperature: 298 K

5.3.2. Kinetic studies

The kinetics adsorption variables such as the rate constant and equilibrium adsorption capacities are vital for understanding the adsorption processes. The pseudo-first order (PFO), pseudo-second order (PSO) and intra-particle diffusion (IPID) kinetic models were used to determine the best model that will best fit the experimental data. The calculated kinetic parameters attained from the experimental data (ClNCNTs) best fitted the PSO. In which, the coefficient correlation (R^2) values of the PSO model were greater than 0.999 while the calculated and experimental equilibrium adsorption capacity were in good agreement. Based on these data, it showed that the PSO model was more appropriate to describe the kinetic adsorption process. The chi-squared (χ^2) values were closer to zero suggesting favourable adsorption of Pb^{2+} ions on the surface of both the nano-adsorbents. Furthermore, the rate constants of ClNCNTs (k_2) values derived from PSO decreased with an increase in the initial concentration similar to what was observed by Bullen *et al*., 2021 and Lazaridis *et al*., 2004. The experimental data obtained using a 20 wt.% Fe_3O_4/CINCNTs nano-adsorbents was also fitted to adsorption kinetics models under similar conditions Table 5.2. Their experimental data was also best fitted to PSO model with similar observations. Both the data poorly fitted the IPID model, this might have been attributed to the adsorption process being chemisorption.

Table 5.1: The experimental data of kinetics adsorption model of ClNCNTs.

Kinetic model of the ClNCNTs		**The initial concentration of Pb^{2+} ions solution mg/L**				
		5	**25**	**50**	**75**	**100**
Pseudo-first-order	**R^2**	0.4723	0.0102	0.0978	0.1551	0.066
	χ^2	2.7	6.7	18.8	1117.4	
	k_1 (g/mg/min)	0.00052969	0.00004606	0.0002303	0.0000216	0.013818
	$q_{e,exp}$ (mg/g)	0.9	4.0	9.7	15	17
	$q_{e,calc}$ (mg/g)	3.9	1.2	2.6	1.5	1.9
Pseudo-second-order	**R^2**	0.999	0.999	0.999	0.999	1
	χ^2	0.00010989	0.000063745	0.0000924974	0.00000374813	0.0000002
	k_2 (g/mg/min)	0.0803	0.0379	0.0933	0.0078	0.6523
	$q_{e,exp}$ (mg/g)	0.9	4.0	9.7	15.0	17
	$q_{e,calc}$ (mg/g)	0.9	4.0	9.7	15.0	17.0
	h(mg/g/min)	0.066	0.602	8.834	1.775	7.237
Intra-particle diffusion	**R^2**	0.4025	0.7965	0,1014	0.6140	0.4000
	k_p (mg/g x $min^{1/2}$)	-0.0073	-0.0916	0.0398	-0.092	0.008733
	C	0.976	4.56	9.70	14.71	16.47

Table 5.2: The experimental data of kinetics adsorption model of 20 wt.% Fe_3O_4/CINCNTs

Kinetic model of 20 wt.% Fe_3O_4/CINCNTs		Initial concentration of Pb^{2+} ions solution mg/L				
		5	**25**	**50**	**75**	**100**
Pseudo-first-order	**R^2**	0.0604	0.1524	0.7256	0.7091	0.0124
	χ^2	16.24388887	1	1.81868206	340.112701	9.46485138
	k_1 (g/mg/min)	0.125969875	0.0059878	0.0094423	0.0025333	0.001381
	$q_{e,exp}$ (mg/g)	0.9	4.9	9.6	14.0	19
	$q_{e,calc}$ (mg/g)	0.8	1.3	13.8	83.0	5.6
Pseudo-second-order	**R^2**	0.948	1.0	0.999	1.0	0.9999
	χ^2	0.055255384	0.0004428	0.00153336	0,000080254	0.0000320026
	k_2 (g/mg/min)	0.1260	2.0280	0.4562	0.1324	0.1653
	$q_{e,exp}$ (mg/g)	0.9	4.9	9.6	14.0	19.0
	$q_{e,calc}$ (mg/g)	0.8	4.9	9.5	13.9	18.9
	h(mg/g/min)	0.0121	20.37	1.9723	0.2451	0.5185
Intra-particle diffusion	**R^2**	0.3907	0.4870	0.2054	0.9062	0.3754
	k_p (mg/g x $min^{1/2}$)	-0.0469	0.0431	-0.0271	-0.0271	-0.0912
	C (mg/g)	1.083	9.5397	9.5397	14.73	19.25

5.3.3. Isotherm studies

The Langmuir and Freundlich models were used to investigate the adsorption processes occurring between the adsorbate ions and the nano-adsorbents using equations 5.10 and 5.12 respectively for adsorbent ClNCNTs. The calculated isotherm parameters obtained from the adsorption isotherm are depicted in Table 5.3. The correlation coefficient (R^2) and equilibrium adsorption capacity calculated from the Freundlich and Langmuir models were found to be 0.995 and 203.4 mg/g and 0.983 and 14.8 mg/g, respectively for ClNCNTs. Their calculated and experimental equilibrium adsorption capacities were in good agreement as compared to those obtained from the Freundlich model (Table 5.3**)**. In addition, the value of chi-squared (χ^2) calculated from the Langmuir model was lower as compared to that of the Freundlich model. These data indicate that the Langmuir model was more suitable to describe the adsorption process. This indicates a monolayer coverage by Pb^{2+} ions occurring on a homogeneous surface of the ClNCNTs as nano-adsorbent, with no interaction between the neighbouring adsorbates. The experimental data of 20 wt.% Fe_3O_4/CINCNTs was also fitted to adsorption isotherm models under similar conditions (Table 5.3). In the case of loaded, the calculated isotherm parameters attained from the experimental data of 20 wt.%

Fe_3O_4/CINCNTs best fitted to Freundlich model. The calculated adsorption capacity was in close agreement with experimental adsorption capacity. This indicates that there was a multi-layer coverage by Pb^{2+} ions occurring on a heterogenous surface of the 20 wt.% Fe_3O_4/CINCNTs nano-adsorbents.

The equilibrium parameter or separation factor (R_L values) for the Langmuir model was calculated to explain the interaction between adsorbate–adsorbent, which are shown in Table 5.4. For ClNCNTs, the Langmuir separation factor (R_L values) for 5, 10, 25, 50, 75 and 100 mg/L Pb^{2+} ions were 0.1981, 0.1099, 0.0471, 0.0241, 0.0162 and 0.0122, respectively. These values are closer to 0 which indicates that the adsorption process was favourable. Furthermore, the R_L values decreased with an increase in the initial concentration which suggests chemisorption occurring between the adsorbate and adsorbent (Ntuli and Pakade, 2020).

Table 5.3: The experimental data of Langmuir isotherms adsorption model of ClNCNTs and 20 wt.% Fe_3O_4/CINCNTs.

Materials	Langmuir Isotherm model				Freundlich Isotherm model				
	R^2	χ^2	$q_{e,exp}$ (mg/g)	Q^o_{max} (mg/g)	R^2	χ^2	$q_{e,exp}$ (mg/g)	Q^o_{max} (mg/g)	n
ClNCNTs	0.983	27.1	14.8	23.93	0.995	423.2	14.8	203.4	1.7
20 wt.% Fe_3O_4/CINCNTs	0.964	0.787	17	150.3	0.963	0.025	17	20.2	1.0

Table 5.4: Langmuir equilibrium parameter or separation factor values of ClNCNTs and 20 wt.% Fe_3O_4/CINCNTs attained for different initial concentrations.

Initial concentration of Pb^{2+} mg/L	R_L values Un-loaded CNTs	R_L values Loaded CNTs
5	0.1981	0.6939
10	0.1099	0.5312
25	0.0471	0.3119
50	0.0241	0.1848
75	0.0162	0.1313
100	0.0122	0.1018

5.4. Conclusions

The ClNCNTs and ClNCNTs loaded with 20 wt.% Fe_3O_4 nanoparticles were employed as nano-adsorbents for the removal of Pb^{2+} ions in aqueous solution using a batch adsorption method. The maximum adsorption efficiency of Pb^{2+} ions removal was 70 % and 76 % for un-loaded and loaded ClNCNTs, which was attributed to increased surface area that was obtained

after loading with Fe_3O_4 nanoparticles. The 6 % difference in the removal efficiency, was not significant; however, the loading of Fe_3O_4 nanoparticles can enable the easy recovery of the nano-adsorbents to be reused utilizing its magnetic properties. The correlation coefficient was (R^2 =0.999) for both ClNCNTs and 20 wt.% Fe_3O_4/CINCNTs and while the chi-squares' were (χ^2 = 0.65230; 0.1653) respectively, indicating that the best fitted model was PSO model. This is an indication that this nano-adsorbents are suitable for the removal of Pb^{2+} ions of variable concentrations in water. The equilibrium data was also fitted using Langmuir and Freundlich adsorption isotherms. In which the correlation coefficient (R^2 = 0.963) and chi-squared (χ^2 = 27.1) showed that the Langmuir isotherm model best fitted the experimental data of ClNCNTs. In the case of 20 wt.% Fe_3O_4/CINCNTs, the experimental data best fitted Freundlich isotherm model. Their correlation coefficient was R^2 = 0.98) and whilst the chi-squared was χ^2= 0.025.

References

Abdel Salam, E.T., Abou El-Nour, K.M., Awad, A.A., and Orabi, A.S., 2020. Carbon nanotubes modified with 5,7-dinitro-8-quinolinol as a potentially applicable tool for efficient removal of industrial wastewater pollutants. *Arabian Journal of Chemistry*, 13 (1), 109–119.

Adegoke, H.I., Adekola, F.A., Olowookere, I.T., and Yaqub, A.L., 2017. Thermodynamic studies on adsorption of lead (II) Ion from aqueous solution using magnetite, activated carbon and composites. *Journal of Applied Sciences and Environmental Management*, 21 (3), 440.

Amadou, J., Chizari, K., Houllé, M., Janowska, I., Ersen, O., Bégin, D., and Pham-Huu, C., 2008. N-doped carbon nanotubes for liquid-phase CC bond hydrogenation. *Catalysis Today*, 138 (1–2), 62–68.

Barakat, M.A., 2011. New trends in removing heavy metals from industrial wastewater. *Arabian Journal of Chemistry*, 4 (4), 361–377.

Boldyrev, M., 2018. Lead: properties, history, and applications. *WikiJournal of Science*, 1 (2), 7.

Bullen, J.C., Saleesongsom, S., Gallagher, K., and Weiss, D.J., 2021. A Revised Pseudo-Second-Order Kinetic Model for Adsorption, Sensitive to Changes in Adsorbate and Adsorbent Concentrations. *Langmuir*, 37 (10), 3189–3201.

Daneshvar Tarigh, G. and Shemirani, F., 2013. Magnetic multi-wall carbon nanotube nanocomposite as an adsorbent for preconcentration and determination of lead (II) and manganese (II) in various matrices. *Talanta*, 115, 744–750.

Elkhaleefa, A., Ali, I.H., Brima, E.I., Shigidi, I., Elhag, A.B., and Karama, B., 2021. Evaluation of the adsorption efficiency on the removal of lead(II) ions from aqueous solutions using Azadirachta indica leaves as an adsorbent. *Processes*, 9 (3).

Hamza, I.A.A., Martincigh, B.S., Ngila, J.C., and Nyamori, V.O., 2013. Adsorption studies of aqueous Pb(II) onto a sugarcane bagasse/multi-walled carbon nanotube composite. *Physics and Chemistry of the Earth, Parts A/B/C*, 66, 157–166.

Ho, Y.S., 2004. Citation Review of Lagergren Kinetic Rate Equation on Adsorption Reactions. *Scientometrics*, 59 (1), 171–177.

Ho, Y.S. and Mckay, G., 1999. Pseudo-second order model for sorption.pdf, 34, 451–465.

ILA, 2012. Lead Production & Statistics < Lead Facts | ILA - International Lead Association Website [online]. Available from: https://www.ila-lead.org/lead-facts/lead-uses--statistics [Accessed 27 Feb 2020].

Kabbashi, N.A., Atieh, M.A., Al-Mamun, A., Mirghami, M.E., Alam, M.D.Z., and Yahya, N., 2009. Kinetic adsorption of application of carbon nanotubes for Pb(II) removal from aqueous solution. *Journal of Environmental Sciences*, 21 (4), 539–544.

Khichi, D.S., Bhati, S., and Gupta, A., 2011. Adsorption of methylene blue dye by using chemically activated low cost adsorbent : Azadirecta indica leaves. *Inventi Rapid: Water & Environment*, 2011 (3), 13–15.

Kosa, S.A., Al-zhrani, G., and Abdel, M., 2012. Removal of heavy metals from aqueous solutions by multi-walled carbon nanotubes modified with 8-hydroxyquinoline. *Chemical Engineering Journal*, 181–182, 159–168.

Lazaridis, N.K., Pandi, T.A., and Matis, K.A., 2004. Chromium(VI) removal from aqueous solutions by Mg−Al−CO_3 hydrotalcite: Sorption−desorption kinetic and equilibrium studies. *Industrial & Engineering Chemistry Research*, 43 (9), 2209–2215.

Manyangadze, M., Chikuruwo, N.H.M., Narsaiah, T.B., Chakra, C.S., Radhakumari, M., and Danha, G., 2020. Enhancing adsorption capacity of nano-adsorbents via surface modification: A review. *South African Journal of Chemical Engineering*, 31 (September 2019), 25–32.

Morris, J., 1991. Laboratory for physical and colloid Chemistry. J*ournal of Colloid and Interface Science*, 141 (2).

Mustapha, S., Shuaib, D.T., Ndamitso, M.M., Etsuyankpa, M.B., Sumaila, A., Mohammed, U.M., and Nasirudeen, M.B., 2019. Adsorption isotherm, kinetic and thermodynamic studies for the removal of Pb(II), Cd(II), Zn(II) and Cu(II) ions from aqueous solutions using Albizia lebbeck pods. *Applied Water Science*, 9 (6), 142.

Ntuli, T.D. and Pakade, V.E., 2020. Hexavalent chromium removal by polyacrylic acid-grafted Macadamia nutshell powder through adsorption–reduction mechanism: Adsorption isotherms, kinetics and thermodynamics. *Chemical Engineering Communications*, 207 (3), 279–294.

Oyetade, O.A., Skelton, A.A., Nyamori, V.O., Jonnalagadda, S.B., and Martincigh, B.S., 2017. Experimental and DFT studies on the selective adsorption of Pb^{2+} and Zn^{2+} from aqueous solution by nitrogen-functionalized multiwalled carbon nanotubes. *Separation and Purification Technology*, 188, 174–187.

Panchangam, S.C., 2015. Engineering & science focus :: AITK A monthly academic bulletin Article : *Engineering & Science Focus: AITK*, (September), 1–4.

Rahimnejad, M., Pirzadeh, K., Mahdavi, I., and Peyghambarzadeh, S.M., 2018. Pb (..) Removal from aqueous solution by adsorption on activated carbon from kiwi peel.

Environmental Engineering and Management Journal, 17 (6), 1293–1300.

Ray, S.C., 2018. Nitrogenated carbon nanotubes functionalized with chlorine and oxygen: Electronic and magnetic properties for electronic/magnetic device applications. *Frontier Research Today*, 1, 1006.

Sarı, A. and Tuzen, M., 2008. Biosorption of Pb(II) and Cd(II) from aqueous solution using green alga (Ulva lactuca) biomass. *Journal of Hazardous Materials*, 152, 302–308.

Sidhaarth, K.R.A. and Jeyanthi, J., 2013. Adsorption of lead from aqueous solution by manganese ferrite nanoparticles. *Asian Journal of Chemistry,* 25 (17), 9920–9926.

Tiwari, S., Tripathi, I.P., and Tiwari, H.L., 2013. Effects of lead on environment. International *Journal of Emerging Research in Management &Technology*, 2 (6), 1–5.

Weber, W. and Morris, J., 1963. Kinetics of Adsorption on Carbon from Solution. *Journal of the Sanitary Engineering Division*, 89 (2), 31–60.

WHO, 2021. Lead poisoning. [online]. Available from: https://www.who.int/news-room/fact-sheets/detail/lead-poisoning-and-health [Accessed 10 Dec 2021].

U.S. Geological Survey, 2021. *Mineral Industry Surveys: Sulfur*. US Geological Survey.

CHAPTER 6
Conclusions and Recommendations

6.1. Conclusions

The aim of the study was to synthesize chlorine functionalized and nitrogen doped carbon nanotubes (ClNCNTs) using pyrolysis chemical vapour deposition method and to modify their surface with iron oxide nanoparticles for their use as adsorbents for Pb^{2+} ions in aqueous solution. The prepared nanomaterials were characterized using analytical techniques that included the characterisation techniques such as, TEM, EDX, PXRD, Raman spectroscopy, XPS, BET and TGA, the following conclusions were made.

TEM revealed the presence of hollow and bamboo-compartmented CNTs, some with open-ends for materials synthesized in the presence of chlorine and nitrogen. The bamboo-compartments were thought to have been initiated by nitrogen inclusion into the carbon matrix, whilst the open-ends were initiated by the presence of chlorine. Both chlorine and nitrogen enhanced the amounts of defects in the nanotube walls as evidenced by increased disorders from Raman analysis. Loading of Fe_3O_4 nanoparticles on the surface of the ClNCNTs was achieved and the attachment of the nanoparticles was thought to occur at defect sites created by chlorine and nitrogen. Varying the amount of iron salts during loading the surface of ClNCNTs with Fe_3O_4 nanoparticles revealed that the best nanoparticle distribution was achieved when 20 wt.% Fe_3O_4 was loaded. Surface area increased after iron oxide addition and further increased with an increase in iron loading, which was attributed to increase in pores by incorporation of Fe_3O_4 nanoparticles.

Both Fe_3O_4 loaded and un-loaded ClNCNTs proved to be good adsorbents for Pb^{2+} ions, with removal efficiencies of 76 and 70 % respectively. However, we will still recommend the use of Fe_3O_4 loaded ClNCNTs as an adsorbent of choice since the presence of magnetic Fe_3O_4 nanoparticles will make the adsorbent recoverable after use and re-used after recovery. The pseudo-second order model best fitted both the adsorbents with R^2 values of close to 1 obtained for both. Also, the experimental and the calculated adsorption capacities were similar when modelled with pseudo-second order model.

The Langmuir adsorption model best fitted data obtained from using a ClNCNTs as adsorbent, while Freundlich adsorption model best fitted data obtained from using a 20 wt.% Fe_3O_4/ClNCNTs as adsorbent.

6.2. Recommendations and future work

Synthesis of Fe_3O_4 nanoparticles and their use as adsorbent for Pb^{2+} ions should be done for comparison. This was hindered by lack of having a vacuum oven in our facilities.

Raman spectroscopy peaks at lower wavelength were too noisy hence the use of Raman spectroscopy with a laser power that will not change the phase of the magnetite or do optimization study of laser power is recommended.

To understand the adsorption process better, characterization of adsorbents after use is crucial. ClNCNTs and 20 wt.% Fe_3O_4/ClNCNTs post-adsorption with XPS is needed to determine the state of present lead and with FTIR, TGA and XRD.

There is also a need to evaluate the selectivity, stability, regeneration, and thermodynamics of the nano-adsorbents.

Effect of temperature will also need to be done to model the thermodynamics and describe the adsorption mechanism.

The regeneration of Fe_3O_4/ClNCNTs must also be investigated to check if the adsorbent can be re-used and for how many times.

Recent studies had indicated that ClNCNTs can perform better if used as electrochemical sensors or catalysts.

Appendix A

Supplementary Information

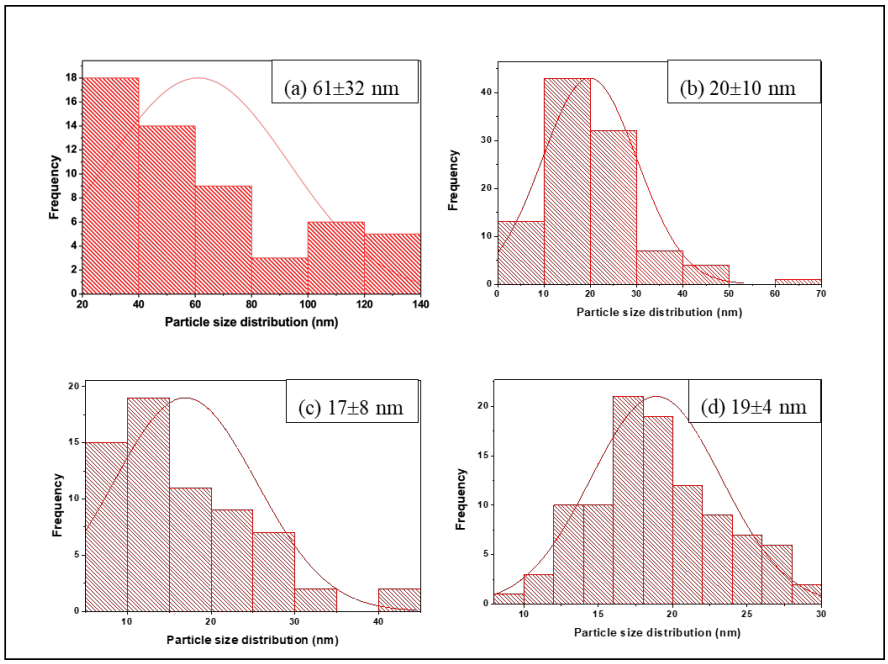

Figure S1: Histogram representing the average particles diameter of (a) ClNCNTs, (b) 10 wt.% Fe_3O_4, (c) 20 wt.% Fe_3O_4, 30 wt.% Fe_3O_4 and (d) 53 wt.% Fe_3O_4

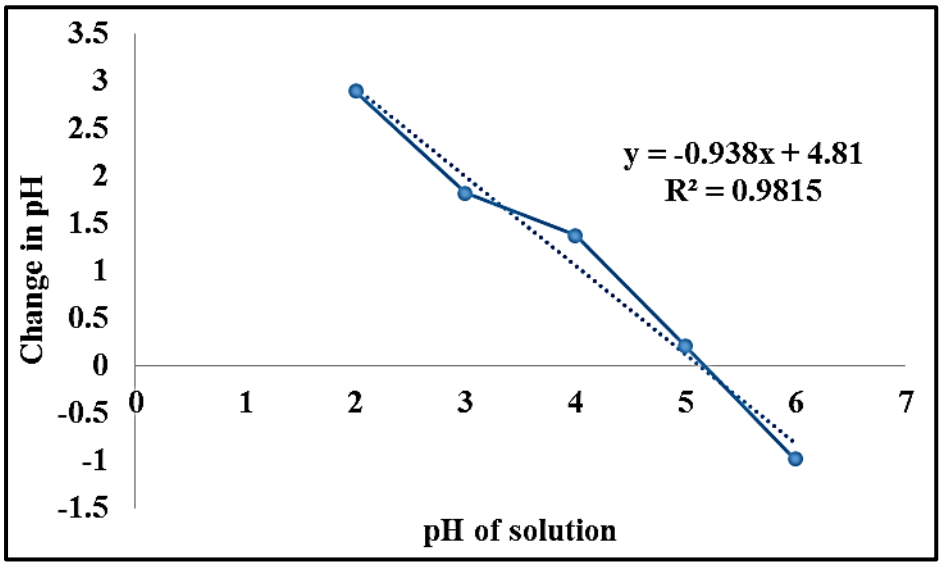

Figure S2: The point zero charge of ClNCNTs.

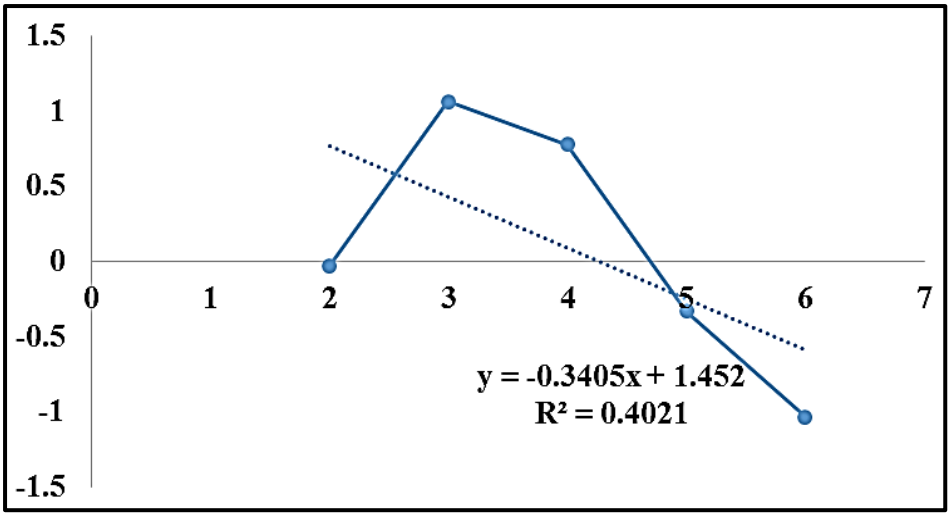

Figure S3: The point zero charge of 20 wt.% Fe_3O_4/ClNCNTs.